Università degli studi di Ferrara

DOTTORATO DI RICERCA IN
FISICA

CICLO XXX

COORDINATORE Prof. Vincenzo Guidi

MEASUREMENT OF THE RATIO OF THE $B^0 \to D^{*-}\tau^+\nu_\tau$ AND $B^0 \to D^{*-}\mu^+\nu_\mu$ BRANCHING FRACTIONS USING THREE-PRONG τ DECAYS

Settore Scientifico Disciplinare **FIS/01**

Dottorando
Dott. Siddi Benedetto Gianluca

(firma)

Tutore
Dott. Bozzi Concezio

(firma)

Anni 2014/2017

Table of contents

List of figures

List of tables

Introduction

In the Standard Model (SM) of particle physics, lepton flavor universality (LFU) is an accidental symmetry broken only by the Yukawa interactions. Differences between processes involving the the three lepton families originate from the different masses of the charged leptons. Further deviations from LFU would be a signature of physics processes beyond the SM. Standard Model extensions give additional interactions, implying in some cases a stronger coupling with the third generation of leptons. Semileptonic decays of b hadrons (hadrons containing a b quark) provide a sensitive probe to such new physics effects. The presence of additional charged Higgs bosons, vector boson (*e.g.* W') or leptoquarks [1–3], required by such SM extensions, can have significant effect on the semileptonic decay rate of $B^0 \to D^{*-}\tau^+\nu_\tau$. Since uncertainties due to hadronic effects cancel to a large extent, the SM prediction for the ratios between branching fractions of semitauonic decays of B mesons relative to decays involving lighter lepton families, such as $R(D^{*-}) = \frac{\mathscr{B}(B^0\to D^{*-}\tau^+\nu_\tau)}{\mathscr{B}(B^0\to D^{*-}\mu^+\nu_\mu)}$ and $R(D^-) = \frac{\mathscr{B}(B^0\to D^-\tau^+\nu_\tau)}{\mathscr{B}(B^0\to D^-\mu^+\nu_\mu)}$, are known with an uncertainty at the percent level [4–6]. The combination of experimental measurements of $R(D^{(*)})$ performed by BaBar[7, 8], Belle [9, 10] and LHCb [11] observing the channel where the τ decays in leptons or in one prong particle [12], gives a deviation from the SM prediction of about 4 σ. In particular, all measurements are consistently above the SM prediction. It is therefore important to perform additional measurements in this sector in order to improve the precision and confirm or disprove this deviation.

This thesis presents a measurement of $R(D^{*-})$, using τ hadronic decay with three charged particles (3-prong) in the final state, *i.e.* $\tau^+ \to \pi^+\pi^-\pi^+(\pi^0)\overline{\nu}_\tau$, by using the full data sample collected by LHCb in 2011-2012. The study of the 3-prong τ decay mode is complementary to the existing measurements, based on τ semileptonic and 1-prong decays and leads to higher signal to noise ratio and better statistical significance. In particular the 3-prong τ decay allows to reconstruct the τ decay vertex, useful to discriminate between signal and background sources and reconstruct the kinematics of the τ and B decays, due to a single neutrino in each of them.

The final aim of this thesis is to measure the ratio:

$$R(D^{*-}) = \frac{\mathscr{B}(B^0 \to D^{*-}\tau^+\nu_\tau)}{\mathscr{B}(B^0 \to D^{*-}\mu^-\nu_\mu)}. \tag{1}$$

Experimentally, what is measured is

$$\mathscr{K}(D^{*-}) \equiv \frac{\mathscr{B}(B^0 \to D^{*-}\tau^+\nu_\tau)}{\mathscr{B}(B^0 \to D^{*-}3\pi)} = \frac{N_{\rm sig}}{N_{\rm norm}} \frac{\varepsilon_{\rm norm}}{\varepsilon_{\rm sig}} \frac{1}{\mathscr{B}(\tau^+ \to 3\pi\overline{\nu}_\tau) + \mathscr{B}(\tau^+ \to 3\pi\pi^0\overline{\nu}_\tau)}, \tag{2}$$

where $3\pi \equiv \pi^+\pi^-\pi^+$, $\varepsilon_{\rm sig}$ and $\varepsilon_{\rm norm}$ are the efficiencies for the signal and normalization decay modes, respectively. The absolute branching fraction is obtained as $\mathscr{B}(B^0 \to D^{*-}\tau^+\nu_\tau) = \mathscr{K}(D^{*-}) \times \mathscr{B}(B^0 \to D^{*-}3\pi)$, where the branching fraction of the $B^0 \to D^{*-}3\pi$ decay is taken as external input. Measuring a ratio of branching ratios is useful to cancel theoretical and experimental uncertainties on luminosity, cross sections and hadronization probabilities (see Chapter 7).

A measurement of $R(D^*)$ can be obtained taking the branching fractions of the normalization channel and the semi-muonic decay as external inputs. In this way the equation will be:

$$R(D^{*-}) = \mathscr{K}(D^{*-}) \times \frac{\mathscr{B}(B^0 \to D^{*-}\pi^+\pi^-\pi^+)}{\mathscr{B}(B^0 \to D^{*-}\mu^-\nu_\mu)}. \tag{3}$$

The signal chosen for this study is defined according to the following decay chain:

$$\begin{aligned} B^0 \to & D^{*-}\tau^+\nu_\tau \\ & \hookrightarrow \pi^+\pi^-\pi^+(\pi^0)\overline{\nu}_\tau \\ & \hookrightarrow \pi^-\bar{D}^0 \\ & \hookrightarrow K^+\pi^- \end{aligned} \tag{4}$$

In the normalization channel the same D^{*-} decay chain is required. The visible final state for signal consists of two pions plus a kaon originating from the D^{*-} decay chain, which is fully reconstructed, and three pions from the τ decay; the additional two neutrinos are not detected. The τ decay vertex is reconstructed through a fit to the three pion tracks. Because of the presence of a neutrino, the momentum and energy of the τ are not known, but they can be estimated based on the separation of the τ and the B decay vertices, and energy conservation.

This thesis is organized as follows. In Chapter 1, an overview of the theoretical framework is given. The LHCb detector and a general view of the LHCb software framework are described in Chapter 2. The subsequent chapters (*i.e.* 3 to 7) are dedicated to the selection and the study of the $B^0 \to D^{*-}\tau^+\nu_\tau$ decay including the measurement of $R(D^{*-})$. The next

chapters are structured as follows. Chapter 3 describe the data and Monte Carlo used to perform the analysis (Sec. 3.1), along with corrections applied on MC in order to match data (Sec. 3.2), and the filtering and trigger selection applied to the Monte Carlo and data samples (Sec. 3.3, 3.4). In Chapter 4, signal selection and background suppression strategies are illustrated, including in Sec. 4.3 isolation criteria used to search for and veto additional neutral and charged particles. Section 4.4 describes the decay reconstruction in the signal and background hypotheses necessary to determine the variables that are used in the fit performed for determining the signal yield. The Sec. 4.5 describes a multivariate analysis used to supress the further background due to double charm decays ($B \to D^{*-}D$ decays) whose composition if fully discussed in Chapter 5. Finally the determination of the signal yield is presented in chapter 6 including the description of the fit model and the estimation of experimental bias. Systematic uncertainties are then illustrated in Chapter 7.

The novel technique presented in this thesis can be applied to all the other semitauonic decays and also allows isolation of large signal samples with high purity, which can be used to measure angular distributions and other observables proposed in the literature to discriminate between SM and new physics contributions.

Chapter 1

Theory of lepton flavour universality in semileptonic decays

1.1 The Glashow-Weinberg-Salam model

In 1967/68, Weinberg and Salam unified weak and electromagnetic interactions by applying the Higgs mechanism to the $SU(2) \times U(1)$ gauge theory (known as the Georgi-Glashow model). The general idea is that weak interactions are mediated by gauge bosons (W, Z), which are at first massless. The lagrangian for the theory also containes terms for massless elctrons, muons and neutrinos, and is introduced with a non-vanishing vacuum expectation value for the Higgs field. The resulting spontaneous symmetry breaking gives masses to quarks, charged leptons, and to the gauge bosons, but not to photons and neutrinos. The $SU(2)$ group corresponds to weak interaction with coupling constant g and gauge fields A^a_μ. The $U(1)_Y$ group corresponds to the hypercharge with coupling constant g' and gauge field B_μ. The Higgs part of the lagrangian for the Glashow-Weinberg-Salam model (GWS model[13–15]) is

$$\mathscr{L} = T + V = (D_\mu \phi)^\dagger D^\mu \phi + \mu^2 \phi^\dagger \phi - \lambda (\phi^\dagger \phi)^2 \tag{1.1}$$

where $D_\mu \phi = (\partial_\mu + igT^a A^a_\mu ig'YB_\mu)\phi$ with $\phi = \begin{pmatrix} \phi^+ \\ \phi^0 \end{pmatrix}$, $Y = \frac{1}{2}$ and T^a as the weak isospin matrices.

The Higgs potential $V(\phi\phi^\dagger) = -\mu^2 \phi^\dagger \phi + \lambda (\phi^\dagger \phi)^2$ has a minimum when $\phi\phi^\dagger = \mu^2/\lambda^2 \equiv v^2/2$, where $\sqrt{v}/2$ is the vacuum expectation value (VEV) of $\phi (v \approx 246 GeV)$.

Because the ground state is infinite degenerate, it is possible to arbitrarily choose

$$< \phi >= \begin{pmatrix} 0 \\ v/\sqrt{2} \end{pmatrix} \tag{1.2}$$

v has units of mass, and it is the only parameter in the Standard Model which is not dimensionless. The $SU(2)$ group generator for spin 1/2 particles can be expressed as Pauli matrices: $T^a = \frac{1}{2}\sigma^a$. It follows that:

$$\begin{aligned}
\frac{1}{2}\sigma^1 < \phi > &= \begin{pmatrix} 0 & 1/2 \\ 1/2 & 0 \end{pmatrix} \begin{pmatrix} 0 \\ v/\sqrt{2} \end{pmatrix} = \begin{pmatrix} v/2\sqrt{2} \\ 0 \end{pmatrix} \neq 0 \\
\frac{1}{2}\sigma^2 < \phi > &= \begin{pmatrix} 0 & -i/2 \\ i/2 & 0 \end{pmatrix} \begin{pmatrix} 0 \\ v/\sqrt{2} \end{pmatrix} = \begin{pmatrix} -iv/2\sqrt{2} \\ 0 \end{pmatrix} \neq 0 \\
\frac{1}{2}\sigma^3 < \phi > &= \begin{pmatrix} 1/2 & 0 \\ 0 & -1/2 \end{pmatrix} \begin{pmatrix} 0 \\ v/\sqrt{2} \end{pmatrix} = \begin{pmatrix} 0 \\ -v/2\sqrt{2} \end{pmatrix} \neq 0 \\
\frac{1}{2}I < \phi > &= \begin{pmatrix} 1/2 & 0 \\ 0 & 1/2 \end{pmatrix} \begin{pmatrix} 0 \\ v/\sqrt{2} \end{pmatrix} = \begin{pmatrix} 0 \\ v/2\sqrt{2} \end{pmatrix} \neq 0
\end{aligned} \tag{1.3}$$

All the generators are in broken in GWS. However, one linear combination of these generators remains unbroken:

$$T^3 + Y = (\frac{1}{2}\sigma^3 + \frac{1}{2}I) \begin{pmatrix} 0 \\ v/\sqrt{2} \end{pmatrix} = 0 \tag{1.4}$$

It is easy to show that this unbroken $U(1)$ is the electric charge.

$$Q = T^3 + Y = \begin{pmatrix} 1/2 & 0 \\ 0 & -1/2 \end{pmatrix} + \begin{pmatrix} 1/2 & 0 \\ 0 & 1/2 \end{pmatrix} = \begin{pmatrix} 1 & 0 \\ 0 & 0 \end{pmatrix} \tag{1.5}$$

That means that $\phi = \begin{pmatrix} \phi^+ \\ \phi^0 \end{pmatrix}$ has the electric charge as indicated before.

Therefore the symmetry spontaneous breaking for the GWS model is $SU(2)\times U(1)_Y \rightarrow U(1)_{EM}$. Now there are three broken generators:

$$\begin{aligned} T^1 &= \frac{1}{2}\sigma^1 \\ T^2 &= \frac{1}{2}\sigma^2 \\ T^3 - Y &= \frac{1}{2}\sigma^3 - \frac{1}{2}I \end{aligned} \tag{1.6}$$

For this reason there are three Goldstone bosons in the GWS model. In order to compute the mass induced by the spontaneous symmetry breaking we have to promote the global symmetry to a local symmetry and rewrite the field as:

$$\phi = \frac{1}{\sqrt{2}}(h+v)e^{[iT^1\pi^1+iT^2\pi^2+i(T^3-Y)\pi^3]}\begin{pmatrix}0\\1\end{pmatrix} \tag{1.7}$$

Taking into account the gauge invariance and gauging away the three Goldstone bosons π^1, π^2 and π^3 we have:

$$\phi \rightarrow \frac{1}{\sqrt{2}}(h+v)\begin{pmatrix}0\\1\end{pmatrix} \tag{1.8}$$

Substituting it into the Eqn. 1.1, we obtain:

$$\mathscr{L} = (D_\mu\phi)^\dagger D^\mu\phi \tag{1.9}$$

$$= \frac{1}{2}\partial_\mu h\partial^\mu h + \frac{1}{8}[(-gA^3_\mu + g'B_\mu)^2 + g^2(A^1_\mu A^{1\mu} + A^2_\mu A^{2\mu})](h+v)^2 \tag{1.10}$$

Hence the fields A^1_μ and A^2_μ have acquired a mass

$$M^2_{A_1} = M^2_{A_2} = \frac{1}{4}g^2v^2 \equiv M^2_W \tag{1.11}$$

This is the mass of the W bosons generated by gauge fields A^1_μ and A^2_μ. We can also find that the field $-gA^3_\mu + g'B_\mu$ has also acquired a mass. To find the mass of this field, we need first to normalize the field:

$$Z_\mu = \frac{1}{\sqrt{g^2+g'^2}}(gA^3_\mu - g'B_\mu) \tag{1.12}$$

where the normalization factor comes from $< Z_\mu | Z_\nu >= \delta_{\mu\nu}$.

Then the lagrangian 1.10 can be rewritten in terms of the Z_μ field:

$$\mathscr{L} = \frac{1}{8}[(g^2 g'^2) Z_\mu Z^\mu + g^2 (A^1_\mu A^{1\mu} + A^2_\mu A^{2\mu})](h+v)^2 \tag{1.13}$$

This implies that the field Z_μ acquires a mass

$$M_Z^2 = \frac{1}{4}(g^2 g'^2) v^2 \tag{1.14}$$

The ortogonal combination, field $\frac{1}{\sqrt{g^2+g'^2}}(g' A^3_\mu + g B_\mu)$, has no mass term, corresponding to the photon in the GWS model. As a result the details about how the massive particles emerge through the spontaneous symmetry breaking in the GWS model has been illustrated. The gauge field A^1_μ, A^2_μ and Z_μ have eaten the Goldstone bosons π^1, π^2 and π^3 to acquire the mass of W and Z bosons. The other Goldstone boson remains massless and it is interpreted as photon. It is also possible to see that the photon and the Z particle are both linear combination of A^3_μ and B_μ fields. Thus it is possible to write this in matrix form:

$$\begin{pmatrix} Z_\mu \\ A_\mu \end{pmatrix} = \begin{pmatrix} cos\theta_w & -sin\theta_w \\ sin\theta_w & cos\theta_w \end{pmatrix} \begin{pmatrix} A^3_\mu \\ B_\mu \end{pmatrix} \tag{1.15}$$

where $cos\theta_w = \frac{g}{\sqrt{g^2+g'^2}}$ and $sin\theta_w = \frac{g'}{\sqrt{g^2+g'^2}}$. θ_w is called weak mixing angle.

Therefore in the tree level, we can relate the mass of the W boson and the mass of the Z boson by the weak mixing angle:

$$M_W = M_Z cos\theta_w \tag{1.16}$$

Eqns. 1.11 and 1.14 relate the W and Z bosons masses to some basic parameters of the theory: g, g', $-\mu^2$ and λ. These relations allow the masses of W and Z bosons to be determined in term of three experimentally well known quantities:

1. Fine structure constant: $\alpha = e^2/4\pi\varepsilon_0\hbar c$
2. Fermi coupling constant: $G_F/(\hbar c)^3$
3. Weak mixing angle: θ_w

The parameter v in Eqns. 1.11 and 1.14 can be expressed in terms of G_F as $v = (G_F\sqrt{2})^{-1/2}$. The parameters g and g' can be written in terms of electric charge and weak mixing angle as $gsin\theta_w = g'cos\theta_w = e$. The W and Z bosons masses can be interpreted in terms of the above

three basic physical quantities:

$$M_W = \left(\frac{\alpha\pi}{G_F\sqrt{2}}\right)^{1/2}\frac{1}{sin\theta_w}, \qquad M_Z = \left(\frac{\alpha\pi}{G_F\sqrt{2}}\right)^{1/2}\frac{2}{sin2\theta_w} \tag{1.17}$$

1.2 The Cabibbo-Kobayashi-Maskawa matrix

In the SM with $SU(2)\times U(1)$ as the gauge group of electroweak interactions, both quarks and leptons are assigned to be left-handed doublets and right-handed singlets. The quark mass eigenstates are not the same as the weak eigenstates, and the matrix relating these bases was defined for six quarks, and given an explicit parametrization by Kobayashi and Maskawa in 1973 [16]. This generalizes the four-quark case, where the matrix is described by a single parameter, the Cabibbo angle.

By convention, the mixing is often expressed in terms of a 3×3 unitary matrix V operating on the charge $-e/3$ quark mass eigenstates (d, s and b):

$$\begin{pmatrix} d' \\ s' \\ b' \end{pmatrix} = \begin{pmatrix} V_{ud} & V_{us} & V_{ub} \\ V_{cd} & V_{cs} & V_{cb} \\ V_{td} & V_{ts} & V_{tb} \end{pmatrix} \begin{pmatrix} d \\ s \\ b \end{pmatrix} \tag{1.18}$$

There are several parametrizations of the Cabibbo-Kobayashi-Maskaya (CKM) matrix [17]. A "standard" parametrization of V utilizes three mixing angles θ_{12}, θ_{23}, θ_{13} and a CP-violationg phase δ_{13}

$$V = \begin{pmatrix} c_{12}c_{13} & s_{12}c_{13} & s_{13}e^{-i\delta_{13}} \\ -s_{12}c_{23} - c_{12}s_{23}s_{13}e^{i\delta_{13}} & c_{12}c_{23} - s_{12}s_{23}s_{13}e^{i\delta_{13}} & s_{23}c_{13} \\ s_{12}s_{23} - c_{12}c_{23}s_{13}e^{i\delta_{13}} & -c_{12}s_{23} - s_{12}c_{23}s_{13}e^{i\delta_{13}} & c_{23}c_{13} \end{pmatrix} \tag{1.19}$$

with $c_{ij} = cos\theta_{ij}$ and $s_{ij} = sin\theta_{ij}$ for the "generation" label $i, j = 1,2,3$. This has distinct advantages of intepretation, for the rotation angles are defined and labeled in a way which relate to the mixing of two specific generations, and if one of these angles vanishes, so does the mixing between those two generations; in the limit $\theta_{23} = \theta_{13} = 0$, the third generation decouples, and the situation reduces to the usual Cabibbo mixing of the first two generations, with θ_{12} identified as the Cabibbo angle. The real angles θ_{12}, θ_{23}, θ_{13} can all be made to lie in the first quadrant by an appropriate redefinition of quark field phases.

The standard parametrization can be approximated in a way that emphasizes the hiearchy in the size of the angles, knowing experimentally that $s_{12} \gg s_{23} \gg s_{13}$. Setting $\lambda \equiv s_{12}$, the

sine of the Cabibbo angle, one can express the other elements in terms of powers of λ, the so-called Wolfenstein parameterization [18],

$$\begin{pmatrix} 1-\lambda^2/2 & \lambda & A\lambda^3(\rho-i\eta) \\ -\lambda & 1-\lambda^2/2 & A\lambda^2 \\ A\lambda^3(1-\rho-i\eta) & -A\lambda^2 & 1 \end{pmatrix} + \mathscr{O}(\lambda^4), \tag{1.20}$$

with A, ρ and η real numbers that were intended to be of order unity, and where

$$s_{12} = \lambda = \frac{|V_{us}|}{\sqrt{|V_{ud}|^2 + |V_{us}|^2}} \tag{1.21}$$

$$s_{23} = A\lambda^2 = \lambda \left| \frac{V_{cb}}{V_{us}} \right| \tag{1.22}$$

$$s_{13} e^{i\delta} = V_{ub}^* = A\lambda^3(\rho + i\eta) \tag{1.23}$$

This approximate form is widely used, especially for B physics, but care must be taken, especially for CP-violating effects in K physics, since the phase enters in V_{cd} and V_{cs} through terms that are higher order in λ. Another parameterization has been advocated [19] that arise naturally where one builds model of quark masses in which initially $m_u = m_d = 0$. With no phases in the third row or third column, the connection between measurements of CP-violating effects for B mesons and single CKM parameters is less direct than in the standard parametrization.

Using the independently measured CKM elements mentioned above, the unitarity of the CKM matrix can be easily checked. We obtain $|V_{ud}|^2 + |V_{us}|^2 + |V_{ud}|^2 = 0.9996 \pm 0.0005$ (1st row), $|V_{cd}|^2 + |V_{cs}|^2 + |V_{cb}|^2 = 1.040 \pm 0.032$ (2nd row), $|V_{ud}|^2 + |V_{cd}|^2 + |V_{td}|^2 = 0.9975 \pm 0.0022$ (1st column), and $|V_{us}|^2 + |V_{cs}|^2 + |V_{ts}|^2 = 1.042 \pm 0.032$ (2nd column), respectively [20]. For the second row, a slightly better check is obtained subtracting the sum of the first row from the measurement of $\Sigma_{i,j=u,c,d,s,b}|V_{ij}|^2$ from the W leptonic branching ratio, yielding $|V_{cd}|^2 + |V_{cs}|^2 + |V_{cb}|^2 = 1.002 \pm 0.027$. The sum of the three angles, $\alpha + \beta + \gamma = (183^{+7}_{-8})^\circ$, is also consistent with the SM expectation, where:

$$\beta = arg\left(-\frac{V_{cd}V_{cb}^*}{V_{td}V_{tb}^*} \right), \qquad \alpha = arg\left(-\frac{V_{td}V_{tb}^*}{V_{ud}V_{ub}^*} \right) \tag{1.24}$$

$$\gamma = arg\left(-\frac{V_{ud}V_{ub}^*}{V_{cd}V_{cb}^*} \right) \tag{1.25}$$

The CKM matrix elements can be most precisely determinated by a global fit that uses all available measurements and imposes the SM constraints. The results for the Wolfenstein

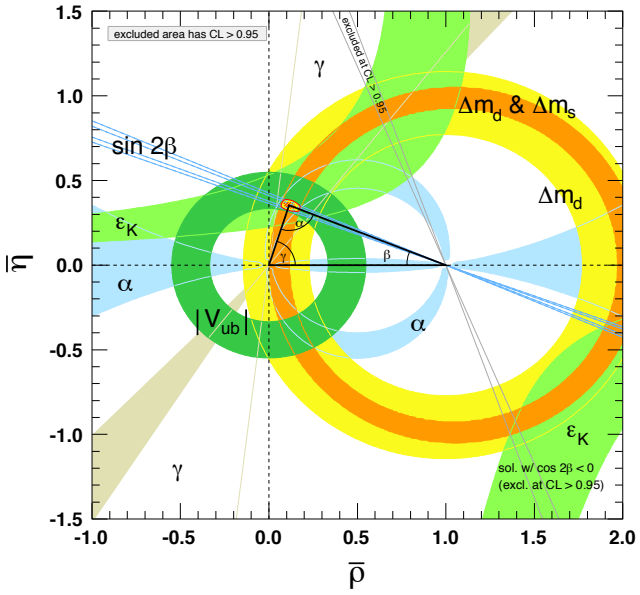

Fig. 1.1 95% CL constraints on the $\bar{\rho},\bar{\eta}$ plane.

parameters are

$$\lambda = 0.22506 \pm 0.00050, \qquad A = 0.911 \pm 0.026, \tag{1.26}$$

$$\rho = 0.124^{+0.019}_{-0.018}, \qquad \eta = 0.356 \pm 0.011 \tag{1.27}$$

The allowed ranges of the magnitudes of all nine CKM elements are

$$V = \begin{pmatrix} 0.97434^{+0.00011}_{-0.00012} & 0.22506 \pm 0.00050 & 0.00357 \pm 0.00015 \\ 0.22492 \pm 0.00050 & 0.97351 \pm 0.00013 & 0.0411 \pm 0.0013 \\ 0.00875^{+0.00032}_{-0.00033} & 0.0403 \pm 0.0013 & 0.99915 \pm 0.00005 \end{pmatrix} \tag{1.28}$$

Fig. 1.1 shows the constraints on the $\bar{\rho},\bar{\eta}$[1] plane from various measurements and the global fit result. The shaded 95% CL regions all overlap consistently around the global fit region.

1.3 The theory of semileptonic decays

The amplitude of the semileptonic decay of a meson M_{Qq} into a state containing a meson $M_{q'q}$ can be written as a term proportional to the product of a leptonic current L^{μ} and a hadronic current H_{μ} [6]. If the exchanged four-momentum $q = p - p'$ between the two mesons of

[1] where $\bar{\rho},\bar{\eta}$ are rescaled in the Wolfenstein parametrization and are defined as $\bar{\rho} = \rho(1-\lambda^2/2)$ and $\bar{\eta} = \eta(1-\lambda^2/2)$

momenta p and p' is much smaller than the mass M_W of the $W^{\pm}$ boson, the amplitude can be written in the following way:

$$\mathscr{M} = -i\frac{G_F}{\sqrt{2}} V_{Qq'} L^{\mu} H_{\mu} \tag{1.29}$$

The leptonic current is given by

$$L^{\mu} = \bar{l}\gamma^{\mu}(1-\gamma_5)\nu_l \tag{1.30}$$

while the hadronic current is

$$H_{\mu} = \langle M_{q'q}(p')|j_{\mu}^{H}|M_{Qq}(p)\rangle \tag{1.31}$$

where j_{μ}^{H} can be expressed in term of the Lorentz-invariant quantities that are combinations of $p_{\mu}+p'_{\mu}$, q_{μ} and q^2. Since the two mesons interact also strongly, the hadronic current will contain some terms that parameterize in the non-pertubative QCD effects. These terms are called form factors, they depend on the given initial and final state and they are measurable experimentally.

Several methods exist to calculate these form factors, one of them is the Heavy Quark Effective Theory (HQET).The calculation of the branching ratio of $B^0 \to D^{*-}\tau^+\nu_\tau$ using HQET is performed in Sec. 1.4.

1.4 Standard Model expectation for $\mathscr{B}(B^0 \to D^{(*)-}\tau^+\nu_\tau)/\mathscr{B}(B^0 \to D^{(*)-}\ell^+\nu_\ell)$

An effective weak hamiltonian for $b \to c\ell\bar{\nu}_l$ transitions can be written as follows [6]

$$\mathscr{H}_{eff} = \frac{4G_F V_{cb}}{\sqrt{2}} J_{bc,\mu} \sum_{\ell=e,\mu,\tau} (\bar{\ell}\gamma^{\mu} P_L \nu_\ell) + h.c. \tag{1.32}$$

where $J_{bc,\mu}$ is the effective SM $b \to c$ charged current

$$J_{bc,\mu} = \bar{c}\gamma_{\mu} P_L b \tag{1.33}$$

In the SM, the decays $(B^0 \to D^{(*)-}\ell^+\nu)$ $(\ell = \mu, \tau)$ differ only due to the mass of the lepton. The differential rate of the $B^0 \to D^{(*)-}\ell^+\nu$ decay as a function of the decay kinematics is

given by:

$$\frac{d^2\Gamma_\ell}{dq^2 dcos\theta} = \frac{G_F^2|V_{cb}|^2 q^2}{256\pi^3 m_B^2}\left(1-\frac{m_\ell^2}{q^2}\right)^2 \times \left[(1-cos\theta)^2|H_+(q^2)|q^2 + (1+cos\theta)^2|H_-(q^2)|^2 + 2sin^2\theta|H_0(q^2)| + \frac{m_\ell^2}{q^2}\left(sin^2\theta(|H_+(q^2)|^2+|H_-(q^2)|^2) + 2|H_s(q^2) - H_0(q^2)cos\theta|^2\right)\right] \quad (1.34)$$

where q^2 is the squared mass of the $\ell\nu$ system, θ is the angle between the D^* and the ℓ in the $\ell\nu$ rest frame. The H_X are the hadronic currents, which in the SM are given by:

$$\begin{aligned} H_\pm^{SM}(q^2) &= (m_B + m_{D^*})A_1(q^2) \mp \frac{2m_B}{m_B+m_{D^*}}|p|V(q^2), \\ H_0^{SM}(q^2) &= \frac{1}{2m_{D^*}\sqrt{q^2}}\left[(m_B^2 - m_{D^*}^2 - q^2)(m_B+m_{D^*})A_1(q^2) - \frac{4m_B^2|p|^2}{m_B+m_{D^*}}A_2(q^2)\right], \\ H_s^{SM}(q^2) &= \frac{2m_B|p|}{\sqrt{q^2}}A_0(q^2) \end{aligned} \quad (1.35)$$

where $A_0(q^2)$, $A_1(q^2)$, $A_2(q^2)$ and $V(q^2)$ are hadronic form factors defined by

$$\langle D^*(p_{D^*},\varepsilon_\alpha)|\bar{c}\gamma_\mu b|B(p_B)\rangle = \frac{2iV(q^2)}{m_B+m_{D^*}}\varepsilon_{\mu\nu\alpha\beta}\varepsilon^{*\nu}p_B^\alpha p_{D^*}^\beta, \quad (1.36)$$

$$\begin{aligned} \langle D^*(p_{D^*},\varepsilon_\alpha)|\bar{c}\gamma_\mu\gamma_5 b|B(p_B)\rangle &= 2m_{D^*}A_0(q^2)\frac{\varepsilon^*\cdot q}{q^2}q_\mu + (m_B+m_{D^*})A_1(q^2) \\ &\times\left(\varepsilon_\mu^* - \frac{\varepsilon^*\cdot q}{q^2}q_\mu\right) \\ &- A_2(q^2)\frac{\varepsilon^*\cdot q}{m_B+m_{D^*}} \\ &\times\left((p_B+p_{D^*})_\mu - \frac{m_B^2-m_{D^*}^2}{q^2}q_\mu\right) \end{aligned} \quad (1.37)$$

where ε_α are the helicity basis vector of the D^* meson.

Integrating Eqn. 1.34 over θ gives the rate of $B \to D^{(*)}\ell^+\nu$ as a function of q^2

$$\frac{d\Gamma_\ell}{dq^2} = \frac{G_F^2|V_{cb}|^2|p|q^2}{96\pi^3 m_B^2}\left(1-\frac{m_\ell^2}{q^2}\right)^2\left[(|H_+(q^2)|^2 + |H_-(q^2)|^2 + |H_0(q^2)|^2) \times\left(1+\frac{m_\ell^2}{2q^2}\right) + \frac{3}{2}\frac{m_\ell^2}{q^2}|H_s(q^2)|^2\right] \quad (1.38)$$

The ratio of rates of the $B^0 \to D^{*-}\tau^+\nu_\tau$ and $B^0 \to D^{*-}\mu^+\nu_\mu$ decays as a function of q^2 is then given by

$$R_{D^*}(q^2) = \frac{d\Gamma_\tau/dq^2}{d\Gamma_\ell/dq^2} = \left(1-\frac{m_\tau^2}{q^2}\right)^2 \left[\left(1-\frac{m_\tau^2}{2q^2}\right) + \frac{3}{2}\frac{m_\tau^2}{q^2}\frac{|H_s(q^2)|^2}{|H_+(q^2)|^2+|H_-(q^2)|^2+|H_0(q^2)|^2}\right] \tag{1.39}$$

for $\ell = e, \mu$.

At a given point in the phase space, the only difference between $B^0 \to D^{*-}\tau^+\nu_\tau$ and $B^0 \to D^{*-}\mu^+\nu_\mu$ is given by the helicity suppressed form factor term. Averaging Eqn. 1.47 across phase space results in a lower value of R_{D^*}, due to the considerably reduced phase space available to the $B^0 \to D^{*-}\tau^+\nu_\tau$.

The form factors are calculable using HQET technique. Defining the velocity transfer

$$w \equiv v_B \cdot v_{D^*} = \frac{m_B^2 + m_{D^*}^2 - q^2}{2m_B m_{D^*}} \tag{1.40}$$

the process is described by a single universal form factor

$$h_{A_1}(w) = A_1(q^2)\frac{1}{M}\frac{2}{w+1} \tag{1.41}$$

and the ratios R_1, R_2 and R_0

$$\begin{aligned} A_0(q^2) &= \frac{R_0(w)}{M} h_{A_1}(w), \\ A_2(q^2) &= \frac{R_2(w)}{M} h_{A_1}(w), \\ V(q^2) &= \frac{R_1(w)}{M} h_{A_1}(w) \end{aligned} \tag{1.42}$$

where $M = \sqrt{m_B m_{D^*}}/(m_B + m_{D^*})$. In the heavy quark limit [21], the variation of these form factors with w is given by

$$\begin{aligned} h_{A_1}(w) &= h_{A_1}(1)[1 - 8\rho^2 z + (53\rho^2 - 15)z^2 - (231\rho^2 - 91)z^3], \\ R_1(w) &= R_1(1) - 0.12(w-1) + 0.05(w-1)^2, \\ R_2(w) &= R_2(1) + 0.11(w-1) - 0.06(w-1)^2, \\ R_0(w) &= R_0(1) - 0.11(w-1) + 0.01(w-1)^2, \end{aligned} \tag{1.43}$$

where $z = (\sqrt{w+1} - \sqrt{2})/(\sqrt{w+1} + \sqrt{2})$ and ρ^2 is the slope of the Isgur-Wise function. The factor of $h_{A_1}(1)$ is common to all of the hadronic currents in Eqn. 1.47, and R_{D^*} does not therefore depend on the value of h_{A_1}. Three of the four remaining parameters have been measured [22] using $B^0 \to D^{*-}\ell^+\nu$ decays, with averages:

$$\rho^2 = 1.401 \pm 0.033 \qquad R_1(1) = 1.401 \pm 0.033 \qquad R_2(1) = 0.854 \pm 0.020 \qquad (1.44)$$

The $R_0(1)$ parameter has not been measured, as $B^0 \to D^{*-}\mu^+\nu_\mu$ decays offer minimal sensitivity to this parameter due to the helicity suppression. This parameter must therefore be taken from theoretical calculations, such as those using HQET. The resulting SM expectation for R_{D^*} is 0.252 ± 0.003 [6, 23, 4], with dominant uncertainty arising from the calculation of the $R_0(1)$ parameter. For D^* decays, recent papers [5, 24] argue for larger uncertainties, up to 4%.

Measurements of $\mathscr{R}(D^{0,-})$ and $\mathscr{R}(D^{*-,0})$ and their averages $\mathscr{R}(D)$ and $\mathscr{R}(D^*)$ have been reported by the BaBar [8, 7] and Belle [9, 10] collaborations in final states involving electrons or muons from the τ decay. The LHCb collaboration measured $\mathscr{R}(D^*)$ [25] with results compatible with those from BaBar, while the result from the Belle collaboration is compatible with the SM within 1 standard deviation. In all of the above measurements, the decay of the τ lepton into a muon, or an electron, and two neutrinos was exploited. More recently, the Belle collaboration published a measurement [10] with events tagged using semileptonic decays, compatible with the SM within 1.6 standard deviations. A simultaneous measurement of $\mathscr{R}(D^*)$ and of the τ polarization, using hadronic tagging and reconstruction of the $\tau^- \to \pi^-\nu_\tau$ and $\tau^- \to \rho^-\nu_\tau$ decays, was published by the Belle collaboration [12, 26]. The average of all these $\mathscr{R}(D^*)$ measurements is in tension with the SM expectation at 3.3 standard deviations. All these $\mathscr{R}(D^{(*)-,0})$ measurements yield values that are above the SM predictions with a combined significance of about 4 standard deviations [27]. It is therefore crucial to confirm or disprove this result by performing more measurements as the one performed in this thesis.

1.5 New Physics in $B^0 \to D^{(*)-}\tau^+\nu_\tau$

At the end of the Sec. 1.4 it has been shown that the experimental measurements of $\mathscr{R}(D^*)$ disagree with the SM expectation. This means that New Physics (NP) interactions could be involved in such processes. The decay of B mesons into a τ lepton in the final state, can exhibit NP contributions not present in processes with light leptons. The large τ mass

can reduce the helicity suppression of certain semileptonic decay amplitudes which are not observable in decays with light leptons in the final state [6].

To have NP leading to charged lepton helicity suppression in $B^0 \to D^{*-}\tau^+\nu_\tau$, it is possible to add a total derivative of a scalar operator to the effective current J^μ_{bc}, so that the 1.33 charged current becames:

$$J^\mu_{bc} = \bar{c}\gamma_\mu P_L b + g_{SL} i\partial^\mu(\bar{c}P_L b) + g_{SR} i\partial^\mu(\bar{c}P_R b), \tag{1.45}$$

where the first term correspond to the SM charged current, while $g_{SL,SR}$ are dimensionful NP couplings. If the NP contributions are associated with a high NP scale $\Lambda \gg v_{EW}$, then $g_{SL,SR} \sim 1/\Lambda_{NP}$.

Only the H_s helicity amplitude is affected by these NP quark charged currents, becoming:

$$H_s(q^2) = H_s^{SM}\left[1 + (g_{SR} - g_{SL})\frac{q^2}{m_b + m_c}\right], \tag{1.46}$$

where H_s^{SM} is the SM amplitude defined in Eqn. 1.35. In this way the ratio of $B^0 \to D^{*-}\tau^+\nu_\tau$ to $B^0 \to D^{*-}\mu^+\nu_\mu$ becomes:

$$R_{D^*} = R_{D^*}^{SM} + A_{D^*} Re(g_{SR} - g_{SL}) + B_{D^*}|g_{SR} - g_{SL}|^2, \tag{1.47}$$

Similarly for $B^0 \to D^-\ell^+\nu_\ell$ decays

$$R_D = R_D^{SM} + A_D Re(g_{SR} - g_{SL}) + B_D|g_{SR} - g_{SL}|^2, \tag{1.48}$$

	$\bar{B} \to D\tau^-\bar{\nu}_\tau$	$\bar{B} \to D^*\tau^-\bar{\nu}_\tau$
$R(D^{(*)})_{SM}$	0.297 ± 0.017	0.252 ± 0.003
$A_{D^{(*)}}$ (GeV ^{2})	-3.25 ± 0.32	-0.230 ± 0.029
$B_{D^{(*)}}$ (GeV ^{4})	16.9 ± 2.0	0.643 ± 0.085

Table 1.1 Dependence of $R(D^{(*)})$ in the 2HDM according to Eqs. 1.47 and 1.48 $\bar{B} \to D\tau^-\bar{\nu}_\tau$ and $\bar{B} \to D^*\tau^-\bar{\nu}_\tau$ decays: the values of $R(D^{(*)})$, the parameters A and B with their uncertainties.

Table 1.1 lists the values of $A_{D^{(*)}}$ and $B_{D^{(*)}}$, which are determined by averaging over B^0 and B^- decays. The uncertainty estimation includes the uncertainties on the mass ratio mc/mb and the FF parameters.

Hence, a measurement of R_{D^*} and R_D can provide constraints on NP parameters. There are several NP candidate models which can be tested in $B^0 \to D^{*-}\tau^+\nu_\tau$ decay, such as

the two Higgs doublet model, the leptoquark model, models with new tensor mediators or coloured scalars. In a 2HDM of type *II* one Higgs doublet couples to down quarks and charged leptons, while another one gives the masses to the up quarks. Then the only free additional parameters are $tan\beta = v_u/v_d$ (the ratio of the two vacuum expectation values) and the mass of the charged Higgs boson, $m_{H^\pm}$. In this case the charged Higgs contribution to $B \to \tau\nu$ interfer destructively with the SM. Thus, an enhancement of $\mathscr{B}(B \to \tau\nu)$ is only possible if the absolute value of the charged Higgs contribution is bigger than two times the SM one, which is in conflict with $B \to D\tau\nu$. Hence, a 2HDM of type *II* cannot explain $\mathscr{R}(D^*)$ and $\mathscr{R}(D)$ simultaneously [28]. The difference between the two 2HDMs is that in the type *III* model both Higgs doublets couple to up and down quarks. In addition in the 2HDM-*III* framework the g_{SL} and g_{SR} parameters are not constrained between each other. The BaBar results on R_D and R_{D^*} show that the 2HDM-II is exluded at 99.8% confidence level, while the type-III model can account for the deviation from the SM simultaneously, but a significant portion of the parameters space is excluded by the analysis of q^2 spectra.

The remaining models are based on new type of particles, like leptoquarks which are hypothetical particles carrying both baryon number (B) and lepton number (L) and allow the interactions between the two particle types, tensor operator or coloured scalars (weak doublets with fractional electric charged). Another important NP model is the Minimal Supersymmetric Model (MSSM) in which fermions have bosonic superpartners (sfermions), and bosons have fermionic superpartners (bosinos). A recent theoretical work [29] shows a possible explaination of the $\mathscr{R}(D^*)$ and other semileptonic anomalies using two scalar leptoquarks (LQs) with the same mass and coupling to fermions related via a discrete symmetry: an $SU(2)_L$ singlet and an $SU(2)_L$ triplet, both with hypercharge $Y = -2/3$.

Chapter 2

The LHCb detector

The LHCb detector at the CERN Large Hadron Collider (LHC) is a forward single arm spectrometer covering an angular region from 10 mrad to 300 mrad along the LHC beam line corresponding to a pseudorapidity[1] range $2 < \eta < 5$. The layout of the detector is shown in Fig. 2.1. The coordinate system is a (O,x,y,z) reference frame centered at the collision point, the z axis is along the beam line and the y axis is along the vertical.

The LHCb detector is made of several subdetectors, each one dedicated to a specific task.

2.1 VErtex LOcator

The VErtex LOcator (VELO) [30] is the first stage of the detector. The VELO provides precise measurements of tracks close to the proton-proton interaction region. The VELO is made of two halves, each containing 21 modules composed of two semi-circular silicon strip sensors. The location of the modules inside the VELO is shown in Fig. 2.2. Each module consists of two 300 μm thick sensors allowing for measurements of the r and ϕ coordinates along the direction of the beam. The sensors are placed along the z direction, mounted in a vessel that maintains vacuum by a thin aluminum wall. This is done in order to minimize the material traversed by charged particles before they cross the sensor while protecting the sensors from the RF (radio frequency) waves produced by the beam. The track coordinates are used to reconstruct vertices from beauty and charmed hadrons as well as the primary pp collision vertex to allow for measurements of decay times and impact parameters. This information is crucial to discriminate signatures of heavy flavour decays from background. The global performance of the VELO must meet criteria such as having a signal noise ratio greater than 14, efficiency of at least 99% from tracks that traverse at least 4 sensors, and a

[1] The pesudorapidity, η is defined as: $\eta = -ln(tan(\Theta/2))$, where Θ is the polar angle of a particle, relative to the beam axis.

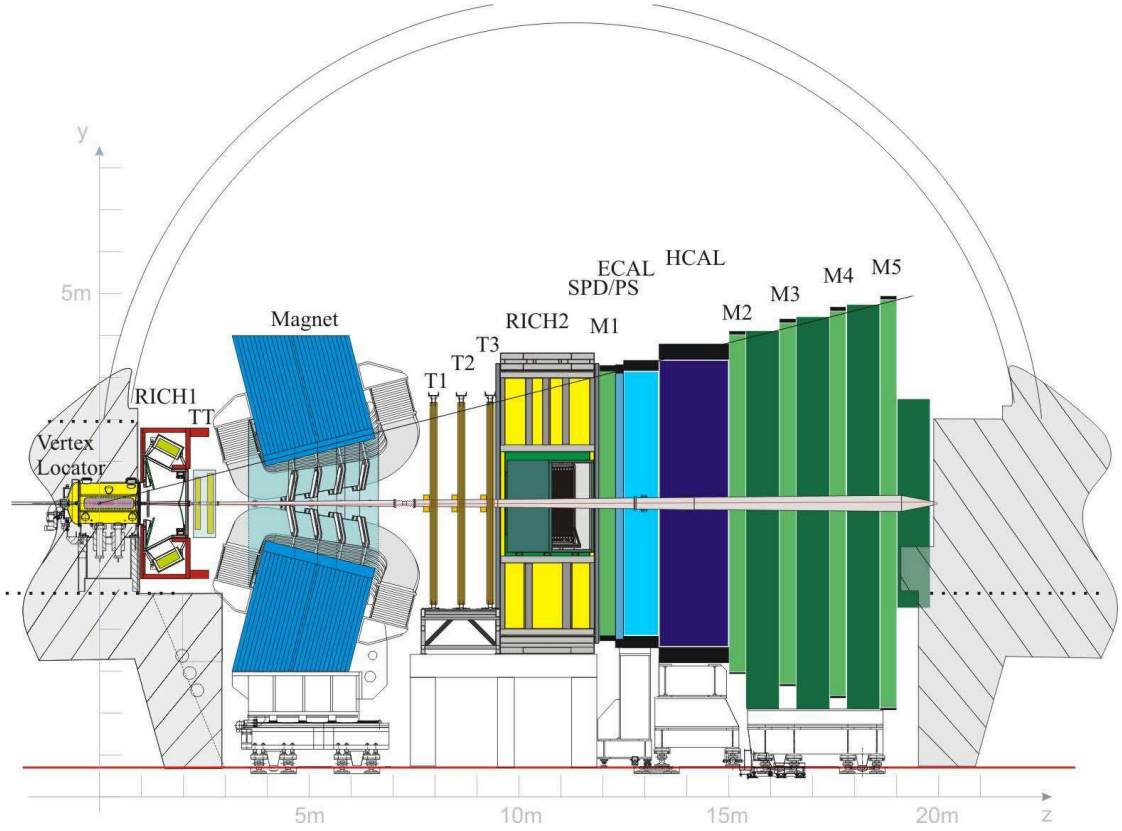

Fig. 2.1 The LHCb detector seen from the side.

spatial resolution of 5 μm for 100 mrad tracks. In order to cover the angular acceptance of the downstream detectors, the VELO has the ability to detect particles with pseudorapidity in the range $1.6 < \eta < 4.9$ coming from primary vertices in the range $|z| < 10.6$ cm. The resolution on the position of a vertex is 13 μm in the (x, y) plane and 71 μm along the z axis. The resolution σ_{IP} on the impact parameter (the minimum distance of a track to a primary vertex) is a function of the transverse momentum of the track p_T. The resolution σ_{IP} in fuction of the transverse momentum is shown in Fig. 2.3.

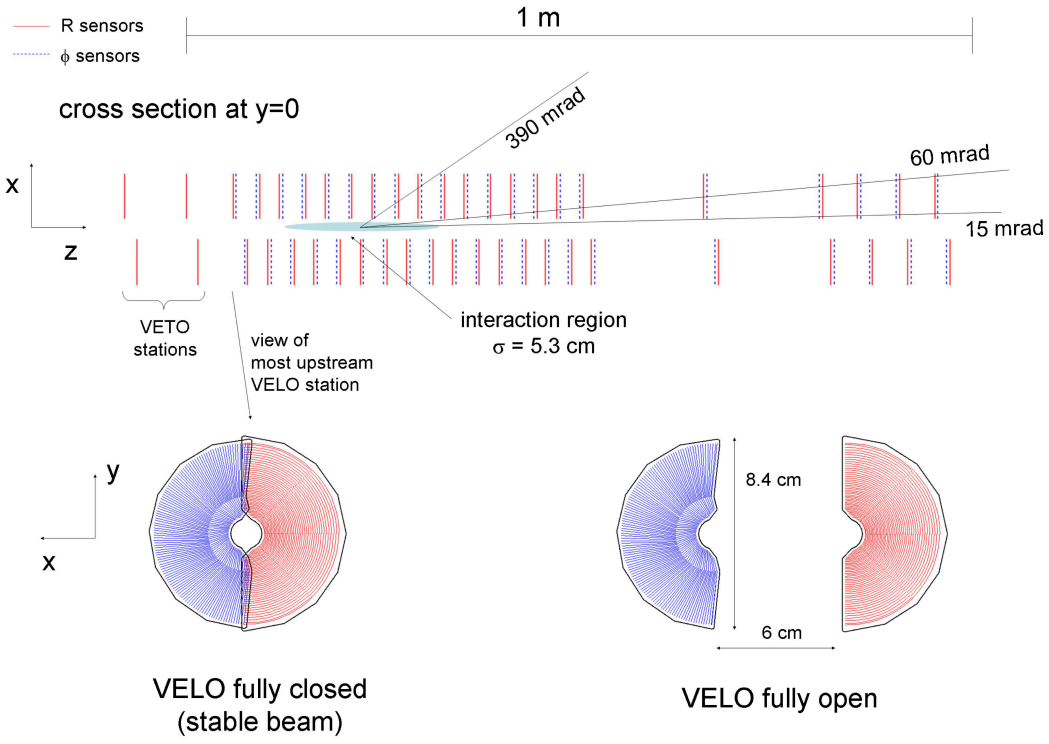

Fig. 2.2 Schematic of the Velo detector

2.2 Tracking System

An overview of the LHCb tracking system is shown in Fig. 2.4. It consists of tracking subdetectors, positioned both downstream and upstream of the magnet in order to measure the momenta of the charged particles. LHCb uses a warm dipole magnet with a bending power of about 4Tm and a peak strenght of 1.1 T; its polarity can be switched in order to minimize systematic effects in the tracking. The upstream detector is the Trigger Tracker (TT) composed of four layers of silicon strips. Three tracking stations (T1-T3) are located

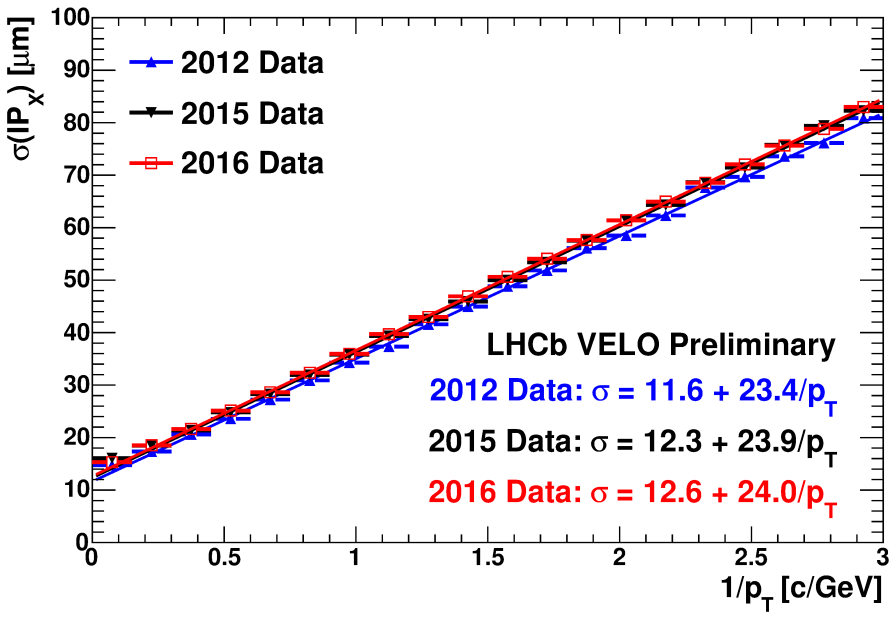

Fig. 2.3 Resolution of the x co-ordinate of the impact parameter vs. $1/p_T$ tracks from 2012, 2015, 2016 data.

downstream of the magnet. As the particle flux is much higher in the central region than in the outer one, two different technoligies are used: silicon microstrip for the Inner Tracker (IT) and straw tubes for the Outer Tracker (OT). The relative uncertainty on the momentum of a charged particle varies from 0.5% at low momentum to 1.0% at 200 GeV (Fig. 2.5).

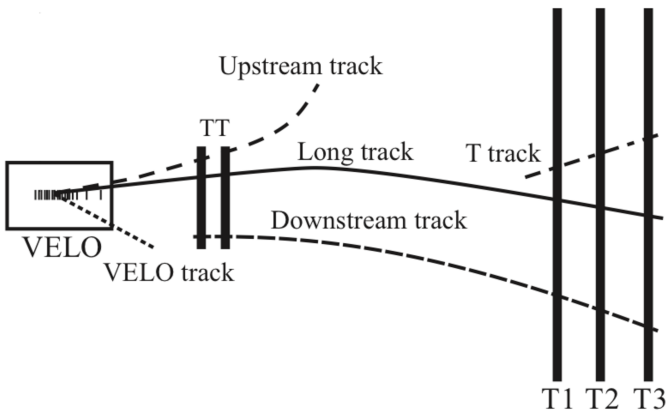

Fig. 2.4 Scheme of the LHCb tracking system and track types.

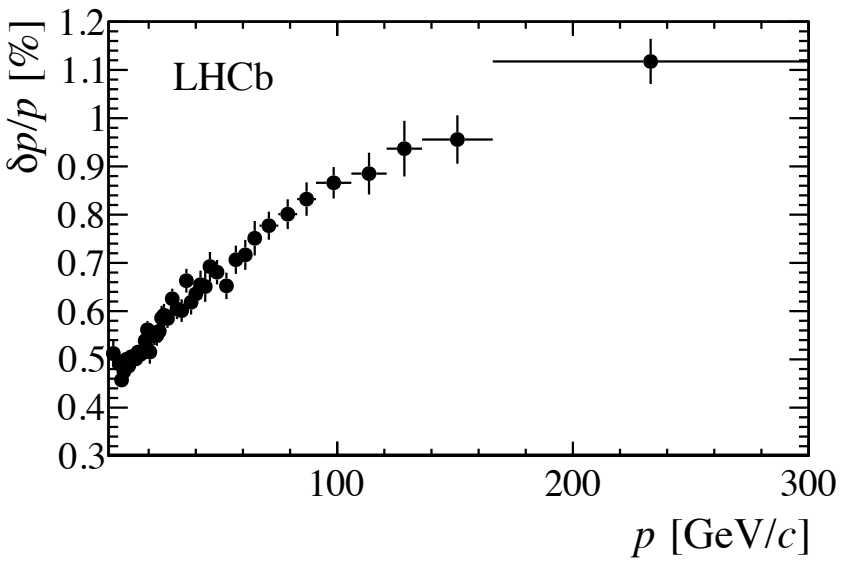

Fig. 2.5 Relative momentum resolution versus momentum for long tracks in data obtained using J/ψ decays.

2.3 Cherenkov detectors (RICH I and II)

The Ring Imaging Cherenkov (RICH) detectors provide particle identification information that is particularly important to distinguish between different types of charged hadrons, i.e. pions, kaons and protons. The ability for LHCb to be able to separate pions from kaons in B hadron decays is essential to the experiment. Two RICH detectors are installed in order to cover the full momentum range of charged particles. RICH 1 covers the 1-60 GeV/c range, using aerogel and C_4F_{10} radiators. RICH 2 is able to cover the higher momentum range 15-100 GeV/c, using CF_4 radiators. Charged particles passing through the RICH detectors are identified by their Cherenkov angle as shown in 2.6. Focusing of Cherenkov light is achieved by spherical and flat mirrors to reflect the image out of the spectrometer acceptance. Hybrid Photon Detectors (HPD) are used to detect Cherenkov photons with 200-600 nm wavelenght.

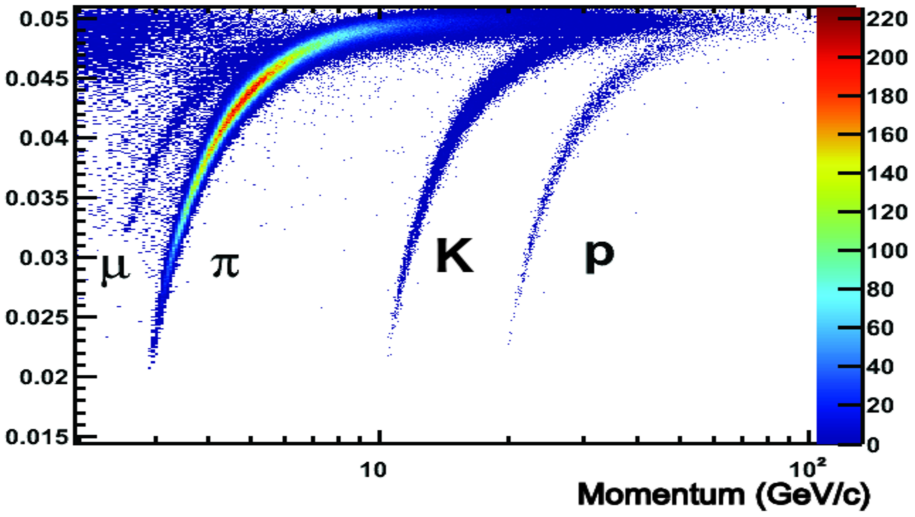

Fig. 2.6 Reconstructed Cherenkov angle as a function of track momentum in the C_4F_{10} radiator.

2.4 Calorimeter system

The calorimeter system has several functions. The first one is to select high transverse energy hadron, electron, photon and π^0 candidates for the hardware trigger (L0) which must return a decision within 4 μsec of the interaction. The calorimeter system is made of the elctromagnetic calorimeter (ECAL) and hadronic calorimeter (HCAL) with a scintillator pad detector (SPD) and a preshower detector (PS) in front of the ECAL. The SPD/PS system has a sensitive area which is 7.6 m wide and 6.2 m high. Both the ECAL and HCAL consist of alternate layers of absorber material (lead for the ECAL and iron for the HCAL) and scintillator material. The task of the ECAL is to select electrons and photons of high tranverse energy while rejecting the high background of charged pions. This is achieved by exploiting the longitudinal segmentation of the electromagnetic shower. Its energy resolution is $\sigma_E/E = 10\%/\sqrt{E} \oplus 10\%$. The scintillator pad detector in front of the pre-shower selects charged particles to distinguish electrons from photons.

The HCAL provides a measurement of the transverse energy of the hadrons and provides information to the hardware trigger. As a consequence it requires fast response even if not particularly high energy resolution: $\sigma_E/E = 70\%/\sqrt{E} \oplus 10\%$. For this reason and for space constraints its total thickness is not enough to contain the full hadronic shower. Scintillation light is read out by Photo Multiplier Tubes (PMT) using wavelenght-shifting fibers (WLS). The SPD/PS fibers are then read out by a 64 channel multianode photomultiplier tube (MAPMT). Individual phototubes for the ECAL and HCAL are set in proportion to the gain

and the distance to the beampipe. This has the advantage that allows to have a constant E_T scale. The HCAL tubes operate at a higher gain than those for the ECAL due to the light yield at the HCAL being smaller by a factor 30. The four detectors use a variable lateral segmentation as it is shown in Fig. 2.7.

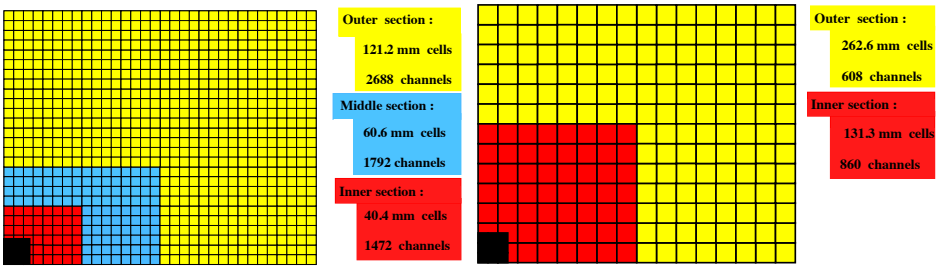

Fig. 2.7 Lateral segmentation of the SPD, PS, ECAL (left) and HCAL (right). Only one quarter of the detector front face is represented, but the number of cells correspond to the entire detector plane.

2.5 The muon chambers

Muon identification is crucial to LHCb experiment, as muons are present in the final states of many B decays. Moreover, muons from semi-leptonic b decays provide a tag of initial state flavour of accompanying neutral B mesons. In addition, the study of rare B decays such as flavour-changing neutral current decays, may reveal new physics beyond the standard model. The muon system of LHCb consists of five stations M1 to M5 installed along the beam axis and provides information for the high transverse momemtum muon trigger at level 0 and muon identification for the high level trigger and offline analysis. The five stations are made of Multi Wire Proportional Chambers (MWPC) with the exception of the inner part of M1, where the particle flow is higher, which is made of triple Gas Electron Multiplier (GEM). The M1 stage, placed in front of the calorimeters, improves the tranverse momentum measurement in the trigger. The muon trigger relies on muon track reconstruction and requires a hit in all five stations. The other stations are located at the end of the line just behind the HCAL. The M2 to M5 stations are interleaved with 80 cm thick iron absorbers in order to stop hadrons. The total thickness of the full muon system corresponds to 20 nuclear interaction lenghts which means that only muon with a minimum momentum of 6 GeV/c can cross the five stations. Stations M1 to M4 have high spatial resolution in the x coordinate which is used to define track direction and calculate the tranverse momentum of muon candidates with a resolution of 20%. The main purpose of stations M4 and M5 is to identify penetrating particles. Figure 2.8 shows the organisation of the five stations. Each detector is split into rectangular logical pads whose dimensions define the x and y resolution.

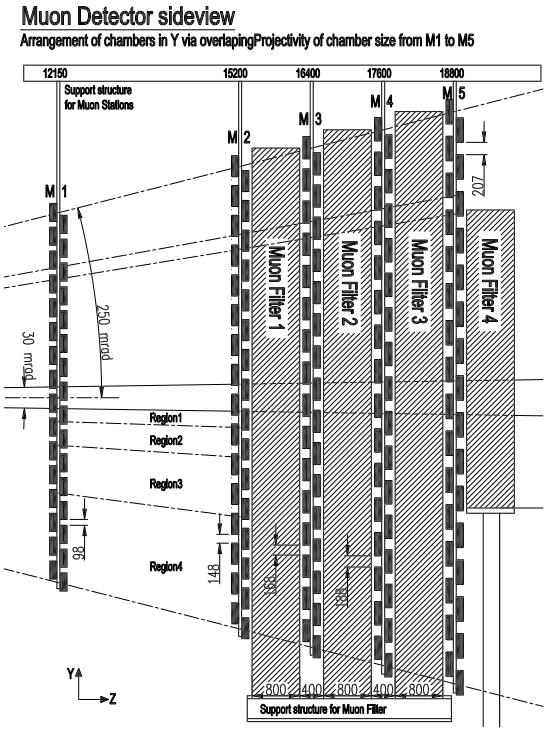

Fig. 2.8 Side view of the muon system in the y,z plane.

2.6 The LHCb trigger system

The LHCb trigger system is used to lower the data output rate from the beam crossing rate of 10 MHz down to a few kHz. Its architecture consists of two levels, the first level trigger (L0) and the High Level Trigger (HLT). L0 is implemented in hardware and uses input from the calorimeter and muon systems. It reduces the rate of crossings with at least one inelastic *pp* interaction to below 1.1 MHz, at which the whole detector can be readout by the front-end (FE) electronics. The full trigger system[2] is summarised in Fig. 2.9. The HLT consist of a software application that runs on a dedicated computing farm. It reduces the rate of accepted events to about 5 kHz, and all such events are written to storage. The events written to storage are processed with a more accurate alignment and calibration of sub-detectors, and with reconstruction software that is more elaborate and allows for more redundancy than is possible in the HLT. This last part of reconstruction and subsequent event selection will be referred as off-line reconstruction and selection.

[2] In Run2 the trigger system workflow is slightly different [31]

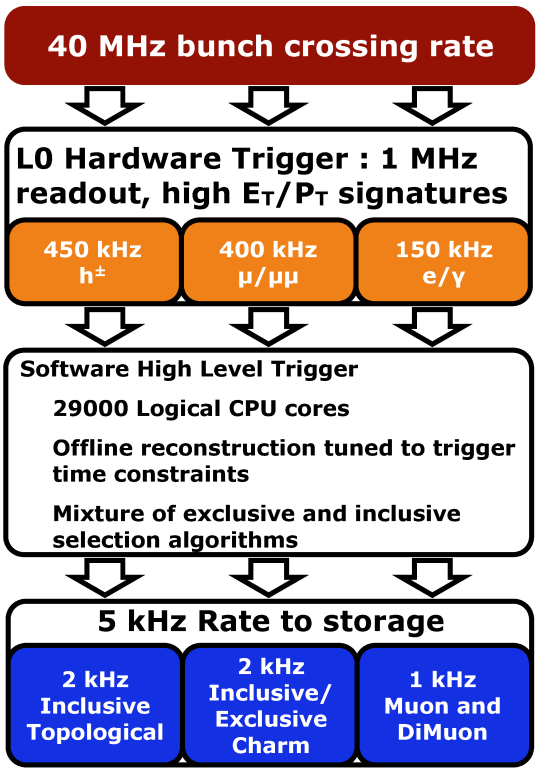

Fig. 2.9 Logical sketch of the LHCb trigger.

2.6.1 L0 trigger

To achieve the goal of rate reduction a decision has to be reached by the hardware implementation in under 4μs. The L0 trigger decisions are based exclusively on information from the muon system and calorimeters, as these are the only pieces of information available at such high rate. Events with either high p_T muons or large transverse energy deposits in the calorimeter are selected by the L0 trigger. The muon trigger selects events containing either a single muon with $p_T > 1.76\,\text{GeV}/c$ or a pair of muons with $p_{T,1} \times p_{T,2} > (1.6\,\text{GeV}/c)^2$. The relative momentum resolution for muons reconstructed using exclusively information from the muon chamber is 20%. The output rate of the L0 muon trigger is about 400 kHz. The hadron trigger selects events in which a significant amount of transverse energy ($E_T > 3.68\,\text{GeV}$) is deposited in the hadronic calorimeter. Electrons and photons trigger the event selection by a deposit of $E_T > 3\,\text{GeV}$ in the electromagnetic calorimeter. The output rates of the hadron and electromagnetic triggers are 450 kHz and 150 kHz, respectively. In the L0 trigger there are several types of objects, e, γ/π^0, h, μ and $(\mu\mu)$, that can fire for the event to be triggered on. The corresponding L0 trigger lines are `L0Electron`, `L0Photon`,

L0Hadron, L0Muon and L0Dimuon. In the analysis discussed in this thesis L0Hadron and a global event trigger called L0Global are used (described in the Sec. 3.4).

The events are selected in two independent ways by the hardware trigger:

- *TOS*: the signal candidate triggers the L0 trigger lines (trigger on signal, TOS);
- *TIS*: Any particle in the event, irrespective if it is part of the signal candidate or not, passes any of the L0 trigger lines (trigger independent of signal, TIS).

2.6.2 The software trigger

The software trigger of LHCb, referred to as the HLT, is made of two stages: HLT1 and HLT2. Whereas a partial reconstruction is performed at the HLT1 level using information from the vertexing and tracking system, a full reconstruction of the event is made at HLT2 level using information from all the subdetectors. The HLT1 performs the reconstruction of the primary vertices (PVs) and the search for secondary vertices. A preliminary track reconstruction is also performed. PVs are reconstructed by searching for five tracks coming from the same point with an uncertainty of $\pm 300 \mu$m along the z axis. The track impact parameter with respect to the primary vertex can be determined and used to reject events. The vertex corresponding to the minimum IP value is set as the origin vertex of the track, Therefore, it is possible to determine if the track is originating from a primary or a secondary vertex. The quality of the vertex reconstruction is also computed from the number of hits in the VELO used to reconstruct the track. This vertex quality is expressed as a χ^2 value. High p_T tracks are also reconstructed at the HLT1 level. A preliminary measurement of the tranverse momentum of the tracks is done using the residual magnetic field in the TT stations. A full reconstruction of the event is done at the HLT level which is completely configurable. A large number of selection lines in the HLT2 trigger selection are tailored for specific physics analyses. There are exclusive lines dedicated to a particular decay as well as inclusive lines based on topological requirements. The selections applied by these lines are either simples cuts or more complex methods using multivariate analyses such as Boosted Decision Trees. The HLT-trigger reduces the incoming 1 MHz rate at the output of the L0-trigger to a few kHz rate which is recorded on disk.

2.7 LHCb software

The detection of proton-proton collisions in LHCb is only the first step to perform physics analysis. In the following some information are given about the simulation, the reconstruction and other technicalities useful to perform analyses within the LHCb experiment.

The production of simulated Monte Carlo (MC) samples involves several phases such as generation, digitisation, reconstruction and several software packages are involved. The first three steps are unique of the MC production, the reconstruction is in common with the real data taking.

The software framework Gaudi [32] is used for the generation and data processing. It ensures availability of all LHCb tools and algorithms across the experiment and enforces global consistency of LHCb analyses. Its main components can be separated in:

- Generation: The LHCb software package Gauss [33] is responsible for the generation of Monte Carlo (MC) simulation data. In this step, the primary *pp* beams collisions are generated using PYTHIA [34] and the decays of b hadrons are simulated with the EvtGen package [35].

- Simulation: The interaction of the generated particles with the detector is simulated with Geant4 toolkit [36].

- Digitisation: The response of the LHCb detector to the generated particles is handled by the Boole application [37]. The digitised output is the MC equivalent of real measured data. From this point, both data and MC pass through the same reconstruction chain.

- Reconstruction (see Sec. 2.7.1): The Brunel application [38] handles the reconstruction of the digitised output of the detector responses. Signal hits in the detector are clustered and associated tracks are constructed. Particle properties such as momentum are determined and PID (Particle Identification) measurements are performed. The output of Brunel is a full reconstructed dataset stored in "Data Storage Tape" (DST) files.

- Analysis: Offline analyses are performed using the DaVinci software package [39]. The DaVinci application allows for reconstructed particles to be combined and determines primary and secondary vertices as well as kinematic quantities, such as invariant masses of decayed particles and their distance of flight.

Individual algorithms store their produced data in a Transient Event Store (TES), which is consecutively used as an input location for the following process. A global condition database containes all parameters required for the current running conditions of the experiment. A schematic overview of the LHCb processing applications and data flow is shown in Fig. 2.10.

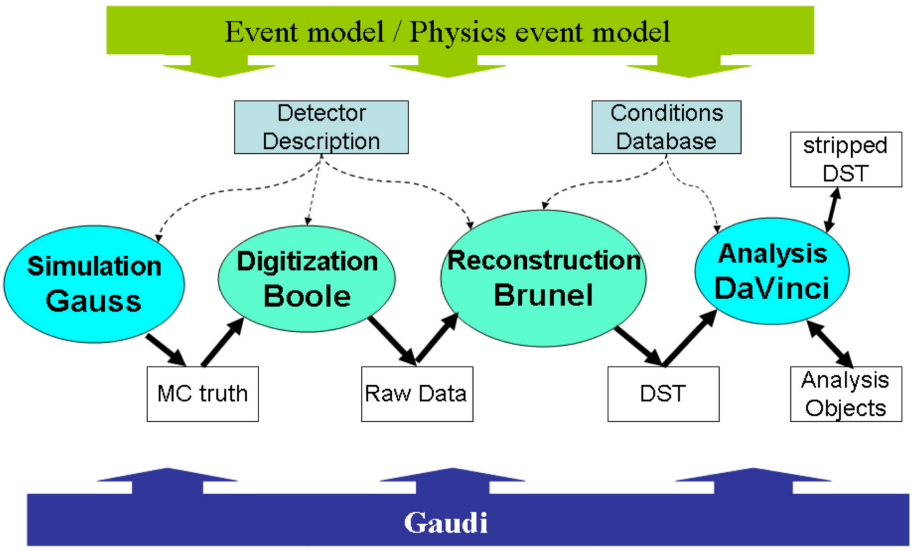

Fig. 2.10 The LHCb data processing applications and data flow. Underlying all of the applications is the Gaudi framework and the event model describes the data expected. The arrows represent input/output data.

2.7.1 Track reconstruction

The tracks (the trajectories of charged particles) are reconstructed in LHCb combining the hits (measured positions of the intersections between tracks and detectors) coming from different tracking detectors (VELO, TT, IT, and OT). Not all charged particles will leave hits in all subdetectors: some are produced in the backward direction and leave hits only in the VELO before flying outside the LHCb acceptance[3], other low-momentum particles are deflected outside the acceptance by the magnet, while particles coming from the decay of neutral long-lived particles such as K_S^0 or Λ are often produced after the VELO and hence leave hits only in the tracker. The track reconstruction must accommodate these different possibilities, get a high efficiency in finding the tracks and, at the same time, have a low probability of reconstructing spurious tracks known as ghosts (*ghost tracks*). Figure 2.4 shows a schematic illustration of the various types of tracks. The reconstruction of the tracks is divided in different steps:

1. The first step of the track reconstruction is the *pattern recognition* in which independently in the VELO and in the T stations sequences of hits are grouped together and identified as coming from the same track. These VELO tracks and T tracks are then used as input to find long, upstream and downstream tracks. The long tracks

[3]Those tracks are crucial in the reconstruction of the primary vertices

are found either by extrapolating the VELO tracks into the T station and looking for matching hits, or by matching directly the VELO tracks with T tracks; TT hits are then added. Upstream tracks are found by extrapolating VELO tracks into the TT while the downstream tracks combine T tracks with TT information.

2. The second step of the track reconstruction is the track *fitting* that in LHCb is done with a *Kalman filter*[40] that takes into account effects from multiple scattering and energy loss due to ionisation.

3. Ghost tracks are then removed based on the *ghost probability*, the output of a neural network that takes as input various variables such as the track χ^2 and the number of hits in each subdetector. The ghost probability response is calibrated on simulated events to be the rejection rate of ghost tracks (*e.g.* 30% of all the ghost tracks have a ghost probability of less 0.3).

4. The last step of the track reconstruction is the *clone killing* which consists of removing tracks that are also subtracks of other tracks, for example a VELO track used to build a long track.

The reconstruction efficiency for charged tracks that pass through the full tracking system varies as function of the kinematics of the tracks and the occupancy of the detector. It is above 95% as shown in Fig. 2.11.

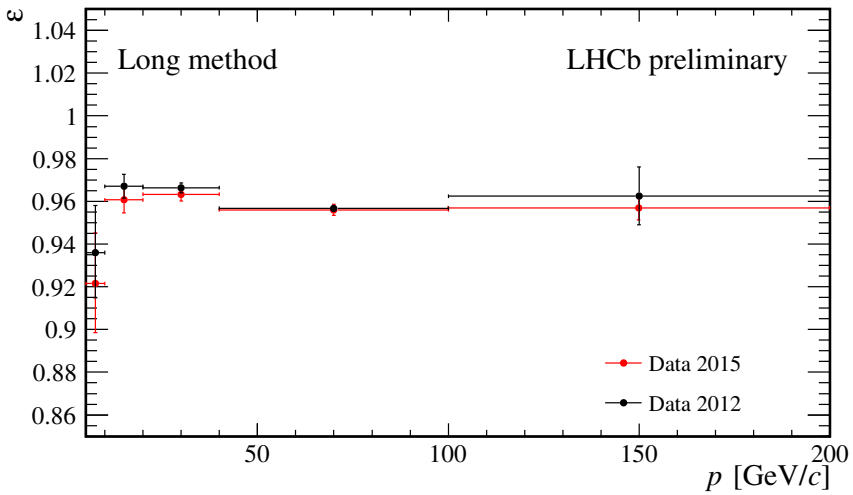

Fig. 2.11 Track reconstruction efficiency for long tracks for 2012 and 2015, nominal data taking period.

2.7.2 Particle identification

Particle identification (PID) at LHCb is performed using information from the RICH detectors, the calorimeter system and the muon system. The PID of a single track can be obtained in a Cherenkov detector by measuring the Cherenkov angle and knowing the momentum of the track. Since the most abundant particles in *pp* collisions are pions, the general approach is a likelihood minimisation procedure that starts by assuming all particles are pions. The overall event likelihood, computed from the distribution of photon hits, the associated tracks and their errors, is then calculated for this set of hypotheses. Then, for each track in turn, the likelihood is recomputed changing the mass hypothesis to e, μ, π, K and proton, whilst leaving all other hypotheses unchanged. The change in mass hypothesis amongst all tracks that gives the largest increase in the event likelihood is identified, and the mass hypothesis for that track is set to its preferred value. This procedure is then repeated until all tracks have been set to their optimal hypotheses, and no further improvement in the event likelihood is found. In LHCb these variables are called PIDK, PIDp etc. where the first mass hypothesis tested is that of a kaon or a proton while the second mass hypothesis is always a pion.

A second class of PID variables are commonly used: ProbNNx. They are the output of a neural network that takes as an input the various PIDx variables and also complementary information from all the subdetectors including the tracking detectors. The output is a variable between zero and one that can be interpreted as absolute probability of a particle to have a certain PID. On average the efficiency to correctly identify a kaon is $\sim$95% with a misidentification probability to identify a pion as a kaon of $\sim$5%[41] (Figure 2.12).

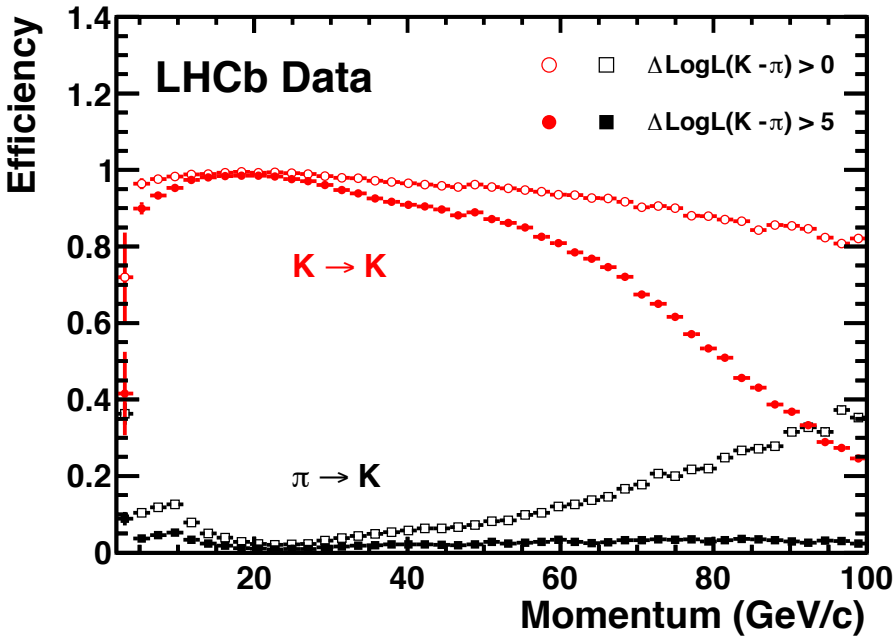

Fig. 2.12 Kaon identification efficiency and pion misidentification rate as measured using data, as a function of track momentum. Two different $\Delta log\mathscr{L}(K-\pi)$ requirements have been imposed on the samples, resulting in the open and filled marker distributions, respectively.

The identification of a track as a muon is mainly based on the muon system. A boolean variable called `isMuon` is set to true based on the association of hits around the extrapolated trajectory of the track in the muon system. A search is performed within rectangular windows; the size of these windows in each muon station and the number of stations required to have hits are optimised to maximise the efficiency and, at the same time, provide low misidentification probabilities. On average the probability to correctly identify a muon is $\sim$97% (shown in Fig. 2.13), with a probability to misidentify a hadron (pion, kaon or proton) as a muon is between 1% and 3%.

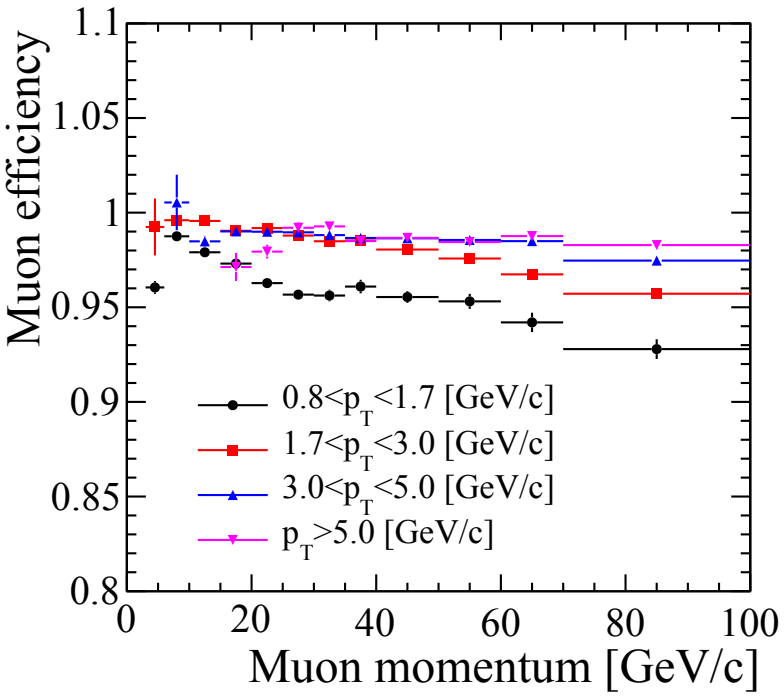

Fig. 2.13 Efficiency of the muon candidate selection based on the matching of hits in the muon system to track extrapolation, as a function of momentum for different p_T ranges.

2.7.3 Selection

In an LHCb analysis the selection usually involves three steps:

- **trigger selection**: decides which events are interesting enough to be saved for later analysis. Details of the LHCb trigger have been given in Sec. 2.6;
- **stripping selection**: is the centralised selection of interesting events after the reconstruction. A *stripping line* contains the instructions for reconstructing the particles of interest from the reconstructed stable particles and the corresponding selections to be applied. A group of stripping lines selecting similar events is collected into a *stream* and their output is saved in a common file;
- **offline selection**: is the term used to refer to the end-user selection on the events which passed trigger and stripping selections.

The trigger and stripping selections used in this analysis are detailed in Chapter 3. The offline selection criteria are discussed in Chapter 4.

Chapter 3

Data and Simulation

3.1 Monte Carlo and data samples

This analysis is performed on the full dataset collected by LHCb in pp collisions during the first run (Run1) of the LHC, corresponding to an integrated luminosity of $3fb^{-1}$ ($1fb^{-1}$ at $\sqrt{s} = 7$TeV in 2011 and $2fb^{-1}$ at $\sqrt{s} = 8$TeV in 2012). A number of simulated samples are used in order to understand and parametrize backgrounds, and to evaluate signal efficiencies during the various analysis steps. In all generated samples, the six charged tracks considered in this analysis, i.e., the pion from the D^{*-} decay, the kaon and the pion from the $\bar{D}^0$ decay, and the three additional pions, are required to be within the LHCb acceptance. These samples have been generated for 2011 and 2012 detector conditions. Signal events, where the τ lepton decays in three charged pions and a neutrino, are generated according to the TAUOLA model [42, 43]. Another sample of $B^0 \to D^{**-}\tau^+\nu_\tau$ is used to study contributions from decays involving excited charm mesons. A sample corresponding to the normalization mode $B^0 \to D^* 3\pi$ is also used.

The simulated background modes include an inclusive $b\bar{b}$ sample where b-hadron decays in final states containing a D^{*-} meson and three charged pions plus anything else are generated, reconstructed and filtered. Other than requiring particles in the LHCb acceptance, the filtering step also includes soft kinematic cuts on the momentum and transverse momentum of the daughter particles (to be greater than 1 GeV/c and 150 MeV/c respectively, except for the transverse momentum of the soft pion which has to be greater than 100 MeV/c) and the D^0 (greater than 1.5 GeV/c). This sample includes also signal and other backgrounds due to semi-inclusive $B \to D^* D_{(s)}^{(*),+,0}$ decays. Other semi-inclusive samples are generated and filtered, where B^0, B^+ and B_s^0 generically decay to $D^* X_c$ with $X_c = D^0$, D^+, D_s^+, D_{sJ} or D^+K^0, which subsequently give three charged hadrons and extra particles in the final state, either through de-excitation or decay of the ground stated meson.

The filtering steps in the above inclusive and semi-inclusive samples, require that the generated and simulated events pass the stripping selection criteria (Sec. 3.3). Either, two trigger lines L0Muon [44] or L0Hadron are required. For the HLT1, the single track trigger or the muon lines are required, while the topological HLT2 line [45] must have fired (HLT2 lines used in the analysis are explained in Sec. 3.4.3). The events satisfying the above criteria are then written on storage.

3.2 Reweighting of signal decay

3.2.1 Form factors

Signal samples were generated with the ISGW2 model [46], which does not fully reproduces the differential distribution in terms of the kinematical variables of the decay. A reweighting of events is therefore performed in order to match the distributions predicted by the CLN parameterization [21], which is more accurate nd widely used. The XslFF package [47] is used to implement such a reweighting. The values of the form factor ratios $R_1(1) = 1.404 \pm 0.032$ and $R_2(1) = 0.854 \pm 0.020$ at zero recoil, as well as the slope of the Isgur-Wise function $\rho^2 = 1.205 \pm 0.015 \pm 0.021$, are taken from their world averages, including their correlations $\rho(\rho^2, R_1) = 0.566$, $\rho(R_1, R_2) = -0.759$, $\rho(R_2, \rho^2) = -0.807$. The calculation shown in Ref [6] is used to compute the scalar form factor ratio at zero recoil and its uncertainty $R_0(1) = 1.14 \pm 0.11$. The effect of signal events reweighting from ISGW2 to the CLN parameterization is shown in Figure 3.1, for MC truth variables. The angular variables and the τ momentum do not change appreciably, while the shapes of the momentum transferred to the $\tau^+\nu_\tau$ system, q^2, and the invariant $D^{*-}\tau^+$ mass distribution are affected.

3.2.2 PID reweighting

A correction to the Monte Carlo samples has been made in order to match the Particle Identification (PID) performance observed on data. This has been made using the PIDCalib tool [48] within the LHCb analysis framework, which provides access to the calibration samples of electrons, muons, pions, kaons and protons. This tool is used to perform two different tasks:

- production of weights per event for given PID requirements
- apply corrections to PID variables in MC samples

The cuts considered for the reweighting are:

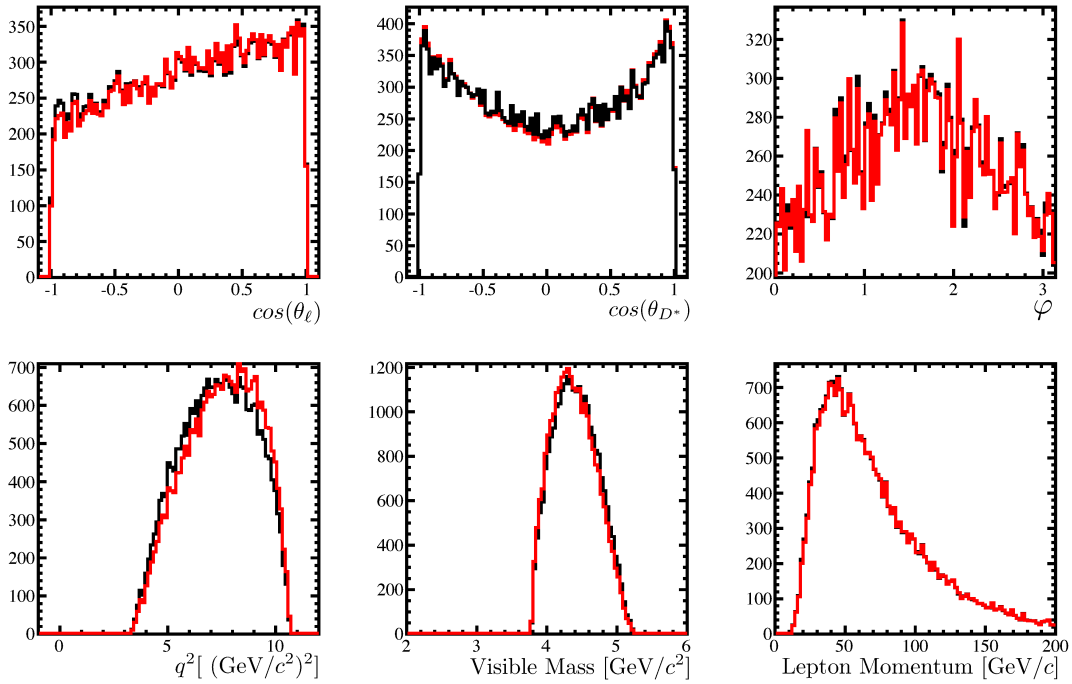

Fig. 3.1 Distribution of angular variables (top plots: helicity angle of the τ, left, helicity angle of the D^*, middle and azimut ϕ, right), q^2 (bottom left), invariant $D^*\tau$ mass (bottom middle) and τ momentum (bottom right) before (black histograms) and after (red histograms) form factor reweighting.

- $ProbNNpi > 0.6$ for the three pions coming from the τ candidate (this cut is a good compromise between purity and efficiency for the standard pions);
- $ProbNNpi > 0.1$ for the pion coming from the D^* (the soft pion is quite pure and has a low efficiency a softer cut is applied);
- $ProbNNk < 0.1$ for the pion coming from the τ with charge opposite with respect to the other two (the negative pion has a lot more potential contamination than the other two due to $K^-\pi^+\pi^+$ decays of the D^+ so we a tighter cut is applied).

In order to perform cross-checks of the performance of the PID cuts on a sample enriched with real kaons, the extraction of the weights reverting the PID cuts ($ProbNNk > 0.1$ and $ProbNNpi < 0.6$ for the opposite charge pion) is also computed. The high purity kaons sample can be demonstrated by the small combinatorial background present in the distribution (Fig.3.2).

The validity of the procedure has been tested by performing several comparisons. In Figs. 3.3, 3.4, both the original and corrected PID variables are shown for the 2012 Monte Carlo exclusive $D^*3\pi$ sample and the corresponding distribution from data. In both cases, candidates corresponding to the $B^0 \to D^*3\pi$ exclusive decay have been selected by an invariant mass cut around the B^0 mass. Figs. 3.5, 3.6 show the same distributions in the case of $D^0 \to K^-\pi^+\pi^-\pi^+$ decay. All these plots are shown with pull distribution defined as $\frac{X^{corr}-X^{data}}{X^{data}}$.

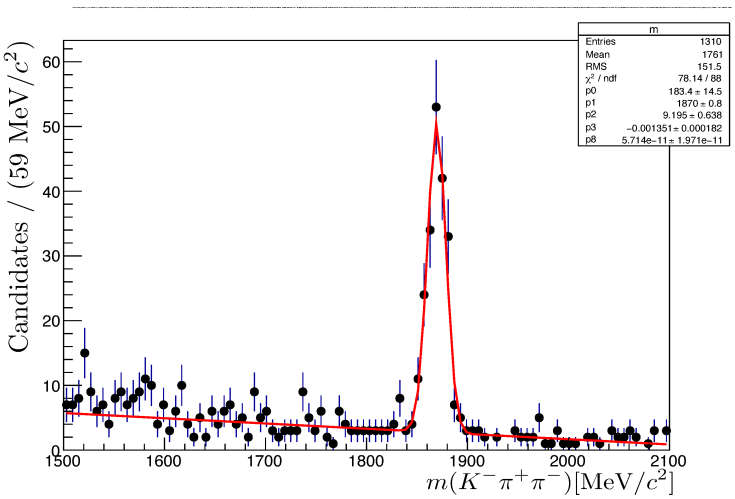

Fig. 3.2 $K^-\pi^+\pi^+$ mass distribution for events in the Run1 dataset with a selection equivalent to the final data set, except that the pion candidate with charge opposite to that of the 3π system has ProbNNk above 0.1., and ProbNNpi<0.6

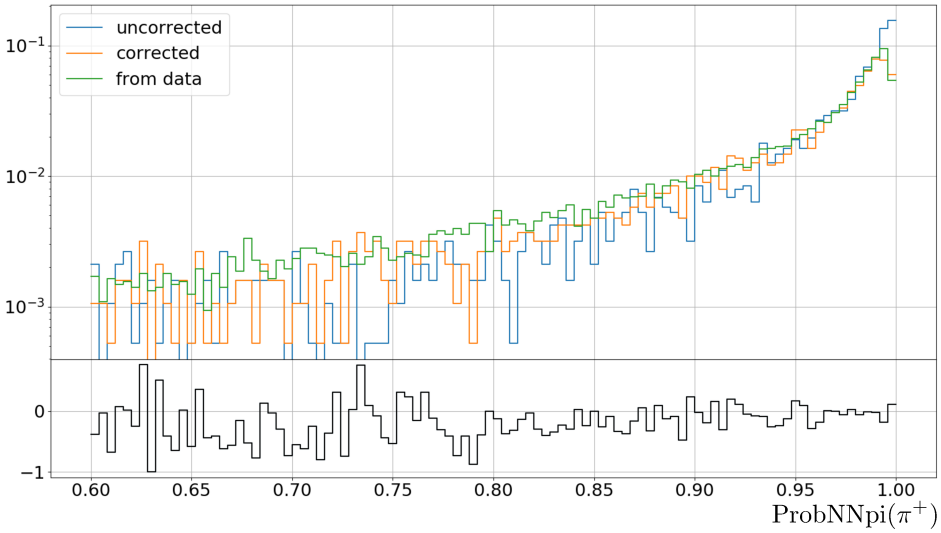

Fig. 3.3 Corrected (orange), uncorrected (blue) and data (green) `ProbNNpi` for the same sign pion (π^+) in 2012 for the exclusive $B^0 \to D^*3\pi$ peak. Pulls are defined as $\frac{X^{corr} - X^{data}}{X^{data}}$.

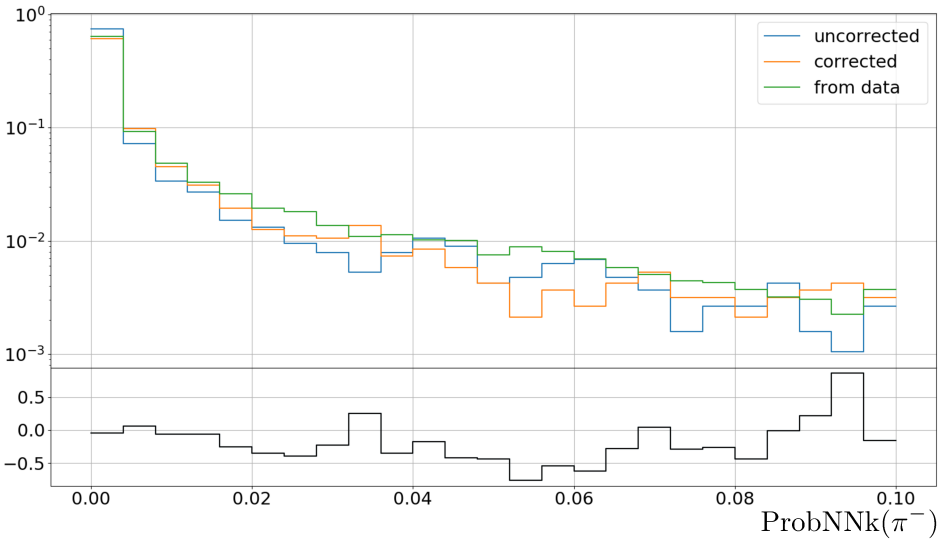

Fig. 3.4 Corrected (orange), uncorrected (blue) and data (green) `ProbNNk` for the opposite sign pion (π^-) in 2012 for the exclusive $B^0 \to D^*3\pi$ peak. Pulls are defined as $\frac{X^{corr} - X^{data}}{X^{data}}$.

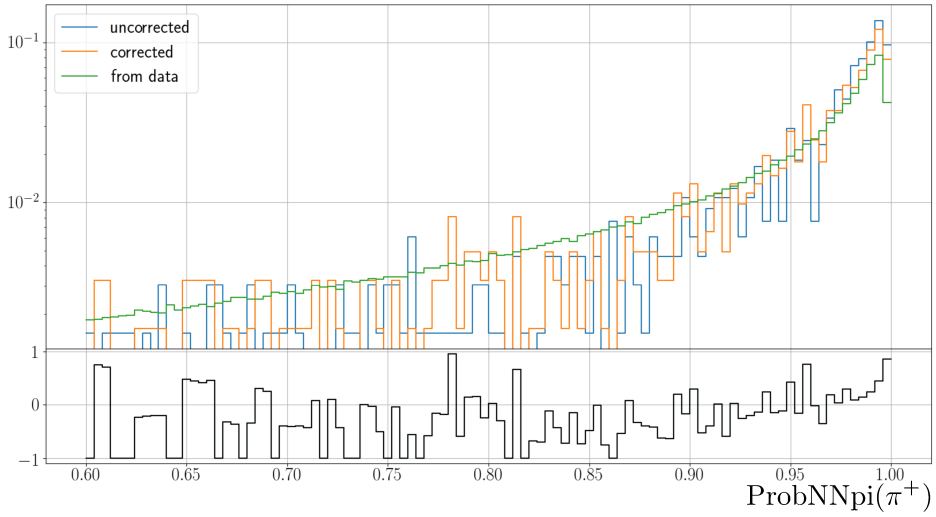

Fig. 3.5 Corrected (orange), uncorrected (blue) and data (green) `ProbNNpi` for the same sign pion (π^+) in 2012 for the exclusive $D^0 \to K^0 3\pi$ peak. Pulls are defined as $\frac{X^{corr}-X^{data}}{X^{data}}$.

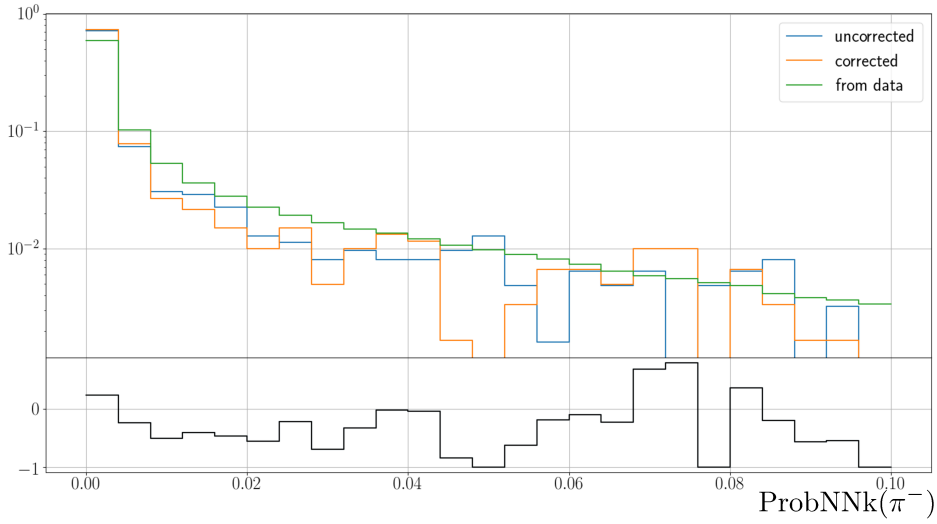

Fig. 3.6 Corrected (orange), uncorrected (blue) and data (green) `ProbNNk` for the opposite sign pion (π^-) in 2012 for the exclusive $D^0 \to K^0 3\pi$ peak. Pulls are defined as $\frac{X^{corr}-X^{data}}{X^{data}}$.

3.3 Stripping

The complete set of cuts used in the used stripping line are shown in Table 3.1.

Cut	Value
B^0	
$m(D^*\pi\pi\pi)$	2500-5600 MeV/c^2
DIRA	> 0.995
Max. DOCA	< 0.15 mm
D^*	
p_T	> 1250 MeV/c
Vertex χ^2/DOF	< 25
$m(D^* - D^0)$	135-150 MeV/c^2
$m(D^0\pi)$	1960-2060 MeV/c^2
D^0	
p_T	> 1600 MeV/c
Vertex Distance χ^2	> 50
DIRA	> 0.999
Vertex χ^2/DOF	< 10
$m(K\pi)$	1825-1905 MeV/c^2
Max. DOCA	< 0.5 mm
Max. DOCA χ^2	< 15
τ	
m($\pi\pi\pi$)	400-3500 MeV/c^2
min[m($\pi\pi$)]	< 1670 MeV/c^2
DIRA	> 0.99
Vertex χ^2	< 25
Max. DOCA	< 0.15 mm
At least two pions p_T	> 300 MeV/c^2
At least two pions IP χ^2	> 5
τ daughter pions	
p_T	> 250 MeV/c
IP χ^2	> 4
Track χ^2/DOF	< 3
PIDK	< 8
Ghost probability	< 0.4
D^0 daughters	
p_T	> 250 MeV/c
p	> 2000 MeV/c
$p_T(K) + p_T(\pi)$	> 1200 MeV/c
Kaon PIDK	> -5
Pion PIDK	< 8
Track χ^2/DOF	< 3
IP χ^2	> 4
Ghost Probability	< 0.4
Slow Pion	
p_T	> 110 MeV/c
Track χ^2/DOF	< 3
Ghost Probability	< 0.6

Table 3.1 Cuts used in the stripping selection. The variables DIRA, Max. DOCA, IP χ^2 correspond respectively to the cosine of the angle between the momentum of the particle and the direction of flight from the best PV to the decay vertex, the maximum distance of closest approach between all possible pairs of particles and the χ^2_{IP} on the related PV.

The efficiencies of the stripping selection on $B^0 \to D^{*-}3\pi$, $B^0 \to D^{*-}\tau^+(\to 3\pi)\nu_\tau$ and $B^0 \to D^{*-}\tau^+(\to 3\pi\pi^0)\nu_\tau$, evaluated on Monte Carlo, are equal to 1.289%, 0.823% and 0.757% respectively. In order to explain the difference of the stripping efficiency between signal and normalization, the efficiencies in the intermediate steps are reported in

Table 3.2. The step which mostly affects the stripping efficiency difference between signal and normalization is the selection of the D^* and the 3π, since the kinematics of the slow pion and the 3π system are different between the two channels.

Intermediate step	ε_{sig} (%)	ε_{norm} (%)	$\varepsilon_{sig}/\varepsilon_{norm}$	Relative eff.
D^0 selection	55.4	56.0	0.988	0.988
D^* candidates	25.6	27.9	0.917	0.929
D^* selection	18.6	21.7	0.856	0.933
3π candidates	25.5	28.6	0.891	0.891
3π selection	16.4	18.4	0.891	1
D^* 3π candidates	8.9	11	0.81	–
D^* 3π selection	2.6	3.4	0.76	0.94
`Hlt1` selection	0.826	1.382	0.598	0.96

Table 3.2 List of efficiencies of each intermediate step in stripping selection.

3.4 Trigger

The trigger [49] consists of a hardware stage, based on information from the calorimeter and muon systems, followed by a software stage, in which all charged particles with $p_{\mathrm{T}} > 500\,(300)\,\mathrm{MeV}$ are reconstructed for 7 TeV (8 TeV) data. At the hardware trigger stage, candidates are required to have a muon with high p_{T} or a hadron, photon or electron with high transverse energy. The software trigger requires a two-, three-, or four-track secondary vertex with significant displacement from any PV consistent with the decay of a b hadron, or a two-track vertex with a significant displacement from any PV consistent with a $\bar{D}^0 \to K^+\pi^-$ decay. In both cases, at least one charged particle must have a transverse momentum $p_{\mathrm{T}} > 1.7\,\mathrm{GeV}/c$ and must be inconsistent with originating from any PV. A multivariate algorithm [50] is used for the identification of secondary vertices consistent with the decay of a b hadron. Secondary vertices consistent with the decay of a $\bar{D}^0$ meson must satisfy additional selection criteria, based on the momenta and transverse momenta of the $\bar{D}^0$ decay products ($p > 5\,\mathrm{GeV}/c$ and $p_{\mathrm{T}} > 800\,\mathrm{MeV}/c$), and on the consistency, as a loose requirement, of the $\bar{D}^0$ momentum vector with the direction formed by joining the PV and the B^0 vertex.

In this analysis the following trigger requirements have to be satisfied:

- TOS Hadron trigger on the D^* candidate (called `L0_Hadron_TOS`) or TIS trigger on B^0 candidate (called `L0_Global_TIS`);

- HLT1 trigger executed for all events accepted by L0 and that have at least one track that satisfies a number of track quality criteria [51] (called `Hlt1TrackAllL0`), required on the stripping line;
- HLT2 topological line that requires two-, three-, or four-track secondary vertex with significant displacement from any PV consistent with the decay of a b hadron, or a two-track vertex with a significant displacement from any PV consistent with a $\bar{D}^0 \to K^+\pi^-$ decay.

The properties of the L0Hadron trigger can be studied using the TIS-TOS method in which the efficiency of the L0 hadronic trigger line can be computed as:

$$\varepsilon_{TOS} = \frac{\eta_{TIS\&TOS}}{\eta_{TIS}}$$

where η_{TIS} is the number of candidates selected by the TIS trigger line and $\eta_{TIS\&TOS}$ is the number of events selected by both.

In our case the L0 trigger is about splitted equally between B0_L0Global_TIS and B0_L0Hadron_TOS events. The events under study in addition must have passed the HLT2 triggers.

3.4.1 L0 trigger efficiency

The main driver of the efficiency of the L0Hadron trigger is the 3π system transverse momentum. Fig. 3.7 shows the efficiency of the L0Hadron trigger as function of this transverse momentum rising almost linearly from 20% to 100% for transverse momentum range from 1 to 15 GeV/c. The efficiency is measured on data (black) and MC (red) using a D_s^+ sample reconstructed in the 3π mode in the detached vertex topology (described in Sec. 4.1). The agreement between data and MC is good at high p_{T} but not at low p_{T} (Fig. 3.8). The same pattern can be seen when measuring the efficiency with the D^* 3π samples, but the disagreement at low p_{T} is smaller. The ratio between the two efficiencies partially cancel these differences. To measure the correction factor due to the partial cancellation, the efficiency of the L0Hadron trigger as been computed using the TIS-TOS method as function of the SPD multiplicity described in Sec. 3.4.2.

3.4.2 L0 trigger efficiency correction due the SPD multiplicity

The L0 trigger efficiency for L0Hadron_TOS and L0Global_TIS events is determined as a function of the number of hits in the SPD detector. To perform this study, events at the

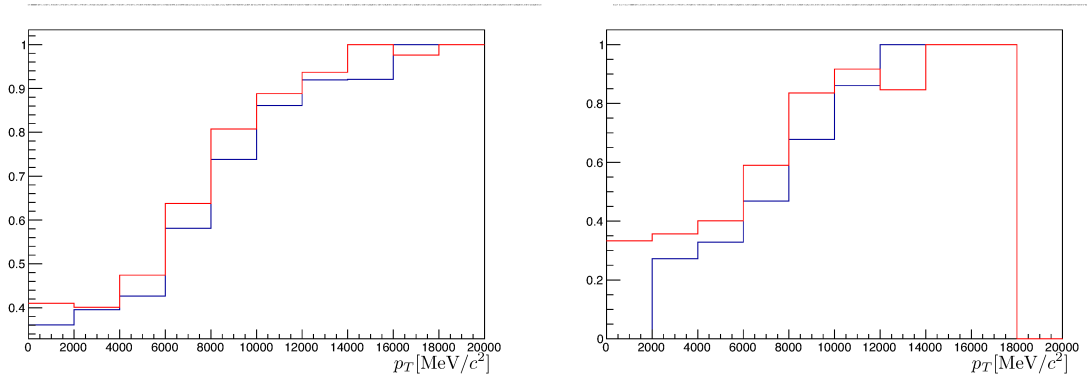

Fig. 3.7 Efficiency for L0 Hadron trigger as function of the transverse momentum of the 3π system, measured using the $B^0 \to D^{*-}\ 3\pi$ exclusive channel (left) and the $B^0 \to D^{*-} D_s^+; D_s^+ \to 3\pi$ (right). The red and black curves correspond to MC simulation and data, respectively.

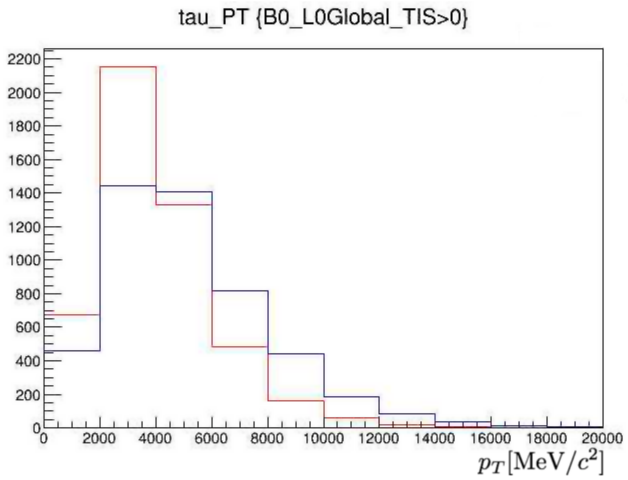

Fig. 3.8 Distribution of the transverse momentum of the 3π system for $D^{*-}\tau^+\nu_\tau$ signal events in red , superimposed with the 3 π transverse momentum distribution from $B^0 \to D^{*-}\ 3\pi$ events (black)

$B^0 \to D^{*-}3\pi$ exclusive peak are selected in data and Monte Carlo. The efficiencies as a function of SPD multiplicity for the two triggers are determinated by computing:

$$\varepsilon_{\texttt{L0Hadron\_TOS}} = \frac{\texttt{L0Hadron\_TOS \&\& L0Global\_TIS}}{\texttt{L0Global\_TIS}} \tag{3.1}$$

$$\varepsilon_{\texttt{L0Global\_TIS}} = \frac{\texttt{L0Hadron\_TOS \&\& L0Global\_TIS}}{\texttt{L0Hadron\_TOS}}. \tag{3.2}$$

In order to match the efficiencies observed in data, the L0Hadron_TOS efficiency must be multiplied by a factor 0.93 and the L0Global_TIS efficiency by a factor 1.12, due to a mismatch bewtween data and MC L0Hadron trigger efficiency as function of the multiplicty of the event which good estimator is the number of SPD hits [51]. Since the fraction of L0Global_TIS events in signal and normalization are different, this correction translates to a factor of 0.97 ± 0.01 in the ratio $\frac{\varepsilon_{norm}}{\varepsilon_{sig}}$.

In Fig. 3.9, the SPD multiplicity is shown for data and MC (exclusive $B^0 \to D^{*-}3\pi$ simulation). On the top figure, the data and MC SPD multiplicity distributions are compared for all events (black), L0Hadron_TOS (red), L0Global_TIS (green) and L0Hadron_TOS && L0Global_TIS (blue). In the middle figure, the number of hits in the SPD detector is scaled by a factor 1.4 in order to match the shape observed on data. In the bottom figure, the L0Hadron_TOS and L0Global_TIS trigger efficiencies are corrected by the factors 0.93 and 1.12, respectively. Those factors are used to reweight the Monte Carlo in order to match the data.

3.4.3 HLT2 trigger efficiency

In the analysis, events are selected to pass any topological trigger line [52]. In addition, two different HLT2 trigger requirements are exploited, based on the D^* candidate and on the topological trigger of the B candidate. The former uses tight cuts to identify the D^* decay chain and especially to select the D^0 decay, whereas the topological trigger on the B candidate is based on the D^0 selection and a global event topology, characteristic of two-, three- or four-body B decays. Fig. 3.10 show the D^0 mass peak for the D^0 trigger in red and topological trigger in blue after the stripping requirements. The D^0 tail is smaller for the D^0 trigger than for the Topo trigger. The two trigger lines select a large fraction of common events but have also significant distinct contributions, as can be seen in Tab 3.3, which shows the number of selected events by each trigger line on the $B^0 \to D^{*-}\tau^+\nu_\tau$ signal Monte Carlo. The efficiency of the topological trigger is significantly larger than that of the D^0 trigger.

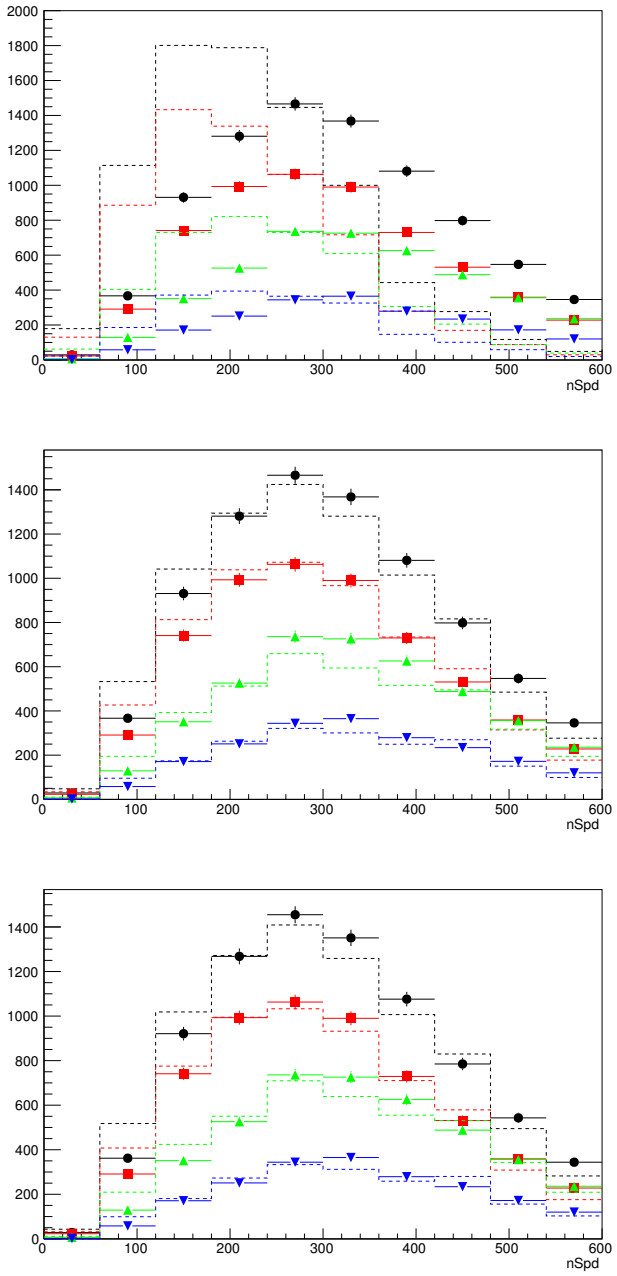

Fig. 3.9 Comparison between the SPD multiplicity between data (full points) and Monte Carlo (dashed histograms). In each figure, the total number of events is shown in black, the `L0Hadron_TOS` are shown in red, the `L0Global_TIS` in green and `L0Global_TIS && L0Hadron_TOS` events are shown in blue (full points data, dashed histogram MC). Top: SPD multiplicity without any correction. Middle: the SPD multiplicity in Monte Carlo is scaled by a factor 1.4. Bottom: `L0Hadron_TOS` and `L0Global_TIS` efficiencies in the Monte Carlo are corrected in order to match the data.

Trigger line	Number of events	Efficiency
No Hlt2 trigger	29090	100%
`Topological`	18486	63.5%
D^0	14791	50.8%
`OR`	22059	75.8%

Table 3.3 Efficiency on signal Monte Carlo events of the various trigger lines after the stripping and cleaning cuts. For historical reasons, the any topological line requirement has not been applied when computing these numbers.

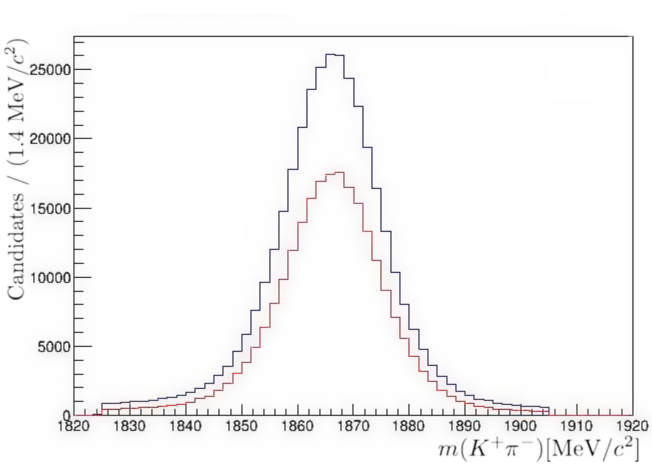

Fig. 3.10 $K^+\pi^-$ mass spectrum for the topological trigger (blue) and the D^0 trigger (red)

The efficiency of the HLT2 trigger lines has been measured on data and Monte Carlo by using the trigger L0Global_TIS on the B^0 (`B0_L0Global_TIS`). To study the trigger efficiency, the ratio

$$\frac{\texttt{N(trigger AND B0\_L0Global\_TIS)}}{\texttt{N(B0\_L0Global\_TIS)}}, \tag{3.3}$$

has been studied as a function of the D^{*-} 3π invariant mass (*B0_M*), the 3π invariant mass, the squared dilepton mass q^2, and the 3π decay time[1]. The last two variables are used in the fit which determines the signal yield on data. In the Eqn. 3.3, `N(trigger)` represents the number of events passing the HLT requirements and `N(B0_L0Global_TIS)` is the number of events passing the same trigger line, where the event is triggered independently of the signal (TIS). The complementarity of the topological and `Dstar` triggers is illustrated in Fig. 3.11, which shows the efficiency for the two trigger lines and their logical `OR` as function of q^2, 3π

[1]Defined later in Sec. 4.4.1.

mass, D^{*-} 3π invariant mass, and 3π decay time. The D^0 trigger efficiency drops as function of the 3π and D^* 3π masses and is very inefficient for the $D^{*-}D_s^+$ events. Reversely, the topological trigger efficiency is low at low masses. The reverse behaviour is observed as a function of q^2 and 3π decay time. Although trigger effects largely cancel out due to usage of the D^{*-} 3π normalisation channel, it is essential to have a trigger efficiency as flat as possible as function of the 3π mass. This is achieved by using the `OR` of these two trigger lines (green curve), which in addition enhances the trigger efficiency on the $D^{*-}\tau^+\nu_\tau$ signal with respect to the topological trigger by a significant amount, as shown in Table 3.3.

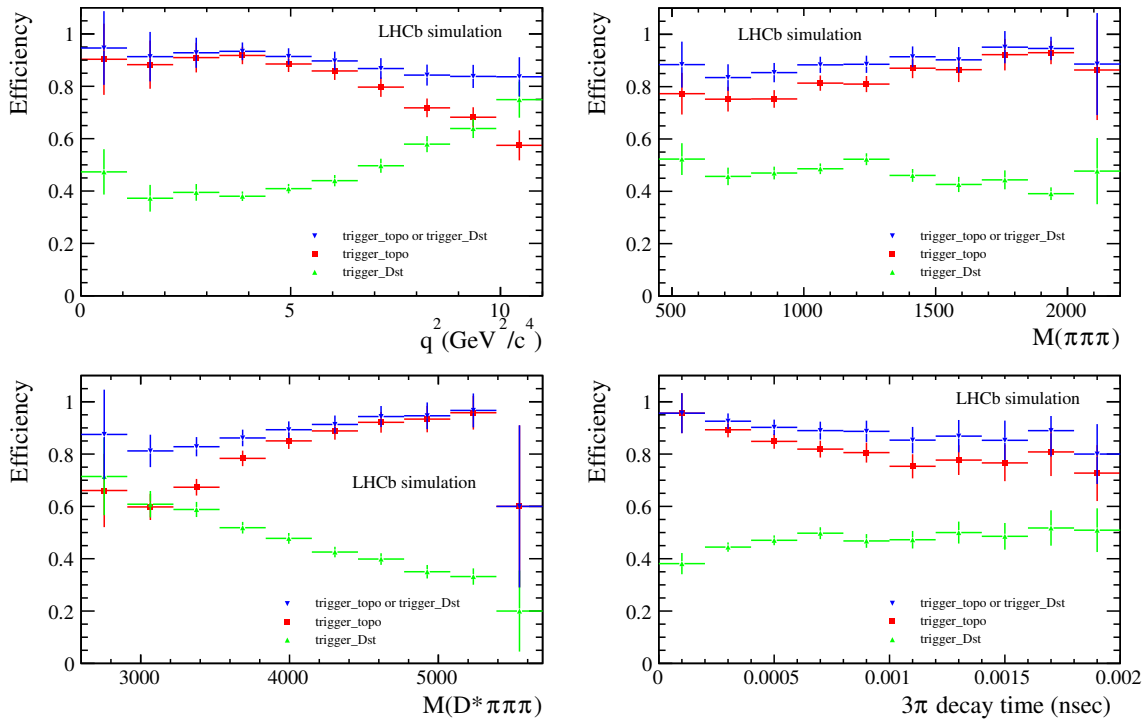

Fig. 3.11 Efficiency for different trigger requirements as a function of the transferred momentum, q^2, to the $\tau\nu_\tau$ system (top left), the 3π invariant mass (top right), the $D^*3\pi$ invariant mass (bottom left), and the 3π decay time (bottom right), for $D^*3\pi X$ inclusive Monte Carlo.

Figure 3.12 shows the trigger efficiency as a function of the examined variables, for data and Monte Carlo, as well as the ratio between the two efficiencies. A small variation of this ratio is observed, and a correction on the ratio of Monte Carlo efficiencies for signal and normalization is applied in order to match the data efficiency as follows. Since, in the normalization channel, all events have a D^{*-} 3π mass equal to the B mass of 5.279 GeV, one has to compute the ratio between the HLT2 trigger efficiency for that mass, and the average efficiency for signal events, obtained by convoluting the observed slope in Fig. 3.12 with the D^{*-} 3π mass distribution. Using the D^{*-} 3π mass distribution obtained on the signal sample

generated with `Tauola` tuned on BaBar experiment results [53], the convoluted average of the HLT2 efficiency is 0.9892 while the HLT2 efficiency for $B^0 \to D^{*-}\ 3\pi$ is 0.9895 when taking the central value for HLT2 variation as function of the $D^{*-}\ 3\pi$ mass, and the error on the slope to compute the error. The correction factor is thus equal to 1.000 ± 0.005.

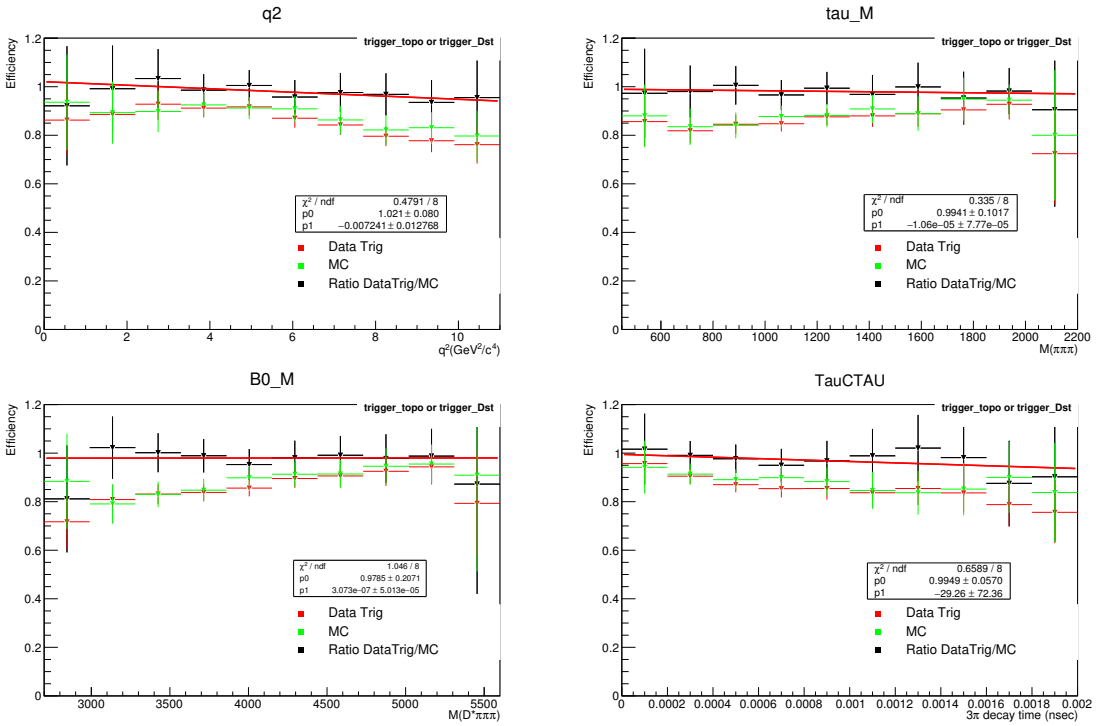

Fig. 3.12 Trigger efficiency as a function of q^2 (top left), 3π invariant mass (top right), $D^{*-}3\pi$ invariant mass (bottom left) and τ decay time (bottom right). Red and green dots represent data and inclusive $D^{*-}\ 3\pi$ Monte Carlo, respectively. Black dots represent the ratio between data and Monte Carlo while the red line is the result of a fit performed with a polynomial of order one.

Chapter 4

Selection criteria and multivariate analysis

The signal selection proceeds in two main steps. First, the dominant background, consisting of candidates where the 3π system originates from the B^0 vertex, called *prompt* hereafter, is suppressed by applying a 3π detached-vertex requirement. Second, the double-charm background (decays of the type $B^0 \to D^{*-}D^0, B^0 \to D^{*-}D^+, B^0 \to D^{*-}D_s^+$) is suppressed using a multivariate analysis (MVA). This is the only background with the same vertex topology as the signal.

This chapter is organized as follows. After a summary of the principles of the signal selection in Sec. 4.1, the categorization of the remaining background processes is given in Secs. 4.1.1 and 4.1.2. This categorization motivates the additional selection criteria that have to be applied to the tracks and vertices of the candidates in order to exploit the requirement of vertex detachment in its full power. The selection used for the normalization channel is described in Sec. 4.2. Section 4.3 describes the isolation tools used to take advantage of the fact that, for the $\tau^+ \to 3\pi\overline{\nu}_\tau$ channel, there is no other charged or neutral particle at the B^0 vertex beside the reconstructed particles in the final state. Section 4.4 details the kinematic techniques used to reconstruct the decay chains in the signal and background hypotheses. Finally, the MVA that is used to reduce the double-charm backgrounds is presented in Sec. 4.5 and, in Sec. 4.6, the background composition at various stages of the selection process is illustrated.

4.1 The detached-vertex topology

Two main categories of events have to be distinguished, depending on whether the 3π system comes from the same vertex (but not necessarily from the same parents) or one pion originates from a second different vertex. The former category can be split according to the origin of the 3π system: τ lepton, charmed mesons D^0, D^+ and D_s^+, or directly from a B particle such as B^0, B^+, B_s^0 or Λ_b^0. The dominant background in the analysis is $B^0 \to D^{*-}\pi^+\pi^-\pi^+X$ and is suppressed by a set of cuts, reported in Tab. 4.1. The most important cut is the first in the table, which will be referred to as *detached vertex cut*; it requires that the distance between the 3π and the B^0 vertices along the beam direction, $\Delta z \equiv z(3\pi) - z(B^0)$ (where the B^0 vertex is reconstructed using the DecayTreeFitter tool [54]), is greater than four times its uncertainty, $\sigma_{\Delta z}$. This leads to a rejection of the prompt background by three orders of magnitude, as shown in Fig. 4.1. The average B^0 decay length is 16 mm while the mean separation $B^0 - \tau$ is 3 mm. Some of the other cuts are topological, such as two requirements, one on the τ^+ flight

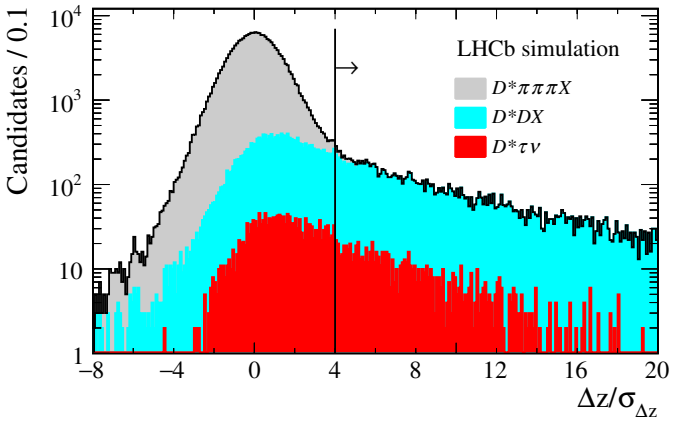

Fig. 4.1 Distribution of the distance between the B^0 vertex and the 3π vertex along the beam direction, divided by its uncertainty, obtained using simulation. The grey area corresponds to the prompt background component, the cyan and red areas to double-charm and signal components, respectively. The vertical line shows the 4σ requirement used in the analysis to reject the prompt background component.

distance (with respect to the PV) along the z-axis (with a 10σ significance) and one in the transverse plane. Another important requirement is that the $\bar{D}^0$ and the pions from τ^+ must not originate from the PV, so a cut on the Impact Paramenter (*IP*) with respect to the PV is applied. The $\bar{D}^0$ and the τ^+ must originate from the same PV in order to reconstruct particles that belong to the same decay chain. One cut on the χ^2 of the 3π vertex is applied in order to select a well reconstructed τ^+ vertex. Cuts on `ProbNNpi` for the three pion candidates are required in order to suppress misidentified kaons. Furthermore, a single candidate per

event is required in order to remove events where several track candidates may form a 3π vertex. The main background for our analysis are very common $B^0 \to D^* D_s^+$ decays, where the D_s^+ decays into 3 pions + anything else. The D_s^+ is a very abundant source of 3π final states through two types of decays :

- $D_s^+ \to \mathrm{IS}\pi^+$ or $\mathrm{IS}\rho^+$ where at least two of the three pions originate from the decay chain of an intermediate state IS: η, η', ϕ or ω
- $D_s^+ \to \mathrm{M}\ 3\pi$ where M is is again an intermediate state K^0, η, η', ϕ or ω

In both types of decays, five charged particles will be present frequently in the final state: in the former case, mostly though $\eta' \to \eta\pi^+\pi^-$ followed by $\eta \to \pi^+\pi^-\pi^0$ or $\pi^+\pi^-\gamma$, in the latter case via basically any IS decay to $\pi^+\pi^-$ X. This true 5-prong background is especially harmful since it produces 6 3π combinations when all tracks are seen, and 2 or 3 when 1 track is missed. It must therefore be rejected with an high efficiency. It is therefore very convenient to exploit the high multiplicity of combinations produced by this background to kill it by asking only one combination per event, which is an obvious feature of any exclusive event such as $B^0 \to D^* \tau\nu$, $B^0 \to D^*\ 3\pi$ or $B^0 \to D^* D_s^+$.

The efficiency of the detached vertex cut has been evaluated on the various MC samples, keeping separated, when possible, the simulation with 2011 conditions from the 2012 one. The distributions of the other variables used in the selection are plotted in Figs. 4.2, 4.3 for the various MC samples. Generally good agreement is observed. The efficiencies are reported in Tab. 4.2.

Variable	Cut	Targeted background
$p_{\mathrm{T}}(\pi)$, π from 3π	> 250 MeV/c	All
$[z(3\pi) - z(B^0)]/\sigma_{(z(3\pi)-z(B^0))}$	> 4	prompt
$[z(3\pi) - z(\mathrm{PV})]/\sigma_{(z(3\pi)-z(\mathrm{PV}))}$	> 10	charm
$r_{3\pi}$	$\in [0.2, 5.0]$ mm	spurious 3π
$\chi^2_{\mathrm{IP}}(\bar{D}^0)$	> 10	charm
$\chi^2_{\mathrm{IP}}(\pi)$, π from 3π	> 15	combinatorial
$\mathrm{PV}(\bar{D}^0)$	$= \mathrm{PV}(3\pi)$	charm/combinatorial
number of B^0 candidates	$= 1$	all
3π vertex χ^2	< 10	combinatorial
$\Delta m \equiv m(D^{*-}) - m(\bar{D}^0)$	$\in [143, 148]$ MeV/c^2	combinatorial

Table 4.1 List of the selection cuts. See text for further explanation.

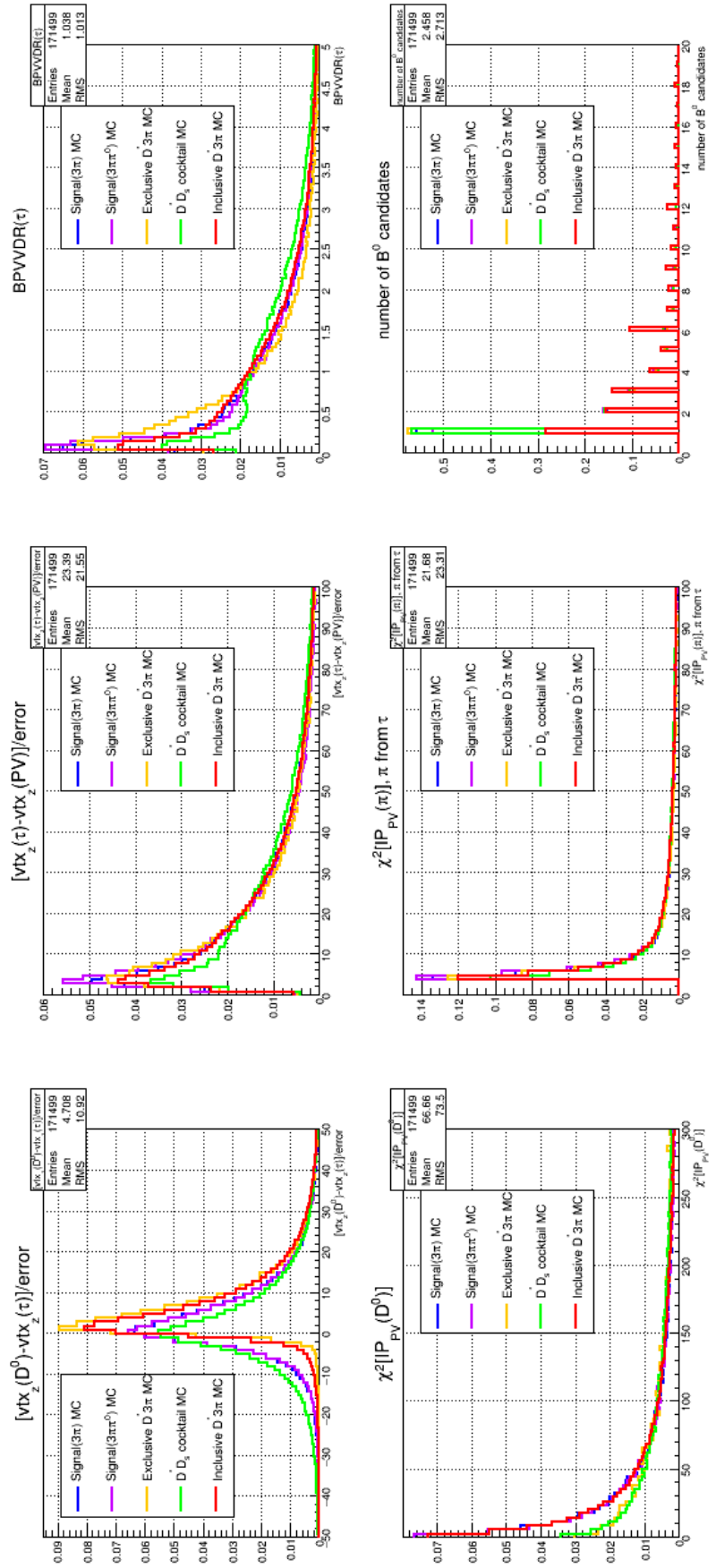

Fig. 4.2 Distributions of the variables used in the first selection (1).

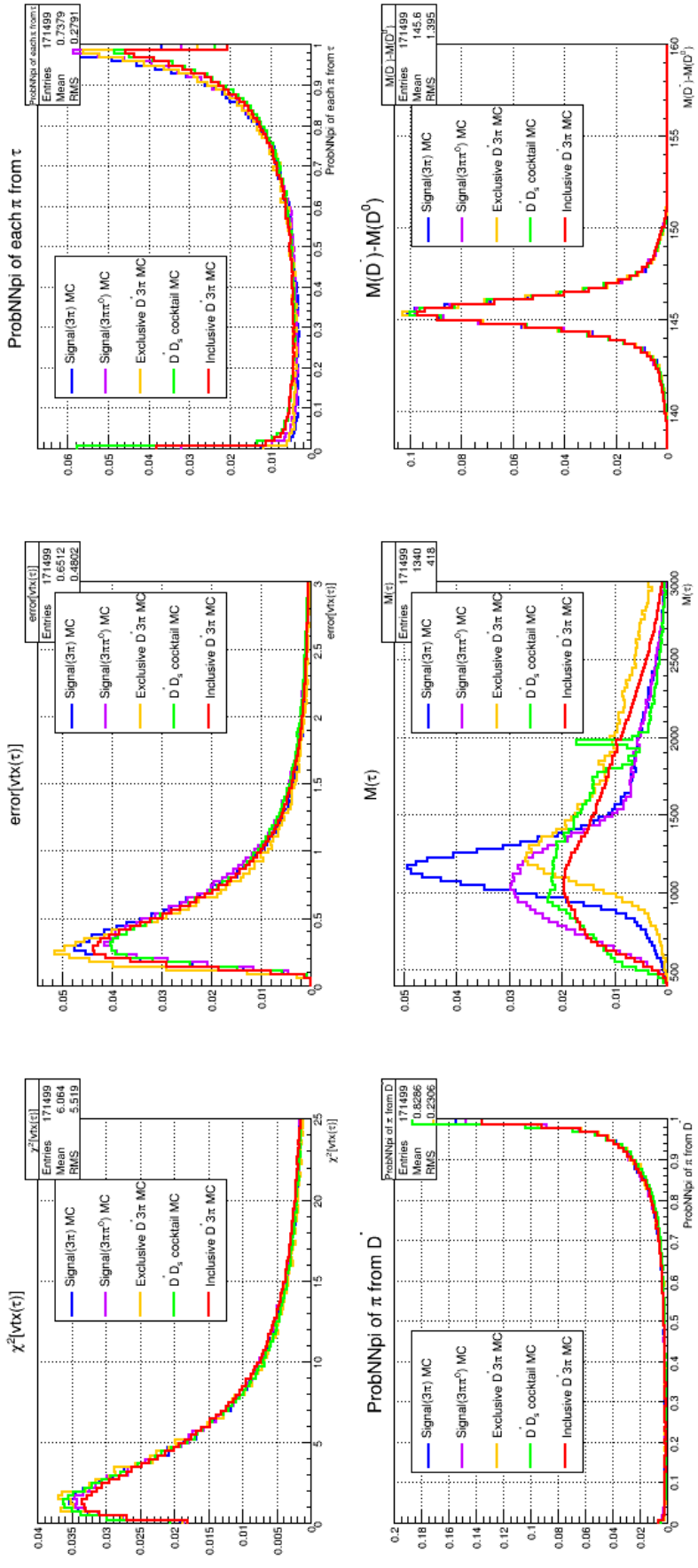

Fig. 4.3 Distributions of the variables used in the first selection (2).

4.1.1 Background with detached-vertex topology

The double-charm $B \to D^{*-}DX$ decays are the only other B decays with the same vertex topology as the signal. Fig. 4.1 show the dominance of the double-charm background over the signal after the detached-vertex requirement, on simulated events. Fig. 4.4 shows the 3π invariant mass data distribution after the vertex-detachement requirement, where peaking structures corresponding to the $D_s^+ \to 3\pi$ decay, a very important control channel for this analysis, and to the $D^+ \to 3\pi$ decay, are clearly visible.

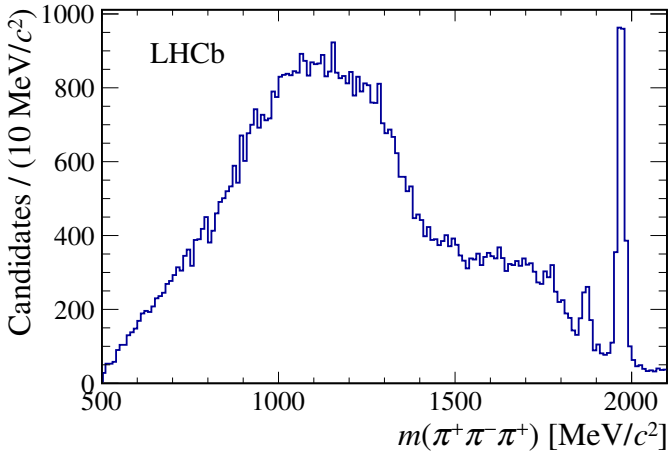

Fig. 4.4 Distribution of the 3π mass for candidates after the detached-vertex requirement. D^+ and D_s^+ mass peaks are clearly visible. The rest of the spectrum is due to D_s^+ and D^+ unreconstructed particles in the final states. For further details see Sec. 5.1.

4.1.2 Background from other sources

Requirements additional to the detached vertex one are needed to reject spurious background sources with vertex topologies similar to the signal. The various background sources are classified to distinguish candidates where the 3π system originates from a common vertex and those where one of the three pions originates from a different vertex.

- Background category where the 3π system stems from a common vertex:
  - the 3π system either comes from the decay of a τ lepton or a D^0, D^+, D_s^+ or Λ_c^+ hadron. In this case, the candidate has the correct signal-like vertex topology. Alternatively, it comes from a misreconstructed prompt background candidate containing a B^0, B^+, B_s^0 or Λ_b^0 hadron. The detailed composition of these different categories at the initial and the final stage of the analysis is described in Sec. 4.6.

- Background category where the 3π system don't originate from a common vertex:
  - In this case, the D^{*-} and the 3π systems are not daughters of the same b hadron. The 3π system originates from one of the following sources: the other b hadron present in the event (*B1B2* category); the decay of the charm hadrons produced at the PV (*charm* category); another PV; an interaction in the beam pipe or in the detector material. The 3π background not originating from the same vertex is dominated by candidates where two pions originate from the same vertex whilst the third may come directly from the PV, from a different vertex in the decay chain of the same b hadron, from the other b hadron produced at the PV, or from another PV. Due to the combinatorial origin of this background, there is no strong correlation between the pion pair and the third pion.

4.2 Selection of the normalization channel

The $B^0 \to D^{*-}3\pi$ normalization channel is selected by requiring the $\bar{D}^0$ vertex to be located at least 4σ downstream of the 3π vertex along the beam direction. All other selection criteria are identical to that of the signal case, except for the fact that no cut on the output of the MVA analysis (described in Sec. 4.5) is applied to the normalization channel. Figure 4.5 shows the D^{*-} 3π invariant mass spectrum after all these requirements. Moreover, the high purity of this sample of exclusive B^0 decays allows the validation of the selection efficiencies derived using simulation.

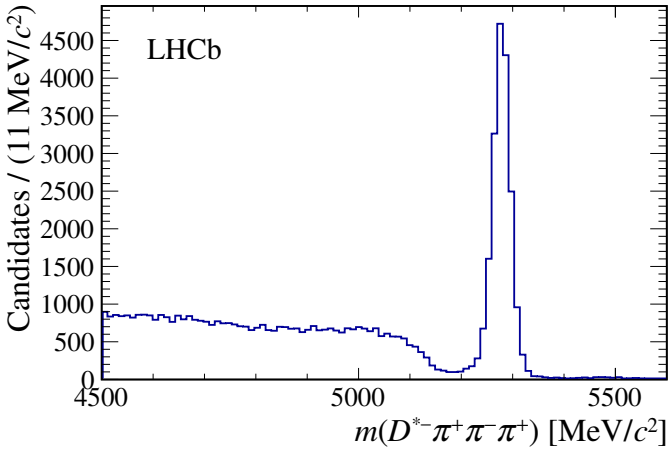

Fig. 4.5 Distribution of the $D^{*-}3\pi$ mass for candidates passing the selection criteria of the normalization channel.

4.3 Isolation requirements

The selection criteria described in the previous sections are efficient in removing backgrounds where the three pions originate from a B decay, where other particles are misidentified as pions, and combinatorial background. The remaining background is due to B decays where the three pions (or some of them) are produced from the decay of a particle with significant lifetime, such as D_s^+, D^0 or D^+ mesons. This background is suppressed by exploiting the fact that additional charged and/or neutral particles are produced in conjunction with the observed candidate. The isolation algorithms used to accomplish this task are described in the following.

4.3.1 Charged isolation

A charged-isolation algorithm ensures that no extra tracks are compatible with either the B^0 or 3π decay vertices. It is implemented by counting the number of charged tracks having p_{T} larger than 250 MeV/c, χ^2_{IP} with respect to the PV larger than 4, and $\chi^2_{\mathrm{IP}}(3\pi)$ and $\chi^2_{\mathrm{IP}}(B^0)$, with respect to the vertex of the 3π and B^0 candidates, respectively, smaller than 25. The candidate is rejected if any such track is found. As an example, the performance of the charged-isolation algorithm is determined on a simulated sample of double-charm decays with a D^0 meson in the final state. In cases where $B^0 \to D^{*-}D^0K^+(X)$, with $D^0 \to K^-3\pi(X)$, two charged kaons are present in the decay chain, one originating from the B^0 vertex and the other from the D^0 vertex. For these candidates, the rejection rate is 95%. The charged-isolation algorithm has a selection efficiency of 80% on a data sample of exclusive $B^0 \to D^{*-}3\pi$ decays. This sample has no additional charged tracks from the B^0 vertex, therefore it is similar at first order to the signal as far as charged-isolation properties are concerned. This value is in good agreement with the efficiency determined from simulation.

It is possible to reverse the isolation requirement to provide a sample of candidates from the inclusive D^0 decay chain, where a D^0 meson decays into $K^-3\pi$ and the charged kaon has been found as a nearby track. Figure 4.6 shows a clear D^0 signal when computing the $K^-3\pi$ invariant mass. This control sample is used to determine the properties of the $B \to D^{*-}D^0(X)$ background in the final fit that determines the signal yield.

4.3.2 Neutral isolation

Background candidates with additional neutral particles present in their decay chain are suppressed by using the energy deposited in the electromagnetic calorimeter in a cone $R = \sqrt{\Delta\eta + \Delta\phi} < 0.3$ units around the direction of the 3π system. For this rejection method

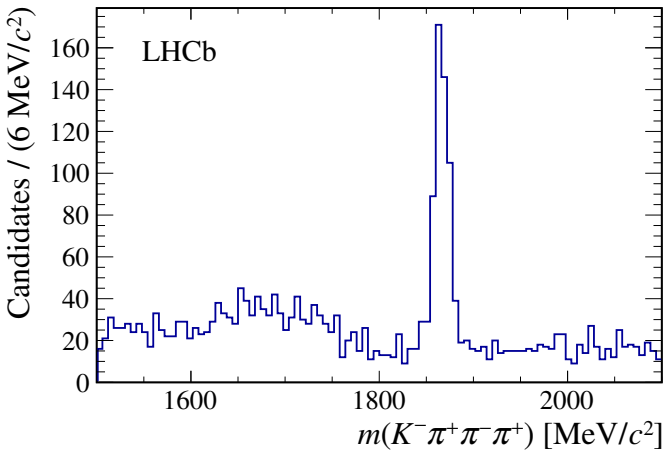

Fig. 4.6 Distribution of the $K^-3\pi$ mass for D^0 candidates where a charged kaon has been associated to the 3π vertex.

to be effective, the amount of collected energy in the region of interest must be small when no neutral particles are produced in the B^0 meson decay. Candidates where the B^0 meson decays to $D^{*-}3\pi$, with $D^{*-} \to \bar{D}^0\pi^-$, are used as a check. Figure 4.7 compares the distributions of the $D^{*-}3\pi$ invariant mass with and without the requirement of an energy deposition of at least 8 GeV in the electromagnetic calorimeter around the 3π direction. Since it is known that no neutral particles are emitted in this decay, the inefficiency of the algorithm can be estimated by the ratio of the yields of the two spectra within $\pm 30\,\text{MeV}/c^2$ around the B^0 mass, and is found small enough to allow the usage of this method. The energy deposited in the electromagnetic calorimeter around the 3π direction is one of the input variables to the MVA described below, used to suppress inclusive D_s^+ decays to 3π X, which contain photons and π^0 mesons in addition to the three pions. Photons are also produced when D_s^+ excited states decay to their ground state. The use of this variable has an impact on signal: the $\tau^+ \to 3\pi\pi^0\overline{\nu}_\tau$ decay has an efficiency roughly one half with respect to that of the 3π mode. This is reflected in the lower efficiency after the BDT cut for the $3\pi\pi^0$ decay mode with respect to 3π mode, as seen in Table 4.2.

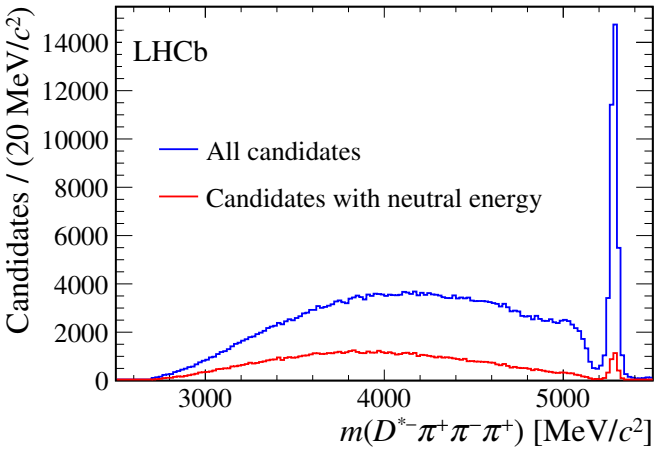

Fig. 4.7 Distribution of the $D^{*-}3\pi$ mass (blue) before and (red) after a requirement of finding at least 8 GeV of energy in the electromagnetic calorimeter around the 3π direction.

4.4 Reconstruction of the decay kinematics

Due to the precise knowledge of the $\bar{D}^0$, 3π and B^0 decay vertices, it is possible to reconstruct the decay chains of both signal and background processes, even in the presence of unreconstructed particles, such as two neutrinos in the case of the signal, or neutral particles originating at the 3π vertex in the case of double-charm background. The relevant reconstruction techniques are detailed in the following.

4.4.1 Reconstruction in the signal hypothesis

The missing information due to the two neutrinos emitted in the signal decay chain can be recovered with the measurements of the B^0 and τ line of flight (unit vectors joining the B^0 vertex to the PV and the 3π vertex to the B^0 vertex, respectively) together with the known B^0 and τ masses. This enables the reconstruction of the complete decay kinematics of both the B^0 and τ decays to be performed, up to two two-fold ambiguities. The τ momentum in the laboratory frame is obtained as

$$|\vec{p}_\tau| = \frac{(m_{3\pi}^2 + m_\tau^2)|\vec{p}_{3\pi}|\cos\theta_{\tau,3\pi} \pm E_{3\pi}\sqrt{(m_\tau^2 - m_{3\pi}^2)^2 - 4m_\tau^2|\vec{p}_{3\pi}|^2\sin^2\theta_{\tau,3\pi}}}{2(E_{3\pi}^2 - |\vec{p}_{3\pi}|^2\cos^2\theta_{\tau,3\pi})}, \tag{4.1}$$

where $\theta_{\tau,3\pi}$ is the angle between the 3π system three-momentum and the τ line of flight; $m_{3\pi}$, $|\vec{p}_{3\pi}|$ and $E_{3\pi}$ are the mass, three-momentum and energy of the 3π system, respectively; and m_τ is the known τ mass. Eq. 4.1 yields a single solution, in the limit where the opening angle between the 3π and the τ directions takes the maximum allowed value

$$\theta_{\tau,3\pi}^{\max} = \arcsin\left(\frac{m_\tau^2 - m_{3\pi}^2}{2m_\tau|\vec{p}_{3\pi}|}\right). \tag{4.2}$$

At this value, the argument of the square root in Eq. 4.1 vanishes, leading to only one solution, which is used as an estimate of the τ momentum. The same procedure is applied to estimate the B^0 momentum

$$|\vec{p}_{B^0}| = \frac{(m_Y^2 + m_{B^0}^2)|\vec{p}_Y|\cos\theta_{B^0,Y} \pm E_Y\sqrt{(m_{B^0}^2 - m_Y^2)^2 - 4m_{B^0}^2|\vec{p}_Y|^2\sin^2\theta_{B^0,Y}}}{2(E_Y^2 - |\vec{p}_Y|^2\cos^2\theta_{B^0,Y})}, \tag{4.3}$$

where Y represents the $D^*\tau$ system, by defining

$$\theta^{\max}_{B^0,Y} = \arcsin\left(\frac{m^2_{B^0} - m^2_Y}{2m_{B^0}|\vec{p}_Y|}\right). \tag{4.4}$$

Here, the three-momentum and mass of the $D^*\tau$ system are calculated using the previously estimated τ momentum

$$\vec{p}_Y = \vec{p}_{D^*} + \vec{p}_\tau, \quad E_Y = E_{D^*} + E_\tau, \tag{4.5}$$

where $\vec{p}_{D^*}$ and $\vec{p}_\tau$ are the three-momenta of the D^{*-} and the τ candidates, and E_{D^*} and E_τ their energies. Using this method, the rest-frame variables are determined with sufficient accuracy to retain their discriminating power against double-charm backgrounds, as discussed in Sec. 6.1. Figure 4.8 shows the difference between the reconstructed and the true $q^2 \equiv (p_{B^0} - p_{D^*})^2 = (p_\tau + p_{\nu_\tau})^2$. No significant bias is observed and an average resolution of $1.2\,\mathrm{GeV}^2/c^4$ is obtained. The relative q^2 resolution (18% full-width half-maximum) in terms of RMS, is comparable with the LHCb analysis using a lepton in the final state [11] ($\approx$15%–20% full width at half maximum).

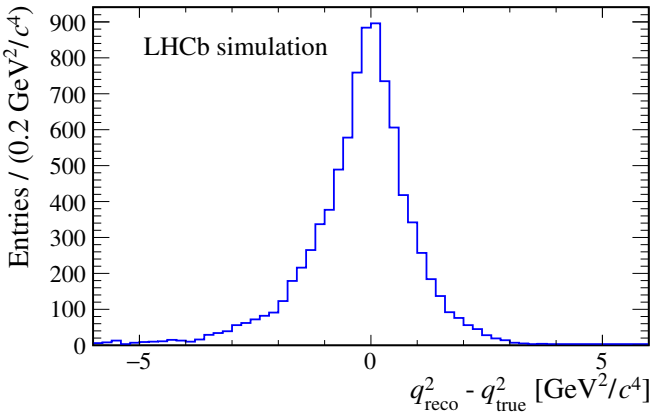

Fig. 4.8 Difference between the reconstructed and true q^2 variables, observed in the $B^0 \to D^{*-}\tau^+\nu_\tau$ simulated signal sample after partial reconstruction.

Using the computed momentum in Eqn. 4.1 it is possible to extract the decay time of the 3π system as follows:

$$\begin{aligned}\beta &= \frac{|p_\tau|}{E_\tau} \\ \gamma &= \frac{1}{\sqrt{1-\beta^2}} \\ L &= \sqrt{(\tau_x - B_x)^2 + (\tau_y - B_y)^2 + (\tau_z - B_z)^2} \\ t_\tau &= \frac{Lc}{\beta\gamma}\end{aligned} \tag{4.6}$$

where E_τ is the energy of the τ, $\tau_{x,y,z}$ and $B_{x,y,z}$ are the coordinates of the τ and B endvertices, c is the speed of light. The distribution and resolution of the computed decay time are shown in figure 4.9.

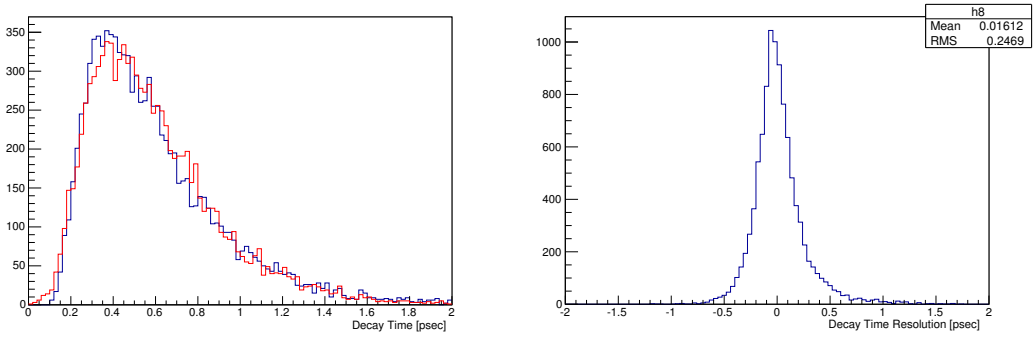

Fig. 4.9 Left: Reconstructed τ decay time (blue) as compared with the true value (red) for signal Monte Carlo. Right: Resolution on the τ decay time.

4.4.2 Reconstruction in the $B^0 \to D^* D^+_{(s)}$ hypothesis

In the $B^0 \to D^{*-} D_s^+$ decay the following equation can be written (momentum conservation, see Fig. 4.10):

$$|\vec{p}_B|\hat{u}_B = |\vec{p}_{D_s^+}|\hat{u}_{D_s^+} + \vec{p}_{D^*}, \tag{4.7}$$

where $\vec{p}_B$, $\vec{p}_{D_s^+}$ and $\vec{p}_{D^*}$ are the momenta of the mesons involved in the decay, and $\hat{u}_B$, $\hat{u}_{D_s^+}$ their unit vectors.

Starting from this relation and applying some vectorial algebra, it is possible to reconstruct the values of $|\vec{p}_B|$ and $|\vec{p}_{D_s^+}|$ in two different ways, that will be called "vectorial" and "scalar"

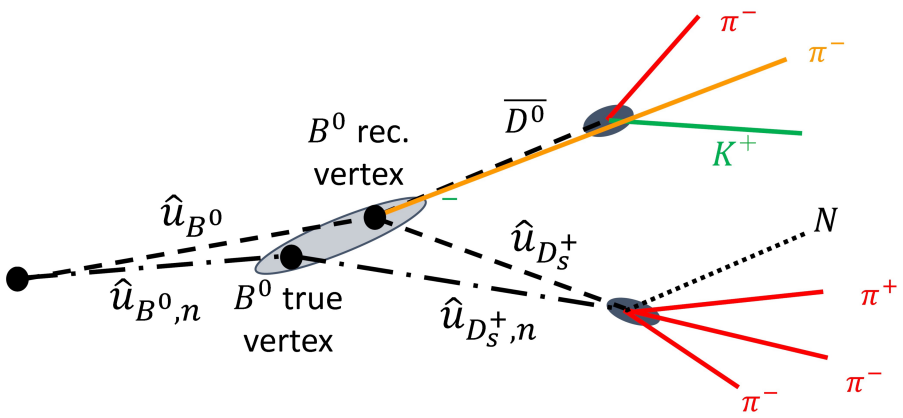

Fig. 4.10 Schematic representation of $B^0 \to D^{*-} D_s^+ (\to \pi^+\pi^-\pi^+ N)$ decay.

approaches. The magnitudes of the momenta obtained with these two approaches are equal to:

$$P_{B,v} = \frac{|\vec{p}_{D^*} \times \hat{u}_{D_s^+}|}{|\hat{u}_B \times \hat{u}_{D_s^+}|}, \tag{4.8a}$$

$$P_{B,s} = \frac{\vec{p}_{D^*} \cdot \hat{u}_B - (\vec{p}_{D^*} \cdot \hat{u}_{D_s^+})(\hat{u}_B \cdot \hat{u}_{D_s^+})}{1 - (\hat{u}_B \cdot \hat{u}_{D_s^+})^2}, \tag{4.8b}$$

for the B^0 momentum, and

$$P_{D_s,v} = \frac{|\vec{p}_{D^*} \times \hat{u}_B|}{|\hat{u}_{D_s^+} \times \hat{u}_B|}, \tag{4.9a}$$

$$P_{D_s,s} = \frac{(\vec{p}_{D^*} \cdot \hat{u}_B)(\hat{u}_B \cdot \hat{u}_{D_s^+}) - \vec{p}_{D^*} \cdot \hat{u}_{D_s^+}}{1 - (\hat{u}_B \cdot \hat{u}_{D_s^+})^2}, \tag{4.9b}$$

for the D_s^+ momentum.

Therefore the B^0 and D_s^+ momenta are reconstructed starting from three vectors:

- $\vec{p}_{D^*}$, which is fully reconstructed;
- $\hat{u}_B$, that is the direction of the line joining the B^0 vertex and the PV;
- $\hat{u}_{D_s^+}$, which at first approximation is given by the flight direction of the three-pion system, *i.e.* without considering possible neutral particles in D_s^+ decay.

This technique can be extended to take into account the presence of neutral particles in the D_s^+ decay chain, by applying a correction to the B^0 vertex position. In order to do that, a parametrization of this correction as function of $m(3\pi)$ has been obtained. Figure 4.11 shows

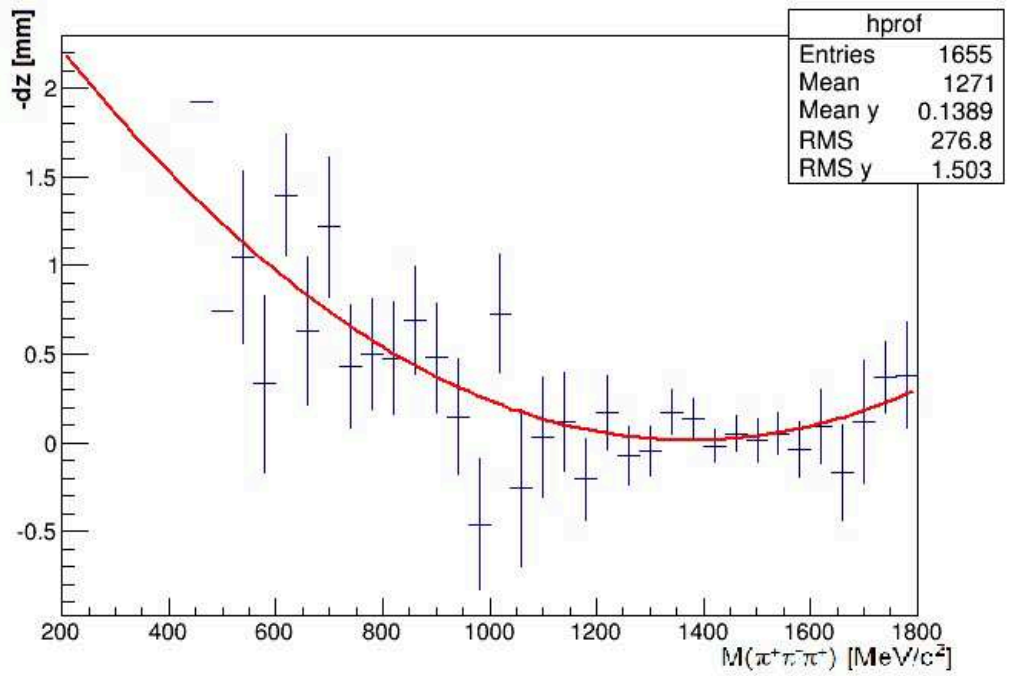

Fig. 4.11 The profile of the correction dz in function of the 3π mass. The chosen fitting function is a parabola.

the profile of $-dz = vtx_z(B^0) - vtx_z^{TRUE}(B^0)$, the correction on the B^0 vertex position along z, as function of the 3π mass.

A parabolic function has been chosen in order to fit this profile, and, after fitting, the dependence can be expressed in the following way:

$$-dz = 3.0346 - 0.00439605 \cdot m(3\pi) + 1.6 \cdot 10^{-6}[m(3\pi)]^2, \tag{4.10}$$

with dz in mm and $m(3\pi)$ in MeV/c^2.

The effect of the dz correction on the B^0 vertex (z component) resolution is shown in Figure 4.12. Even if the resolution does not improve very much, it is quite evident that the mean of the $(\text{true\_vtx}_z - \text{reco\_vtx}_z)/\text{true\_vtx}_z$ distribution is closer to 0 after the correction.

This correction allows to recompute the B^0 vertex position, in order to get new momentum values at a next-level of approximation. They are called $P_{B,vn}$, $P_{B,sn}$, $P_{D_s,vn}$ and $P_{D_s,sn}$, and they are calculated by using (4.8a), (4.9a), after plugging in the new directions $\hat{u}_{B,n}$ and $\hat{u}_{D_s^+,n}$. Another set of variables which can be reconstructed by using $P_{B,v(s,vn,sn)}$ and $\hat{u}_{B(B,n)}$ are the squared D_s^+ masses built in the various hypotheses, $m^2_{D_s,v(s,vn,sn)}$, which are calculated using the nominal B^0 and D^{*-} masses. This variables will be useful in defining a D_s^+ mass region for the training of the MVA. Figure 4.13 shows the $3\pi N$ mass distribution obtained on a

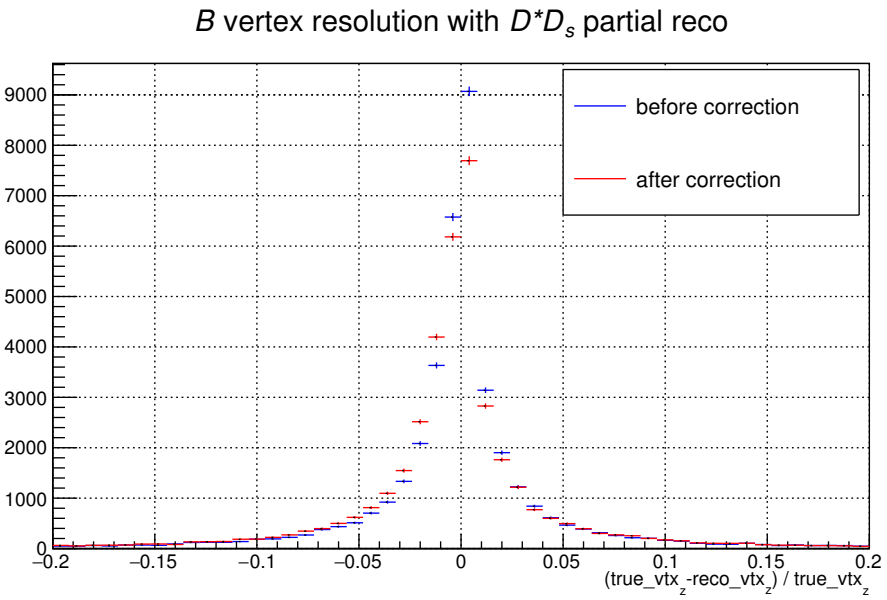

Fig. 4.12 Resolution on B^0 vertex (z component) on inclusive $D^*3\pi$ MC sample, before and after the correction dz.

sample enriched in $B \to D^{*-} D_s^+(X)$ decays, with $D_s^+ \to 3\pi N$, by means of the output of the MVA. A peaking structure originating from D_s^+ and D_s^{*+} decays is clearly visible. Due to the presence of two neutrinos at different vertices, signal decays are not handled well by partial reconstruction method, which therefore provides a useful discrimination between signal and background due to $B \to D^{*-} D_s^+(X)$ decays. However, this method cannot discriminate the signal from background due to $B \to D^{*-} D^0(X)$ and $B \to D^{*-} D^+(X)$ decays, where two kaons are missing at the B^0 and 3π vertices.

4.5 Multivariate analysis

Three features are used to reject the double-charm background: the different resonant structures of $\tau^+ \to 3\pi\overline{\nu}_\tau$ and $D_s^+ \to 3\pi X$ decays, the charged and neutral isolation (Sec. 4.3) and the different kinematic properties of signal and background candidates (Sec. 4.4.2).

To suppress double-charm background, a set of 18 variables is used as input to a MVA based upon a Boosted Decision Tree (BDT)[55, 56].
This set includes:

Variables related to the partial reconstruction (8 variables)

Reconstruction of the observed event can be performed into two possible scenarios:

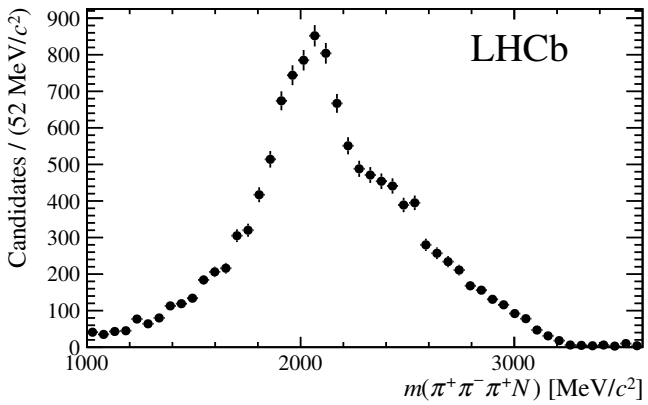

Fig. 4.13 Distribution of the reconstructed $3\pi N$ mass observed in a data sample enriched by $B \to D^{*-}D_s^+(X)$ candidates.

- Reconstruction as a background event: under this scenario, the event is reconstructed as $B^0 \to D^* D_{(s)}^{(*)}$ (see Section 4.4.2). Six variables stemming from this reconstruction are included in the BDT.
  1. $P_{B_{sn}}$: the B^0 momentum reconstructed using the scalar product method, using the corrected B^0 vertex;
  2. $ln|\frac{P_{Bv}}{B^0{}_P}|$: the ratio between the reconstructed B momentum and the visible one;
  3. $ln|\frac{P_{Bvn}}{B^0{}_P}|$: the ratio between the reconstructed B momentum and the visible one, using the corrected B^0 vertex;
  4. $ln|\frac{P_{Bsn}-P_{Bvn}}{P_{Bvn}}|$: the normalized difference between the different estimates of the B^0 momentum;
  5. m_{N2v}: the squared mass of the reconstructed neutral vector;
  6. $\sqrt{|m_{Ds2vn}|}$: the reconstructed mass of the $D_{(s)}^{(*,**)}$ system.
- Reconstruction as a signal event: the event is reconstructed as a signal event, (see Section 4.4.1). Two variables are incorporated:
  1. $P_B - P_\tau - P_{D^{*-}}$: the energy of the neutrino emitted at the B vertex;
  2. $ln(\chi^2_{B^0})$: the χ^2 of the reconstruction of the event in this hypothesis.

The neutral and charged isolation (5 variables)

Background events where the 3π system is coming from D_s^+ decays are often accompanied by a large neutral energy coming from the rest of the D_s^+ decay. This neutral energy is searched in cones around the 3π system. The neutral cone variables have

already been described in Section 4.3.2. Three variables related to neutral energy are included in the BDT:

1. $Mult(\tau)_{0.4nc}$: the multiplicity of neutral objects in a cone of 0.4 opening (defined in the $\Delta\phi$, $\Delta\eta$ reference frame) centered around the 3π vector;
2. $P_z(\tau)_{0.4nc}$: the sum of the neutral energy contained in the cone of 0.4 opening;
3. $P_z(\tau)_{0.3nc}$: the sum of the neutral energy in a cone of 0.3 opening.

Even if the tau and the B^0 vertices are required to be isolated from additional charged tracks, we include in the BDT two variables provided by the charged isolation algorithm, *i.e.* $Mult(\tau)_{0.2cc}$ and $P_z(\tau)_{0.2cc}$, which are the multiplicity of charged objects and the energy in a cone of 0.2 opening centered around the 3π vector.

The $\pi^+\pi^-$ dynamics (2 variables)

The Q-value available to the $\pi^+\pi^-$ pair in the $\eta \to \pi^+\pi^-\pi^0$ and $\eta' \to \eta\pi^+\pi^-$ decay chain is less than 400 MeV, so the $\pi^+\pi^-$ invariant mass in these decays is bound to be constrained between 278 MeV and 400 MeV. Therefore, many $\pi^+\pi^-$ from D_s^+ decays where η and η' abound will exhibit this distinctive low mass enhancement. On the other hand, the $\tau \to 3\pi\nu$ decay is a pure a_1 channel which itself decays exclusively to $\rho\pi$ [57]. The maximum value for the two possible $\pi^+\pi^-$ states will therefore exhibit a ρ peak for the signal and a peak at much lower mass for the background. The minimum and maximum values for the $\pi^+\pi^-$ masses have been included in the BDT.

Kinematics (3 variable)

The kinematics variables $\rho(B^0)$[1], $E(\tau)$ (the energy of the 3π system) and $m(B^0)$ (the mass of the six tracks system) have also been included. $m(B^0)$ is a powerful discriminant against backgrounds where the τ lepton originates from D_s^+ decays and from events where the 3 pions do not come from the same vertex.

The BDT is trained using simulated samples of signal and double-charm background decays. Figure 4.14 shows the normalized distributions of the four input variables having the largest discriminating power for signal and background namely: the minimum and maximum of the masses of oppositely charged pions, $\min[m(\pi^+\pi^-)]$ and $\max[m(\pi^+\pi^-)]$; the neutrino energy, approximated as the the difference of the moduli of the momentum of the B^0 and the sum of the moduli of the momenta of D^{*-} and τ reconstructed in the signal hypothesis, and the $D^{*-}3\pi$ mass. The BDT response for signal and background is illustrated in Fig. 4.15.

[1]The distance (cylindrical) from the end vertex of the B^0 and the related primary vertex.

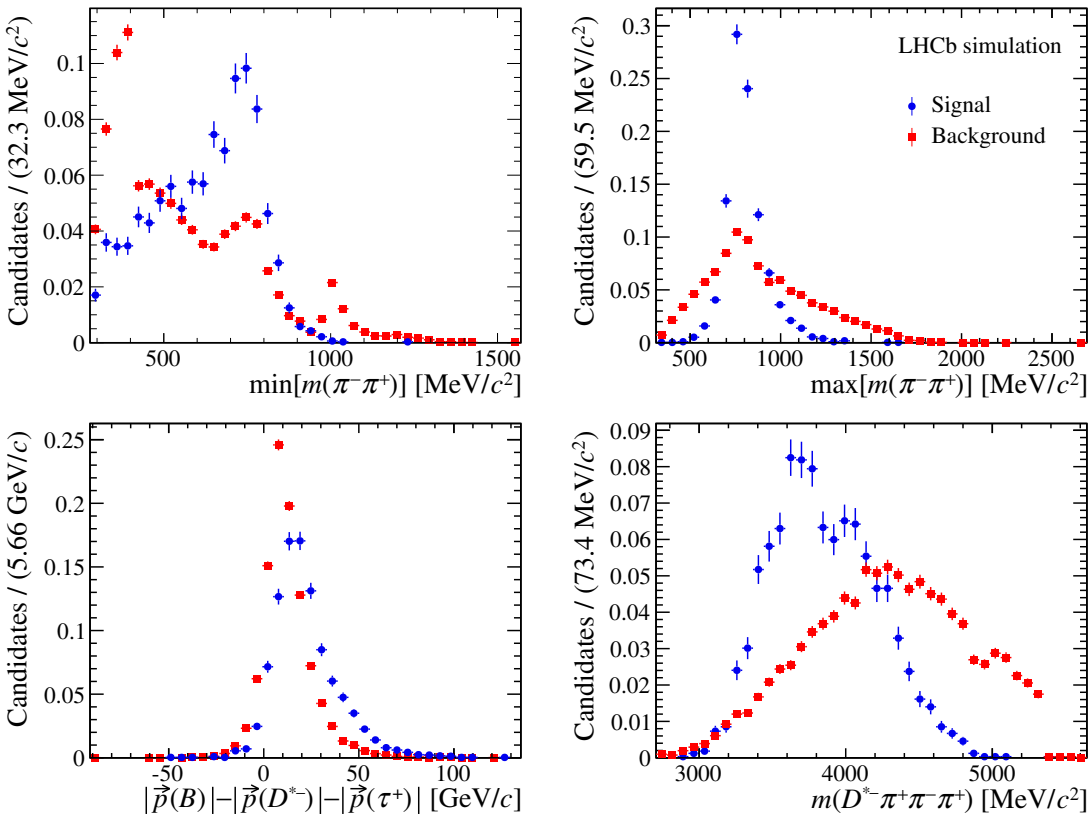

Fig. 4.14 Normalized distributions of (top left) min$[m(\pi^+\pi^-)]$, (top right) max$[m(\pi^+\pi^-)]$, (bottom left) approximated neutrino energy reconstructed in signal hypothesis, and (bottom right) the $D^{*-}3\pi$ mass in simulated samples.

The $B \to D^{*-}D_s^+(X)$, $B \to D^{*-}D^0(X)$ and $B \to D^{*-}D^+(X)$ control samples, described in Sec. 5, are used to validate the BDT. Figure 4.16 show the comparison of a subset of BDT input variables. There is a significant discrepancy between MC and control sample for the distributions. This can be explained by the fact that the background structure in data and MC are different, and no background subtraction is performed. Also, no MC reweightings are performed.

In Figure 4.17 the normalized distributions of the input BDT variables for the $D^{*-}D^0X$ control sample are shown. The agreement is pretty good for most of the variables. The discriminating power of this variable is small, so we do not expect big effects if it is not very well modelled in a subdominant background.

The same comparison is done for the $D^{*-}D^+X$ component is reported in Figure 4.17 The agreement is pretty good, similarly to what happens for the $D^{*-}D^0X$ component.

The signal yield is determined from candidates in the region where the BDT output is greater than -0.075. According to simulation, this value gives the best statistical power in

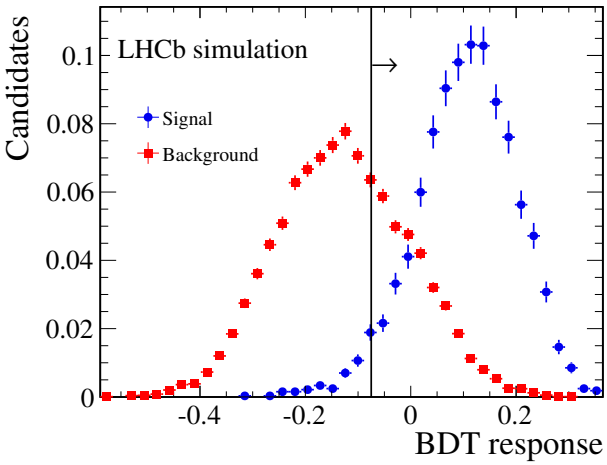

Fig. 4.15 Distribution of the BDT response on the signal and background simulated samples.

the determination of the signal yield. Candidates with the BDT output less than -0.075 are highly enriched in D_s^+ decays and contain very little signal, as shown in Fig. 4.15, and represent about half of the total data sample. They are used to validate the simulation of the various components in $D_s^+ \to 3\pi X$ decays used in the parameterization of the templates entering in the fit that determines the signal yield, as explained in Sec. 5.1. No BDT cut is applied in the selection for the normalization channel.

4.6 Composition of the selected samples and efficiencies

Figure 4.19 shows the composition of an inclusive sample of simulated events, generated by requiring that a D^{*-} meson and a 3π system are both part of the decay chain of a $b\bar{b}$ pair produced in a proton-proton collision before the detached-vertex requirement, at the level of the signal fit, and with a tighter cut corresponding to BDT output greater than 0.031. In the histograms, the first bin corresponds to the signal representing only 1% of the candidates at the initial stage, and the second to prompt candidates, where the 3π system originates from the b-hadron decay. The latter constitutes by far the largest initial background source. The following three bins correspond to cases where the 3π system originates from the decay of a D_s^+, D^0 or D^+ meson, respectively. The plot in the middle corresponds to the BDT output greater than -0.075 used in the analysis to form the sample in which the signal determination takes place. One can see the suppression of the prompt background due to the detached-vertex requirement, and the dominance of the D_s^+ background. The bottom plot shows for illustration the sample composition with a tighter BDT output cut. The D_s^+

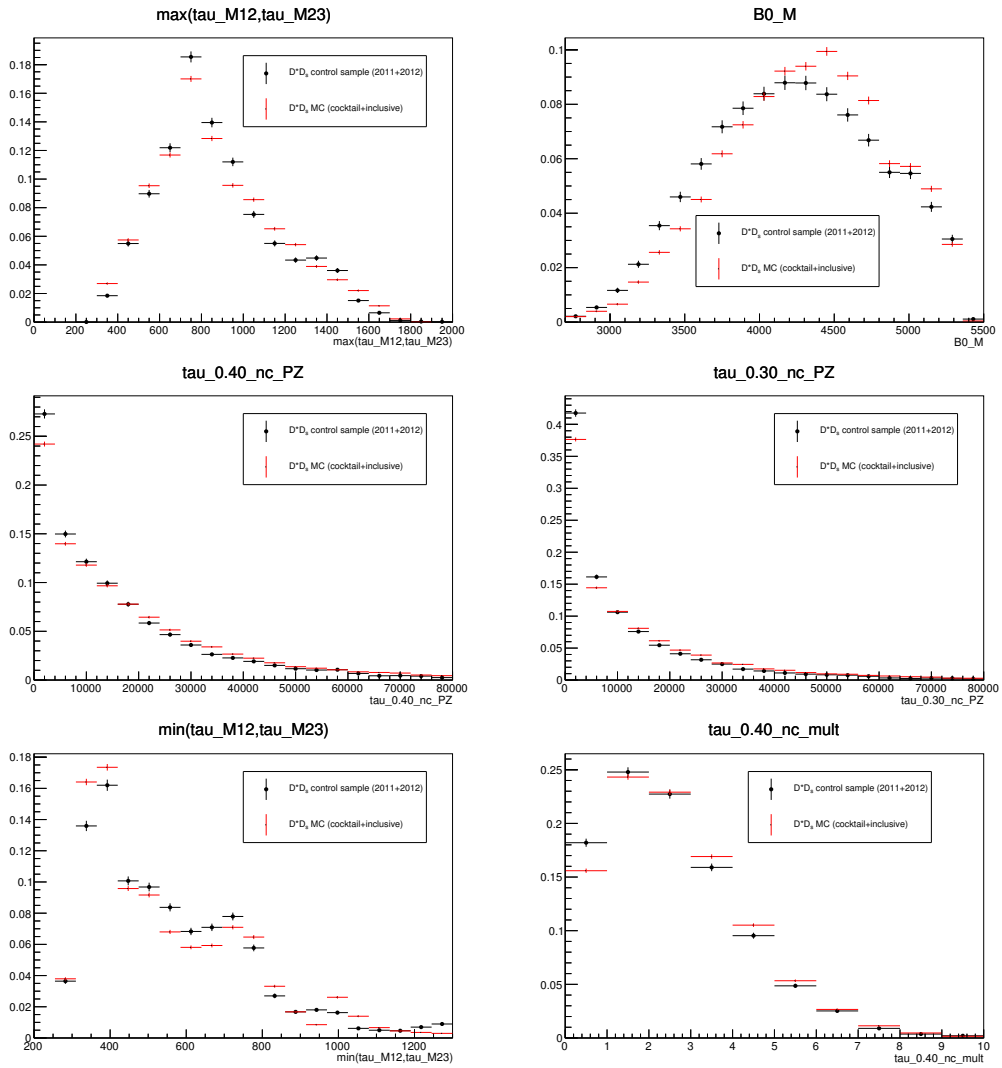

Fig. 4.16 Comparison of the BDT variables between $D^{*-}D_sX$ component of background MC and $D^{*-}D_sX$ control sample.

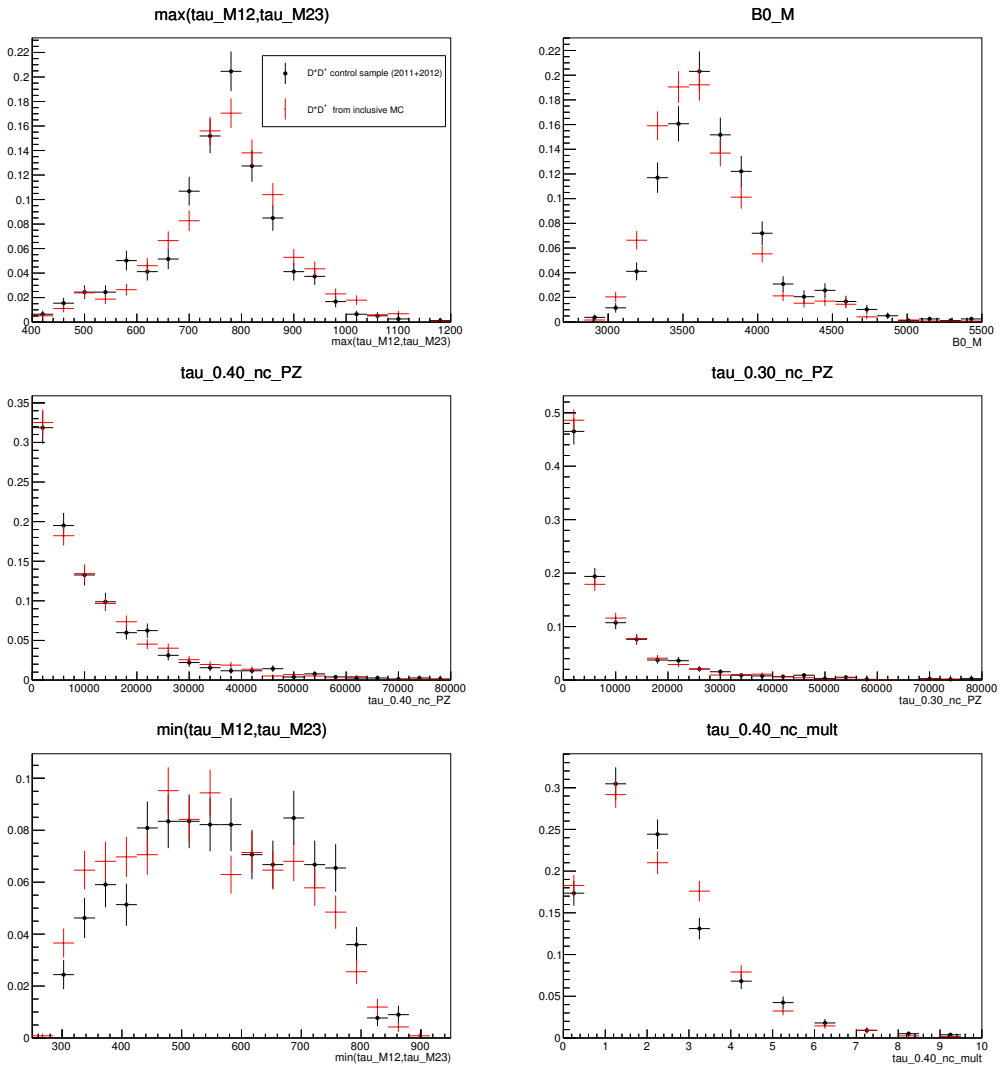

Fig. 4.17 Comparison of the BDT variables between $D^{*-}D^0X$ component of background MC and $D^{*-}D^0X$ control samples (1).

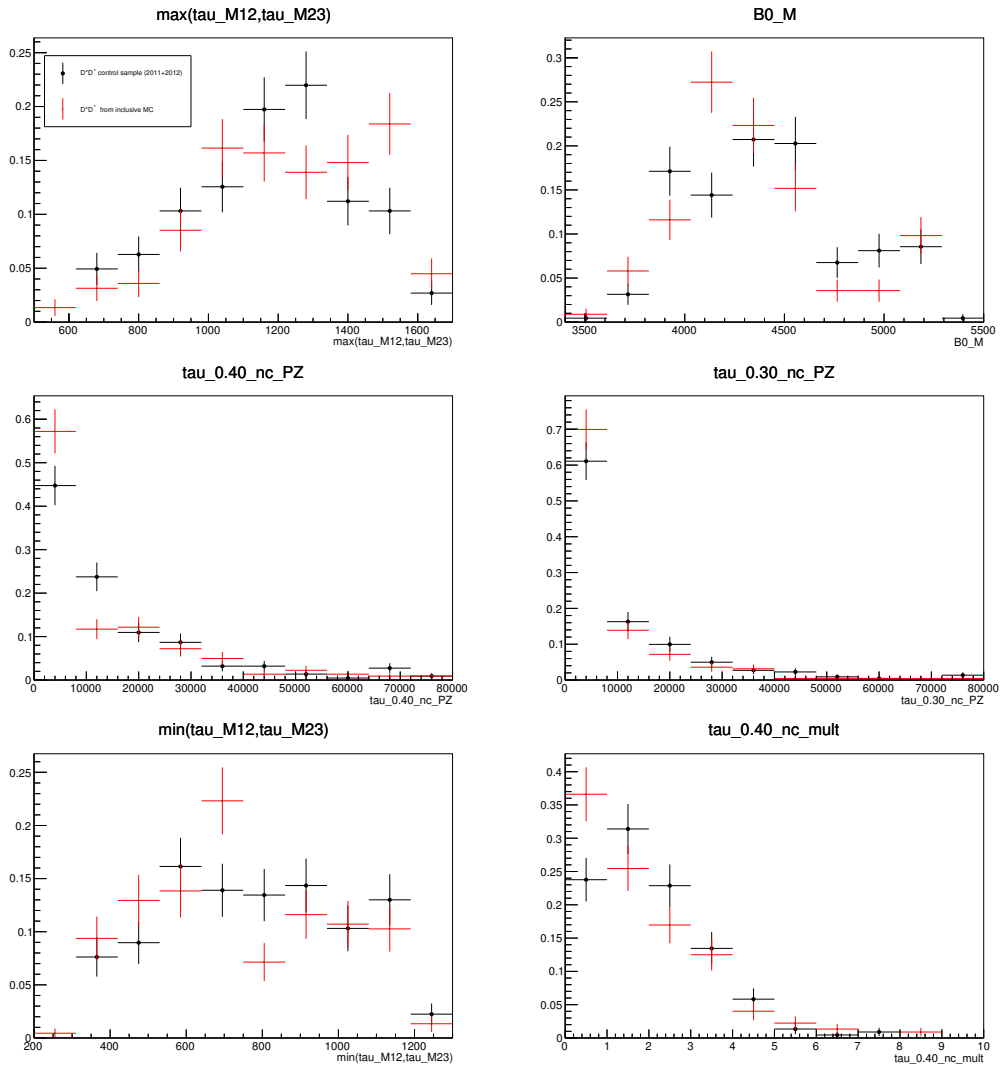

Fig. 4.18 Comparison of the BDT variables between $D^{*-}D^{+}X$ component of background MC and $D^{*-}D^{+}X$ control samples (1).

contribution is now suppressed as well. The signal fraction represents more than 30% at this stage. Figure 4.19 also allows contributions due to decays of other b hadrons to be compared with those due to B^0 meson decays.

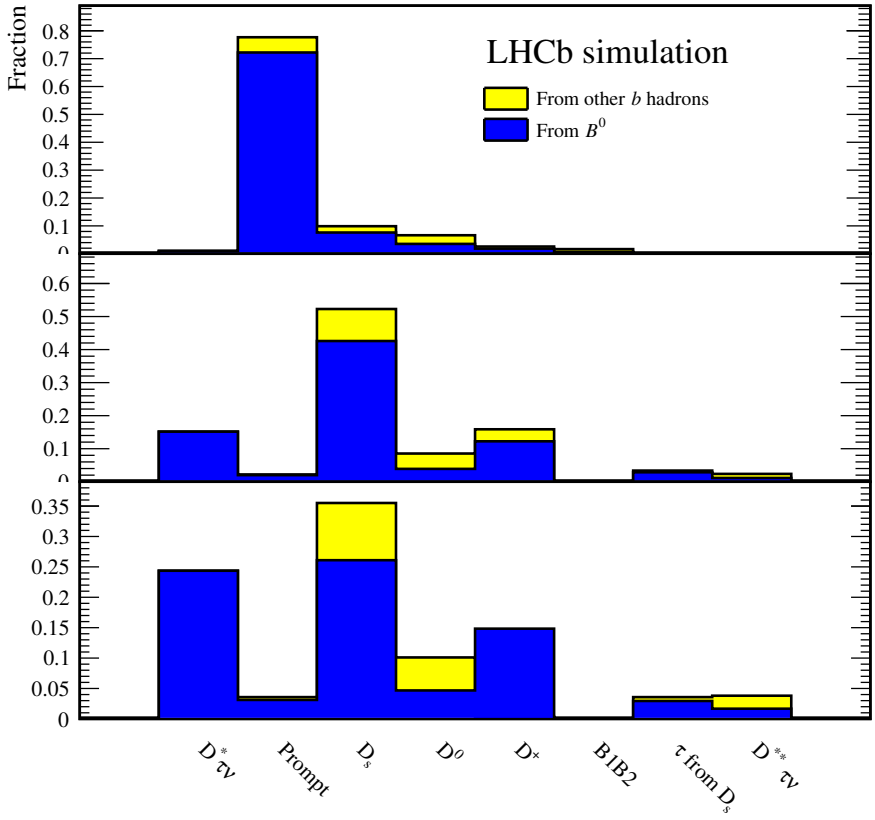

Fig. 4.19 Composition of an inclusive simulated sample where a D^{*-} and a 3π system have been produced in the decay chain of a $b\bar{b}$ pair from a pp collision. Each bin shows the fractional contribution of the different possible parents of the 3π system (blue from a B^0, yellow for other b hadrons): from signal; directly from the b hadron (prompt); from a charm parent D_s^+, D^0, or D^+ meson; 3π form a B and the D^0 from the other B (B1B2); from τ lepton following a D_s^+ decay; from a τ lepton following a $D^{**}\tau^+\nu_\tau$ decay (D^{**} denotes here any higher excitation of D mesons). (Top) After the initial selection and the removal of spurious 3π candidates. (Middle) For candidates entering the signal fit. (Bottom) For candidates populating the last 3 bins of the BDT distribution (cf. Fig. 6.1).

Table 4.2 presents the efficiency of the various selection steps, both for signal and normalization channels.

Requirement	Absolute efficiencies (%)			Relative efficiencies (%)		
	$D^{*-}3\pi$	$D^{*-}\tau^+\nu_\tau$		$D^{*-}3\pi$	$D^{*-}\tau^+\nu_\tau$	
		$3\pi\overline{\nu}_\tau$	$3\pi\pi^0\overline{\nu}_\tau$		$3\pi\overline{\nu}_\tau$	$3\pi\pi^0\overline{\nu}_\tau$
Geometrical acceptance	14.65	15.47	14.64			
After:						
initial selection	1.382	0.826	0.729			
spurious 3π removal	0.561	0.308	0.238	40.6	37.3	32.6
trigger requirements	0.484	0.200	0.143	86.3	65.1	59.9
vertex selection	0.270	0.0796	0.0539	55.8	39.8	37.8
charged isolation	0.219	0.0613	0.0412	81.2	77.0	76.3
BDT requirement	-	0.0541	0.0292	-	94.1	74.8
PID requirements	0.136	0.0392	0.0216	65.8	72.4	74.1

Table 4.2 Summary of the efficiencies (in %) measured at the various steps of the analysis for simulated samples of the $B^0 \to D^{*-}3\pi$ channel and the $B^0 \to D^{*-}\tau^+\nu_\tau$ signal channel for both τ decays to $3\pi\overline{\nu}_\tau$ and $3\pi\pi^0\overline{\nu}_\tau$ modes. No requirement on the BDT output is applied for $D^{*-}3\pi$ candidates. The relative efficiency designates the individual efficiency of each requirement.

Chapter 5

Study of double-charm candidates

The fit that determines the signal yield uses templates that are taken from simulation. It is therefore of paramount importance to verify the agreement between data and simulation for the remaining background processes. Control samples from data are used wherever possible for this purpose. The relative contributions of double-charm backgrounds and their q^2 distributions from simulation are validated, and corrected where appropriate, by using data control samples enriched in such processes. Inclusive decays of D^0, D^+ and D_s^+ mesons to 3π are also studied in this way.

5.1 The D_s^+ decay model

The branching fraction of D_s^+ meson decays with a 3π system in the final state, denoted as $D_s^+ \to 3\pi X$ is about 15 times larger than that of the exclusive $D_s^+ \to 3\pi$. This is due to the large contributions from decays involving intermediate states such as K_S^0, η, η', ϕ, and ω mesons, which are generically denoted with the symbol R in the following. The branching fractions of processes of the type $D_s^+ \to R\pi^+$ are well know, but large uncertainties exist for several decays, such $D_s^+ \to R(\to \pi^+\pi^- X)\pi^+\pi^0$ and $D_s^+ \to R3\pi$.

The τ lepton decays through the $a_1(1260)^+$ resonance, which leads to the $\rho^0\pi^+$ final state [58]. The dominant source of ρ^0 resonances in D_s^+ decays is due to $\eta' \to \rho^0\gamma$ decays. It is therefore crucial to control the η' contribution in D_s^+ decays very accurately. The shape of the η' contribution in the $\min[m(\pi^+\pi^-)]$ distribution, is clearly visible in Fig. 5.1. It exhibits a double peaking structure: at low mass, due to the endpoint of phase space for the charged pion pair in the $\eta \to \pi^+\pi^-\pi^0$ and $\eta' \to \eta\pi^+\pi^-$ decays and, at higher mass, a ρ^0 peak. The shape of this contribution is precisely known since the η' branching fractions are known to better than 2%. The precise measurement of the low-mass excess on data therefore enables the control of the η' contribution in the sensitive ρ region.

The $D_s^+ \to 3\pi X$ decay model is determined from a data sample enriched in $B \to D^{*-} D_s^+ (X)$ decays by requiring a value of the BDT output less than -0.075. The distributions of $\min[m(\pi^+\pi^-)]$ and $\max[m(\pi^+\pi^-)]$, of the mass of the same-charge pions, $m(\pi^+\pi^+)$, and of the mass of the 3π system, $m(3\pi)$, are simultaneously fit with a model obtained from simulation. The fit model is constructed from the following components:

- D_s^+ decays where at least one pion originates from the decay of an η meson; the $D_s^+ \to \eta\pi^+$ and $D_s^+ \to \eta\rho^+$ components are in this category.
- D_s^+ decays where, in analogy with the previous category, an η' meson is involved.
- D_s^+ decays where at least one pion originates from an intermediate resonance other than η or η'; these are then subdivided into $R\pi^+$ and $R\rho^+$ final states; these decays are dominated by $R = \omega, \phi$ resonances.
- Other D_s^+ decays, where none of the three pions originates from an intermediate state; these are then subdivided into $K^0 3\pi$, $\eta 3\pi$, $\eta' 3\pi$, $\omega 3\pi$, $\phi 3\pi$, $\tau^+(\to 3\pi(N)\overline{\nu}_\tau)\nu_\tau$, and 3π nonresonant final states, $X_{\rm nr}$. Regarding the tauonic $D_s^+ \to \tau^+\nu_\tau$ decay, the label N stands for any potential extra neutral particle.

Templates for each category and for the non-D_s^+ candidates are determined from $B \to D^{*-} D_s^+ (X)$ and $B \to D^{*-} 3\pi X$ simulation samples, respectively. Figure 5.1 shows the fit results for the four variables. The fit measures the η and η' inclusive fractions very precisely because, in the $\min[m(\pi^+\pi^-)]$ histogram, the low-mass peak is the sum of the η and η' contributions, while only the η' meson contributes to the ρ^0 region. The ratio between decays with a π^+ and a ρ^+ meson in the final state is not precisely determined because of the limited sensitivity of the fit variables to the presence of the extra π^0. The sensitivity only comes from the low-yield high-mass tail of the 3π mass distribution which exhibits different endpoints for these two types of decays. Finally, the kinematical endpoints of the 3π mass for each $R3\pi$ final state enable the fit to determine their individual contributions, which are presently either poorly measured or not measured at all. The $D_s^+ \to \phi 3\pi$ and $D_s^+ \to \tau^+(\to 3\pi(N)\overline{\nu}_\tau)\nu_\tau$ branching fractions, known with a 10% precision, are fixed to their measured values [20].

The fit is in good agreement with the data, especially in the critical $\min[m(\pi^+\pi^-)]$ distribution. The fit parameters and their ratios, with values from simulation, are reported in Table 5.1. These are used to correct the corresponding contributions from simulation. In the final fit performed in the high BDT output region, the shape of each contribution is scaled according to the ratio of candidates in the two BDT regions, which is taken from simulation.

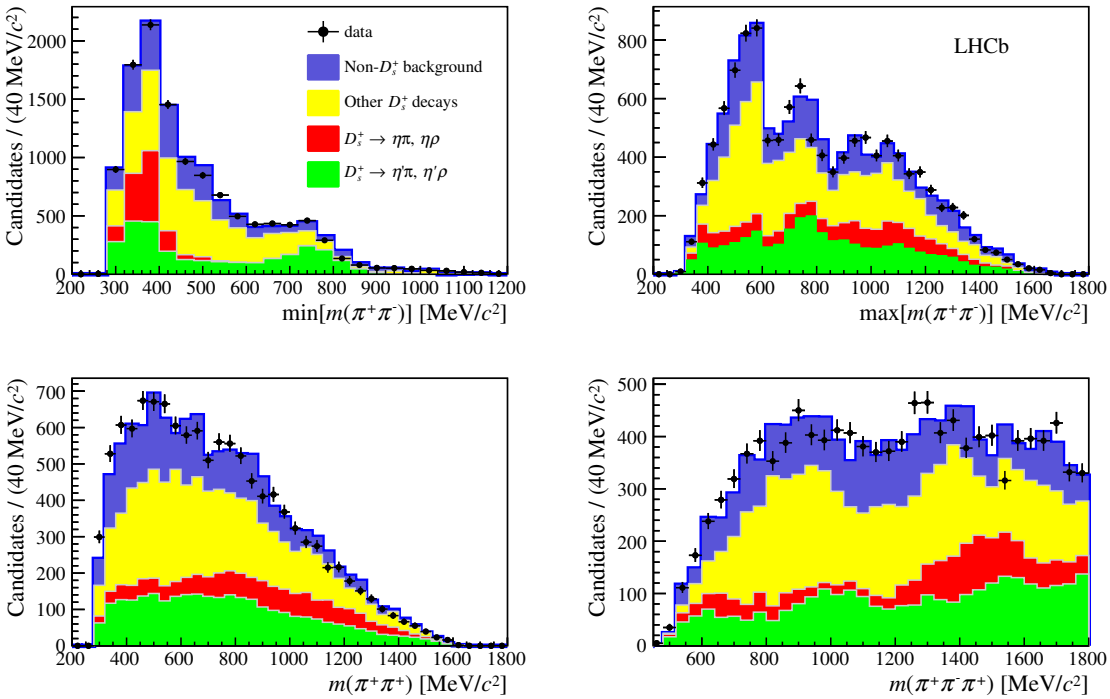

Fig. 5.1 Distributions of (top left) min$[m(\pi^+\pi^-)]$, (top right) max$[m(\pi^+\pi^-)]$, (bottom left) $m(\pi^+\pi^+)$, (bottom right) $m(\pi^+\pi^-\pi^+)$ for a sample enriched in $B \to D^{*-} D_s^+(X)$ decays, obtained by requiring the BDT output below a certain threshold. The different fit components correspond to D_s^+ decays with (red) η or (green) η' in the final state, (yellow) all the other considered D_s^+ decays, and (blue) backgrounds originating from decays not involving the D_s^+ meson.

The fit determines that $(47.3 \pm 2.5)\%$ of the D_s^+ decays in this sample contain η and η' mesons with an additional charged pion, $(20.6 \pm 4.0)\%$ contain ϕ and ω mesons with an additional charged pion and $(32.1 \pm 4.0)\%$ are due to $R3\pi$ modes.

This last contribution is dominated by the $\eta 3\pi$ and $\eta' 3\pi$ modes.

5.2 The $B^0 \to D^{*-} D_s^+(X)$ control sample

Candidates where the D_s^+ meson decays exclusively to the $\pi^+\pi^-\pi^+$ final state give a pure sample of $B \to D^{*-} D_s^+(X)$ decays. This sample includes three types of processes:[1]

[1] In this Section, D^{**} and D_s^{**} are used to refer to any higher-mass excitations of D^{*-} or D_s^+ mesons decaying D^{*-} and D_s^+ ground states.

D_s^+ decay	Relative contribution	Correction to simulation
$\eta\pi^+(X)$	0.156 ± 0.010	
$\eta\rho^+$	0.109 ± 0.016	0.88 ± 0.13
$\eta\pi^+$	0.047 ± 0.014	0.75 ± 0.23
$\eta'\pi^+(X)$	0.317 ± 0.015	
$\eta'\rho^+$	0.179 ± 0.016	0.710 ± 0.063
$\eta'\pi^+$	0.138 ± 0.015	0.808 ± 0.088
$\phi\pi^+(X)$, $\omega\pi^+(X)$	0.206 ± 0.02	
$\phi\rho^+$, $\omega\rho^+$	0.043 ± 0.022	0.28 ± 0.14
$\phi\pi^+$, $\omega\pi^+$	0.163 ± 0.021	1.588 ± 0.208
$\eta 3\pi$	0.104 ± 0.021	1.81 ± 0.36
$\eta' 3\pi$	0.0835 ± 0.0102	5.39 ± 0.66
$\omega 3\pi$	0.0415 ± 0.0122	5.19 ± 1.53
$K^0 3\pi$	0.0204 ± 0.0139	1.0 ± 0.7
$\phi 3\pi$	0.0141	0.97
$\tau^+(\to 3\pi(N)\overline{\nu}_\tau)\nu_\tau$	0.0135	0.97
$X_{\rm nr}3\pi$	0.038 ± 0.005	6.69 ± 0.94

Table 5.1 Results of the fit to the D_s^+ decay model. The relative contribution of each decay and the correction to be applied to the simulation are reported in the second and third columns, respectively.

- $B^0 \to D^{*-} D_s^{(*,**)+}$ decays, where a neutral particle is emitted in the decay of the excited states of the D_s^+ meson. The corresponding q^2 distribution peaks at the squared mass, $(p_{B^0} - p_{D^*})^2$, of the given states.

- $B_s^0 \to D^{*-} D_s^+ X$ decays, where at least one additional particle is missing. This category contains feeddown from excited states, both for D^{*-} or D_s^+ mesons. The q^2 distribution is shifted to higher values.

- $B^{0,-} \to D^{*-} D_s^+ X^{0,-}$ decays, where at least one additional particle originates from either the $B^{0,-}$ decay, or the de-excitation of charm-meson resonances of higher mass, that results in a D^{*-} meson in the final state. These additional missing particles shift the q^2 distribution to even higher values.

The $B \to D^{*-} D_s^+(X)$ control sample is used to evaluate the agreement between data and simulation, by performing a fit to the distribution of the mass of the $D^{*-}3\pi$ system, $m(D^{*-}3\pi)$. The fitting probability density function $\mathscr{P}$ is parameterized as

$$\mathscr{P} = f_{\rm c.b.}\, \mathscr{P}_{\rm c.b.} + \frac{(1 - f_{\rm c.b.})}{\sum_i f_i} \sum_j f_j \mathscr{P}_j \tag{5.1}$$

Parameter	Simulation	Fit	Ratio
$f_{\text{c.b.}}$	—	0.014	—
$f_{D_s^+}$	0.54	0.594 ± 0.041	1.10 ± 0.08
$f_{D_{s0}^{*+}}$	0.08	$0.000^{+0.040}_{-0.000}$	$0.00^{+0.50}_{-0.00}$
$f_{D_{s1}^+}$	0.39	0.365 ± 0.053	0.94 ± 0.14
$f_{D_s^+X}$	0.22	0.416 ± 0.069	1.89 ± 0.31
$f_{(D_s^+X)_s}$	0.23	0.093 ± 0.027	0.40 ± 0.12

Table 5.2 Relative fractions of the various components obtained from the fit to the $B \to D^{*-}D_s^+(X)$ control sample. The values used in the simulation and the ratio of the two are also shown.

where i or $j = \{D_s^+;\ D_s^{*+};\ D_{s0}^{*+};\ D_{s1}^+;\ D_s^+X;\ D_s^+X,\ s\}$. The fraction of combinatorial background, $f_{\text{c.b.}}$, is fixed in the fit. Its shape is taken from a sample where the D^{*-} meson and the 3π system have the same charge. Each component i is described by the probability density function $\mathscr{P}_i$, whose shapes are taken from simulation. The parameters f_i are the relative yields of $B^0 \to D^{*-}D_s^+$, $B^0 \to D^{*-}D_{s0}^*(2317)^+$, $B^0 \to D^{*-}D_{s1}(2460)^+$, $B^{0,+} \to D^{*-}D_s^+X$ and $B_s^0 \to D^{*-}D_s^+X$ decays with respect to the number of $B^0 \to D^{*-}D_s^{*+}$ candidates. They are floating in the fit, and $f_{D_s^{*+}} = 1$ by definition.

The 1D fit result on $m(D^{*-}3\pi)$ along with the projections of the signal fit variables, is shown in Fig. 5.2 and reported in Table 5.2, where a comparison with the corresponding values in the simulation is also given, along with their ratios. The measured ratios, including the uncertainties and correlations, are used to constrain these contributions in the final fit.

5.3 Other control samples

The main background component in the analysis is due to events containing a charm particle with a non-negligible lifetime. This is the case of decays involving D_s^+, D^0 and D^+ mesons.

The $B \to D^*D_s^+$ decay background composition has been discussed in Sec. 5.1. In this section, control samples of $B \to D^{*-}D^0(X)$ and $B \to D^{*-}D^+(X)$ decay modes are studied into final states corresponding to $D^{0,+} \to K^{-,0}3\pi(\pi^0)$ modes.

5.3.1 $B \to D^{*-}D^0(X)$ control samples

The agreement between data and simulation is validated in the D^0 case by using a control sample where the isolation algorithm identifies a kaon with charge opposite to the total charge of the 3π system, and compatible with originating from the 3π vertex. The mass of the $K^-3\pi$ system must be compatible with the known D^0 mass. This method provides a pure sample of $B \to D^{*-}D^0X$ decays. The $m(D^*K^-3\pi)$, q^2, 3π decay time and BDT distributions

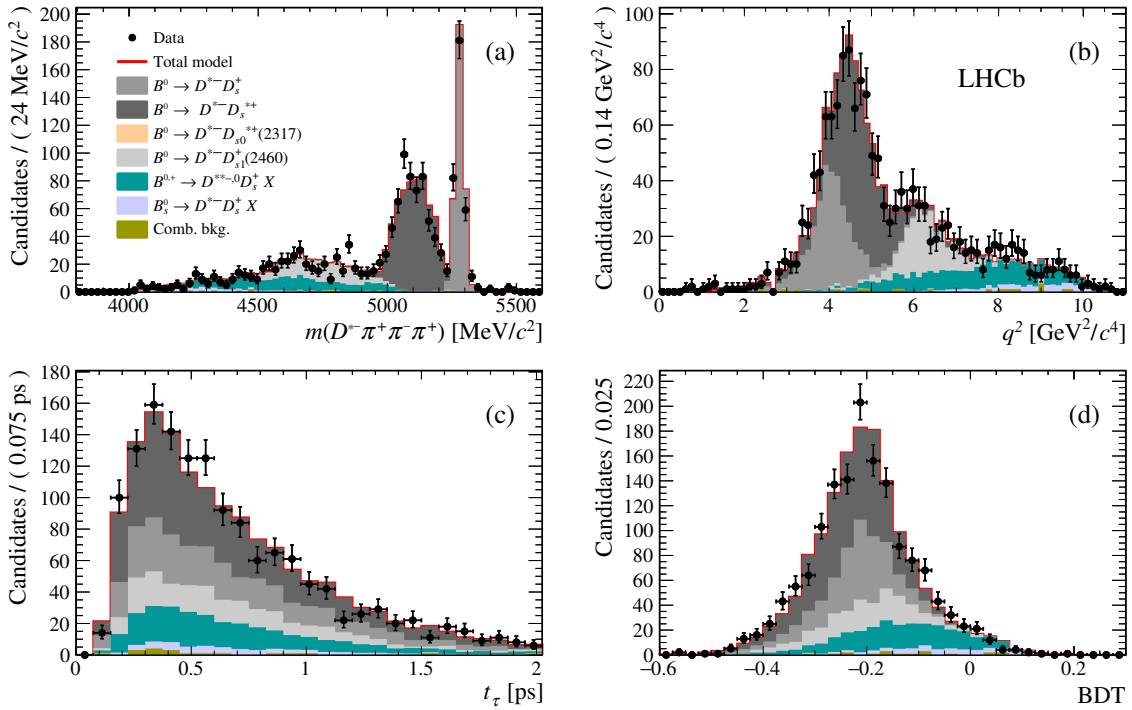

Fig. 5.2 Results from the fit to data for candidates containing a $D^{*-}D_s^+$ pair, where $D_s^+ \to 3\pi$. The fit components are described in the legend. The figures correspond to the fit projection on (a) $m(D^{*-}3\pi)$, (b) q^2, (c) 3π decay time t_τ and (d) BDT output distributions.

for such events are shown in Fig. 5.3 for real and simulated data. A clear systematic trend in the $m(D^*K3\pi)$ and q^2 distributions is present. This discrepancy indicates a bad description of the $B \to D^{*-}D^0X$ dynamics by the Monte Carlo.

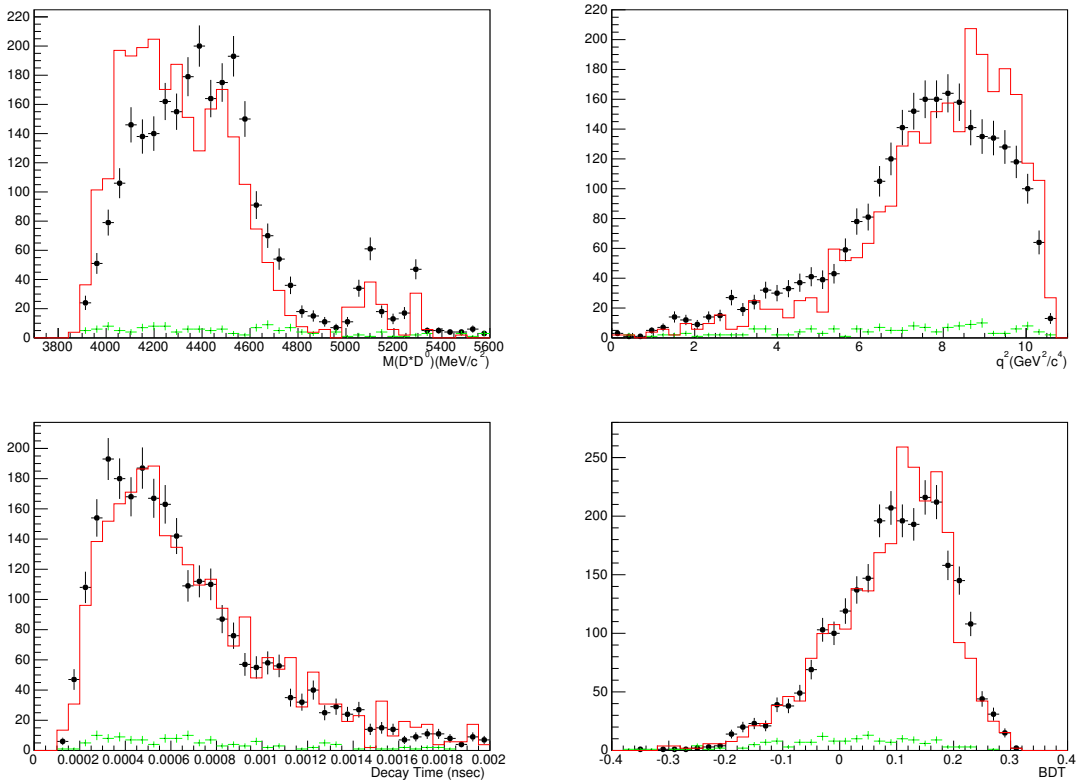

Fig. 5.3 Comparison between data (black points) and the $D^{*-}3\pi X$ inclusive Monte Carlo (red) for the $M(D^*K3\pi)$ (top left), q^2 (top right), 3π decay time (bottom left) and BDT (bottom right) distributions for the $B \to D^{*-}D^0X$ control sample. The combinatorial background, described by the wrong-sign events from the corresponding stripping line, is shown in green. The discrepancy observed in the q^2 distribution is corrected by applying a linear function correction to the D^0 component of the Monte Carlo.

To correct for this discrepancy, the ratio data/MC of the q^2 distribution is determined for events with $m(D^{*-}K^-3\pi) < 4.9GeV/c^2$, shown in Fig. 5.4. A first order polynomial is used to fit such ratio and the resulting correction is applied to the D^0 component of the $D^{*-}3\pi X$ inclusive Monte Carlo, which is used to create the template used in the fit to extract the $D^{*-}\tau^+\nu_\tau$ signal. The difference in the results with and without the correction is treated as a source of systematic uncertainty. A comparison of the four distributions is done after the correction. This is shown in Fig. 5.5, where a better agreement between data and MC is seen.

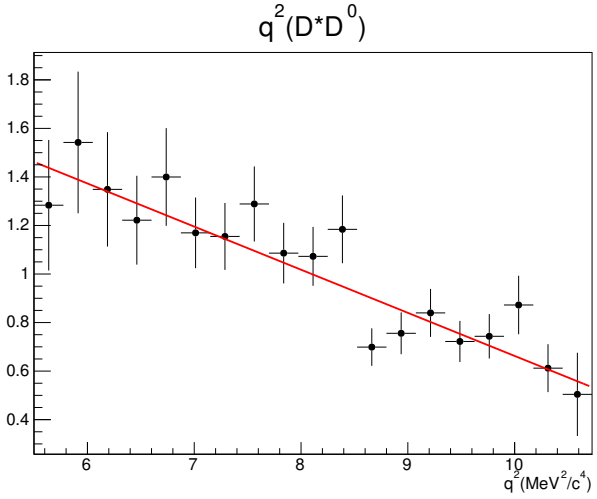

Fig. 5.4 Ratio data/MC on the q^2 distribution for events from the $B \to D^{*-}D^0X$ control sample. The fit to a linear function is shown in red, and it is applied as a correction to the D^0 component of the Monte Carlo.

5.3.2 $B \to D^{*-}D^+(X)$ control samples

A pure sample of $B \to D^{*-}D^+(X)$ decays is obtained by inverting the PID requirement on the negative pion of the 3π system, assigning to this particle the kaon mass and selecting 3π candidates with mass compatible with the known D^+ mass. As in the $B \to D^{*-}D^0(X)$ control sample, disagreement betwen data and simulation is found. The $m(D^{*-}K^-\pi^+\pi^+)$, q^2, 3π decay time and BDT distribution are shown in Fig. 5.6.

The limited size of this sample does not allow the determination of a specific correction. The same correction found in the $B \to D^{*-}D^0(X)$ case is therefore applied, since the dominant decay $B \to D^{*-}DK$ is identical for both cases. The distributions after applying the correction are shown in Fig. 5.7.

The difference between the distribution with and without the correction is accounted for in the study of the systematic uncertainties.

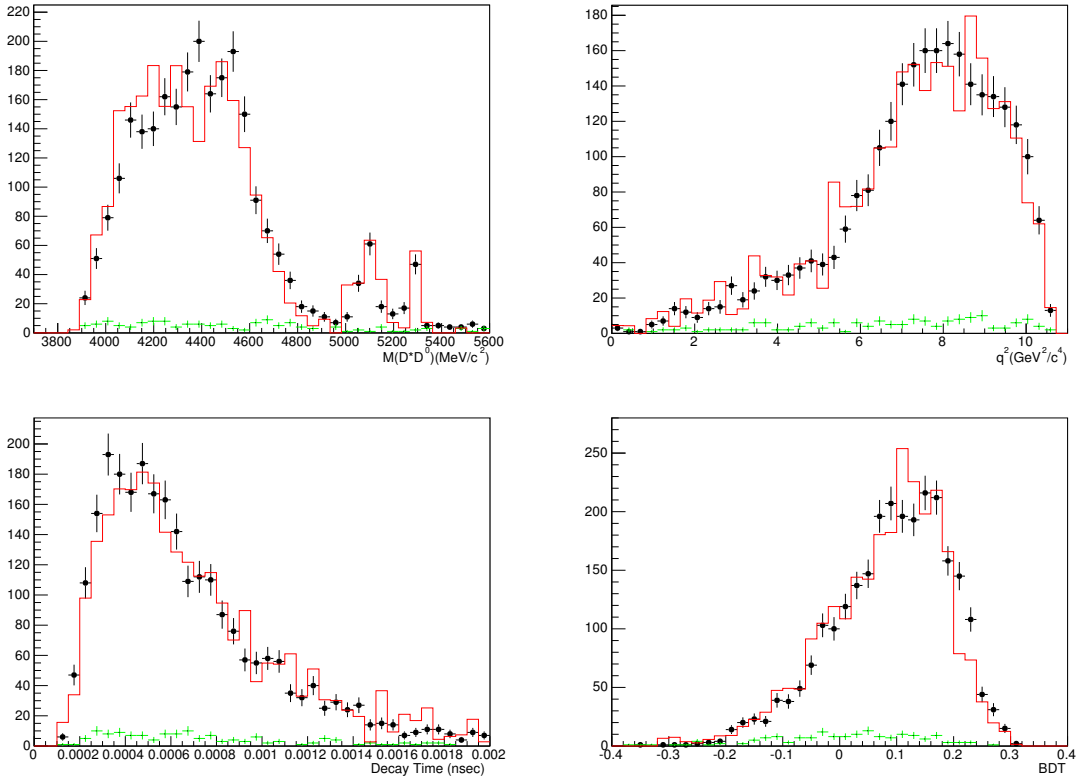

Fig. 5.5 Comparison between data (black points) and the $D^{*-}3\pi X$ inclusive Monte Carlo (red) for the $M(D^*K3\pi)$ (top left), q^2 (top right), 3π decay time (bottom left) and BDT (bottom right) distributions for the $B \to D^{*-}D^0X$ control sample after applying the correction on the q^2 distribution. The combinatorial background, described by the wrong-sign events from the corresponding stripping line, is shown in green.

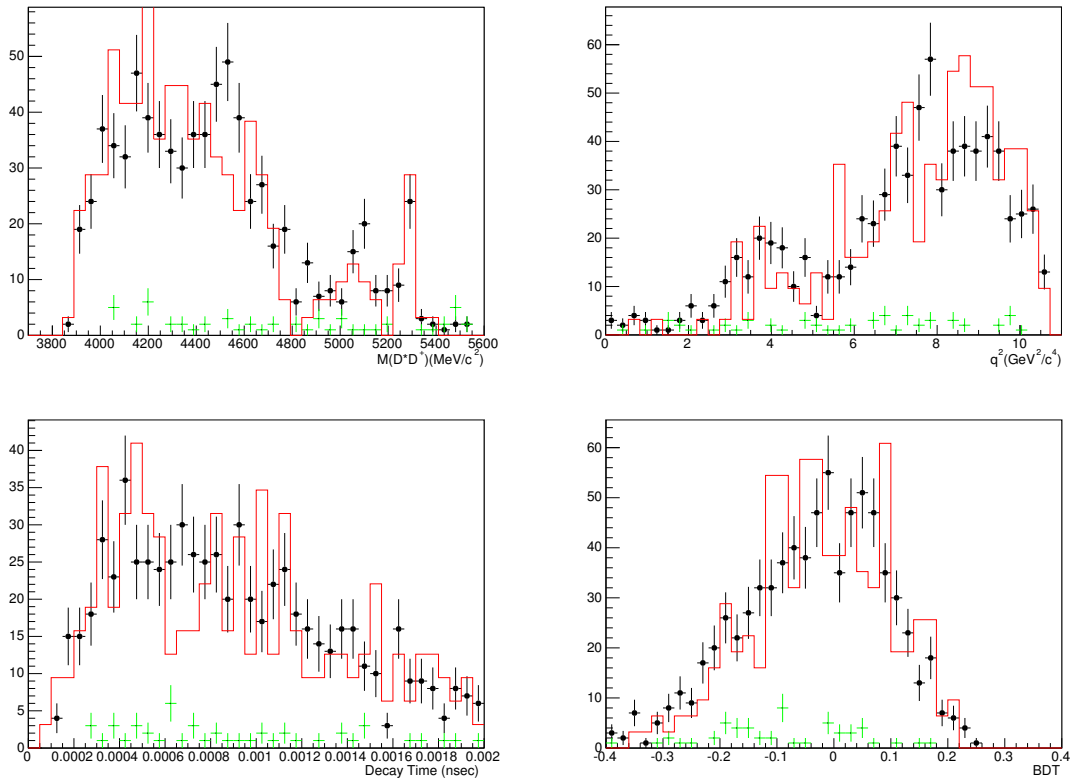

Fig. 5.6 Comparison between data (black points) and the $D^{*-}3\pi X$ inclusive Monte Carlo (red) for the $M(D^{*-}K^-\pi^+\pi^+)$ (top left), q^2 (top right), 3π decay time (bottom left) and BDT (bottom right) distributions for the $B \to D^{*-}D^+X$ control sample. The combinatorial background, described by the wrong-sign events from the corresponding stripping line, is shown in green. It is worth to note the large decay time observed due to the long D^+ lifetime.

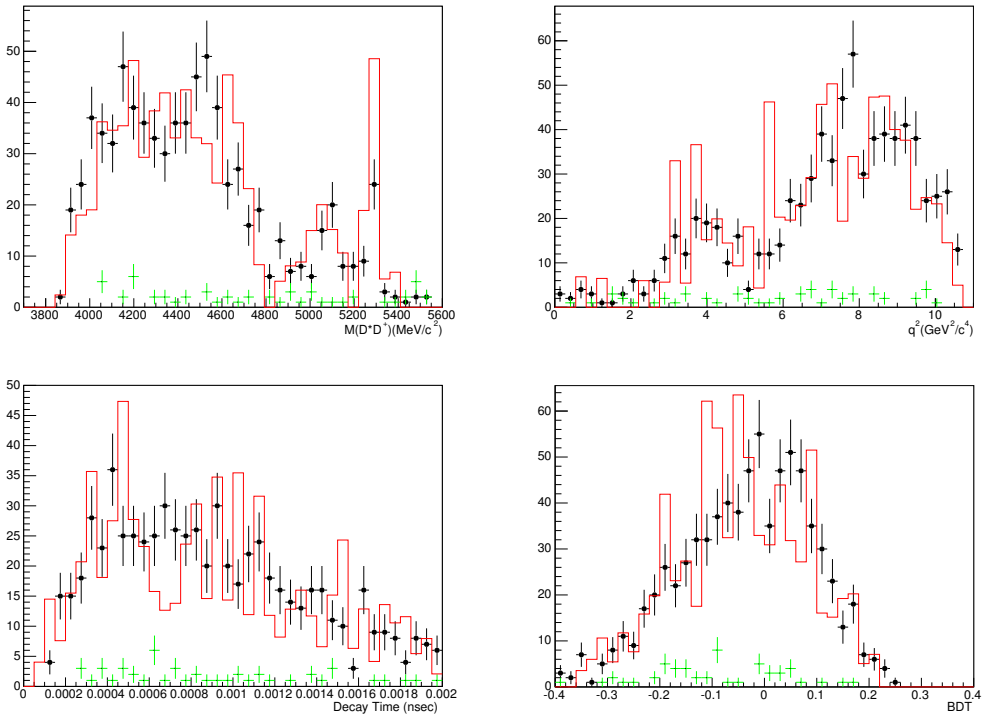

Fig. 5.7 Comparison between data (black points) and the $D^{*-}3\pi X$ inclusive Monte Carlo (red) for the $M(D^{*-}K^-\pi^+\pi^+)$ (top left), q^2 (top right), 3π decay time (bottom left) and BDT (bottom right) distributions for the $B \to D^{*-}D^+X$ control sample after applying the correction on the q^2 distribution. The combinatorial background, described by the wrong-sign events from the corresponding stripping line, is shown in green.

Chapter 6

Determination of the signal and normalization yields

6.1 The fit model

The yield of $B^0 \to D^{*-}\tau^+\nu_\tau$ decays is determined from a three-dimensional binned maximum likelihood fit to the distributions of q^2, 3π decay time (t_τ) and BDT output. Signal and background templates are produced with eight bins in q^2, eight bins in t_τ, and four bins in the BDT output, from the corresponding simulation samples. The model used to fit the data is summarized in Table 6.1 where $k = 1 + F_{D_s} + F_{D_{s0}^*} + F_{D_{s1}'} + F_{D_s}^{B^{0,+}} + F_{D_s}^{B_s^0}$. In the table,

Fit component	Normalization
$B^0 \to D^{*-}\tau^+(\to 3\pi\overline{\nu}_\tau)\nu_\tau$	$N_{\rm sig} \times f_{\tau\to 3\pi\nu}$
$B^0 \to D^{*-}\tau^+(\to 3\pi\pi^0\overline{\nu}_\tau)\nu_\tau$	$N_{\rm sig} \times (1 - f_{\tau\to 3\pi\nu})$
$B \to D^{**}\tau^+\nu_\tau$	$N_{\rm sig} \times f_{D^{**}\tau\nu}$
$B \to D^{*-}D^+X$	$f_{D^+} \times N_{D_s}$
$B \to D^{*-}D^0X$ different vertices	$f_{D^0}^{\nu_1\nu_2} \times N_{D^0}^{\rm SV}$
$B \to D^{*-}D^0X$ same vertex	$N_{D^0}^{\rm SV}$
$B^0 \to D^{*-}D_s^+$	$N_{D_s} \times f_{D_s^+}/k$
$B^0 \to D^{*-}D_s^{*+}$	$N_{D_s} \times 1/k$
$B^0 \to D^{*-}D_{s0}^*(2317)^+$	$N_{D_s} \times f_{D_{s0}^{*+}}/k$
$B^0 \to D^{*-}D_{s1}(2460)^+$	$N_{D_s} \times f_{D_{s1}^+}/k$
$B^{0,+} \to D^{**}D_s^+X$	$N_{D_s} \times f_{D_s^+X}/k$
$B_s^0 \to D^{*-}D_s^+X$	$N_{D_s} \times f_{D_s^+X,s}/k$
$B \to D^{*-}3\pi X$	$N_{B\to D^*3\pi X}$
B1B2 combinatorics	N_{B1B2}
Combinatoric D^{*-}	$N_{{\rm not}D^*}$

Table 6.1 Summary of fit components and their corresponding normalization parameters. The first three components correspond to parameters related to the signal.

- $N_{\rm sig}$ is a free parameter accounting for the yield of signal candidates.
- $f_{\tau\to 3\pi\nu}$ is the fraction of $\tau^+ \to 3\pi\overline{\nu}_\tau$ signal candidates with respect to the sum of the $\tau^+ \to 3\pi\overline{\nu}_\tau$ and $\tau^+ \to 3\pi\pi^0\overline{\nu}_\tau$ components. This parameter is fixed to 0.78, according to the different branching fractions and efficiencies of the two modes.
- $f_{D^{**}\tau\nu}$, fixed to 0.11, is the ratio of the yield of $B \to D^{**}\tau^+\nu_\tau$ decay candidates to the signal decays. This yield is computed assuming that the ratio of the decay rates lies between the ratio of available phase space (0.18) and the predictions of Ref.[6] (0.06), and taking into account the relative efficiencies of the different channels.
- $N_{D^0}^{\rm SV}$ is the yield of $B \to D^{*-}D^0X$ decays where the three pions originate from the same vertex (SV) as the the D^0 vertex. The $D^0 \to K^+\pi^-\pi^+\pi^-(\pi^0)$ decays are reconstructed by recovering a charged kaon pointing to the 3π vertex in nonisolated events. The exclusive $D^0 \to K^+\pi^-\pi^+\pi^-$ peak is used to apply a 5% Gaussian constraint to this parameter, accounting for the knowledge of the efficiency in finding the additional kaon.

- $f_{D^0}^{\nu_1\nu_2}$ is the ratio of $B \to D^{*-}D^0X$ decays where at least one pion originates from the D^0 vertex and the other pion(s) from a different vertex, normalized to $N_{D^0}^{\mathrm{sv}}$. This is the case when the soft pion from a D^{*-} decay is reconstructed as it were produced at the 3π vertex.

- f_{D^+} is the ratio of $B \to D^{*-}D^+X$ decays with respect to those containing a D_s^+ meson.

- N_{D_s} is the yield of events involving a D_s^+. The parameters f_i defined in Sec. 5.2, are used after correcting for efficiency.

- $N_{B\to D^*3\pi X}$ is the yield of $B \to D^{*-}3\pi X$ events where the three pions come from the B vertex. This value is constrained by using the observed ratio between $B^0 \to D^{*-}3\pi$ exclusive and $B \to D^{*-}3\pi X$ inclusive decays, corrected for efficiency.

- N_{B1B2} is the yield of combinatorial background events where the D^{*-} and the 3π system come from different B decays. Its yield is fixed by using the yield of wrong-sign events $D^{*-}\pi^-\pi^+\pi^-$ in the region $m(D^{*-}\pi^-\pi^+\pi^-) > 5.1$ GeV/c^2.

- $N_{\mathrm{not}D^*}$ is the combinatorial background yield with a fake D^{*-}. Its value is fixed by using the number of events in the $\bar{D}^0$ mass sidebands of the $D^{*-} \to \bar{D}^0\pi^-$ decay.

6.2 Fit results

The results of the three-dimensional fit are shown in Table 6.2 and Fig. 6.1.

Parameter	Fit result	Constraint
N_{sig}	1296 ± 86	
$f_{\tau\to 3\pi\nu}$	0.78	0.78 (fixed)
$f_{D^{**}\tau\nu}$	0.11	0.11 (fixed)
$N_{D^0}^{\mathrm{SV}}$	445 ± 22	445 ± 22
$f_{D^0}^{\nu_1\nu_2}$	0.41 ± 0.22	
N_{D_s}	6835 ± 166	
f_{D^+}	0.245 ± 0.020	
$N_{B\to D^*3\pi X}$	424 ± 21	443 ± 22
$f_{D_s^+}$	0.494 ± 0.028	0.467 ± 0.032
$f_{D_{s0}^{*+}}$	$0^{+0.010}_{-0.000}$	$0^{+0.042}_{-0.000}$
$f_{D_{s1}^+}$	0.384 ± 0.044	0.444 ± 0.064
$f_{D_s^+X}$	0.836 ± 0.077	0.647 ± 0.107
$f_{D_s^+X,s}$	0.159 ± 0.034	0.138 ± 0.040
N_{B1B2}	197	197 (fixed)
$N_{\mathrm{not}D^*}$	243	243 (fixed)

Table 6.2 Fit results for the three-dimensional fit. The constraints on the parameters $f_{D_s^+}$, $f_{D_{s0}^{*+}}$, $f_{D_{s1}^+}$, $f_{D_s^+X}$ and $f_{D_s^+X,s}$ are applied taking into account their correlations.

6.2.1 Fit results

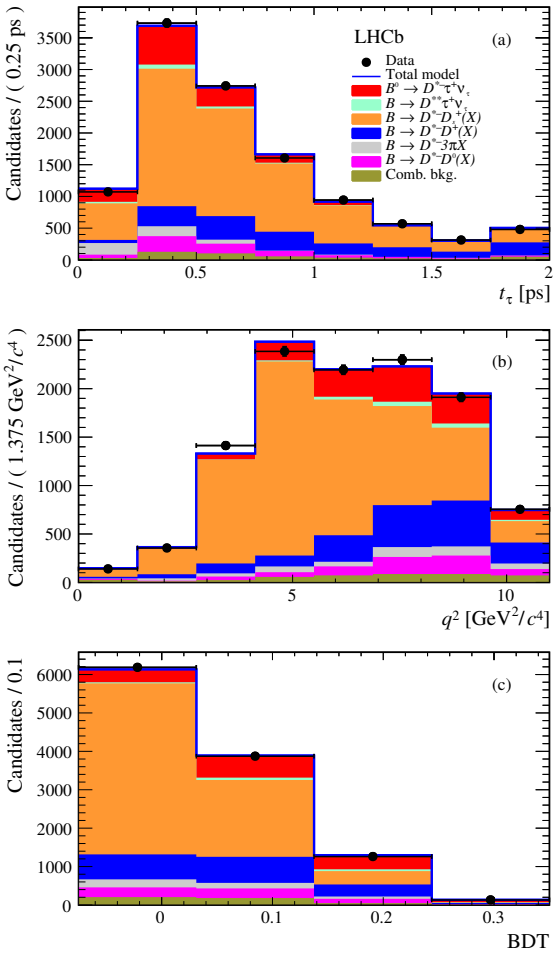

Fig. 6.1 Projections of the three-dimensional fit on the (a) 3π decay time, (b) q^2 and (c) BDT output distributions. The fit components are described in the legend.

A raw yield of 1336 decays translates into a yield of $N_{\text{sig}} = 1296 \pm 86$ $B^0 \to D^{*-}\tau^+\nu_\tau$ decays, after a correction of -3% due to a fit bias is applied, as detailed in Sec. 6.3. Figure 6.2 shows the results of the fit in bins of the BDT output. The two most discriminant variables of the BDT response are the variables $\min[m(\pi^+\pi^-)]$ and $m(D^{*-}3\pi)$.

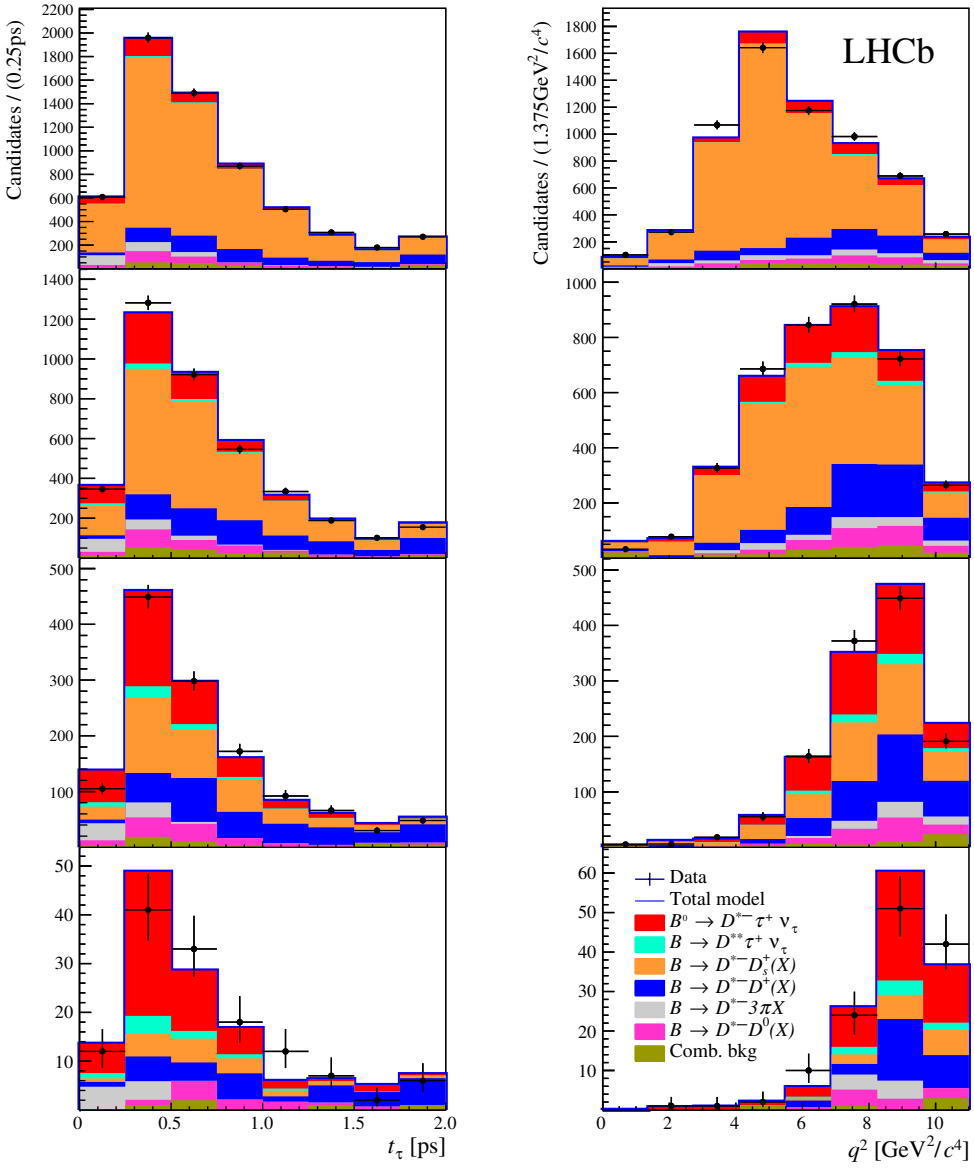

Fig. 6.2 Distributions of (left) t_τ and (right) q^2 in four different BDT bins, with increasing values of the BDT response from top to bottom. The fit components are described in the legend.

Figure 6.3 shows the fit results projected onto these variables. A good agreement with data and the post-fit model is found. The fit χ^2 is 1.15 per degree of freedom, after taking into account the statistical fluctuation in the simulation templates, and 1.8 without. The statistical contribution to the total uncertainty is determined by performing a second fit where the parameters governing the templates shapes of the double-charmed decays, $f_{D_s^+}$, $f_{D_{s0}^{*+}}$, $f_{D_{s1}^+}$, $f_{D_s^+X}$, $f_{D_s^+X,s}$ and $f_{D^0}^{\nu_1\nu_2}$, are fixed to the values obtained in the first fit. The quadratic

difference between the uncertainties provided by the two fits is taken as systematic uncertainty due to the knowledge of the $B \to D^{*-} D_s^+ X$ and $B \to D^{*-} D^0 X$ decay models, and reported in Table 7.1.

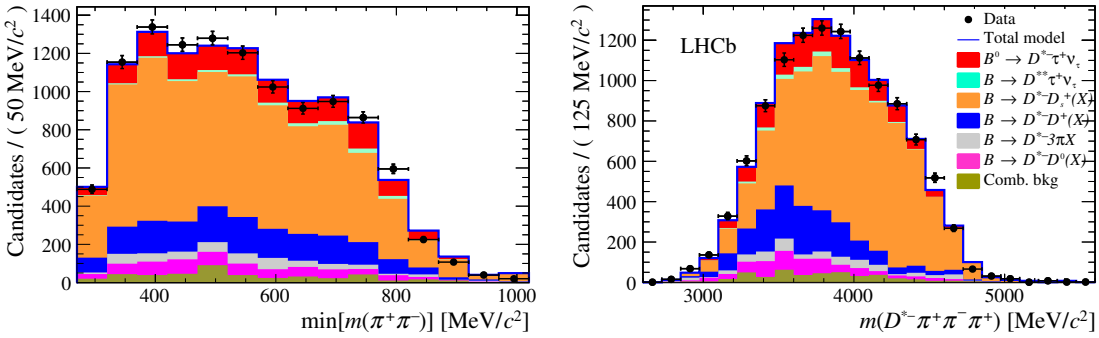

Fig. 6.3 Projection of the fit results on (left) min$[m(\pi^+\pi^-)]$ and (right) $m(D^{*-}3\pi)$ distributions. The fit components are described in the legend.

The results from the nominal fit are used to extrapolate the fit components into the low BDT output. The distributions for min$[m(2\pi)]$, max$[m(2\pi)]$, $m[D^*3\pi]$ and $m[3\pi]$ are shown in Fig. 6.4 in which a general good agreement is exhibited.

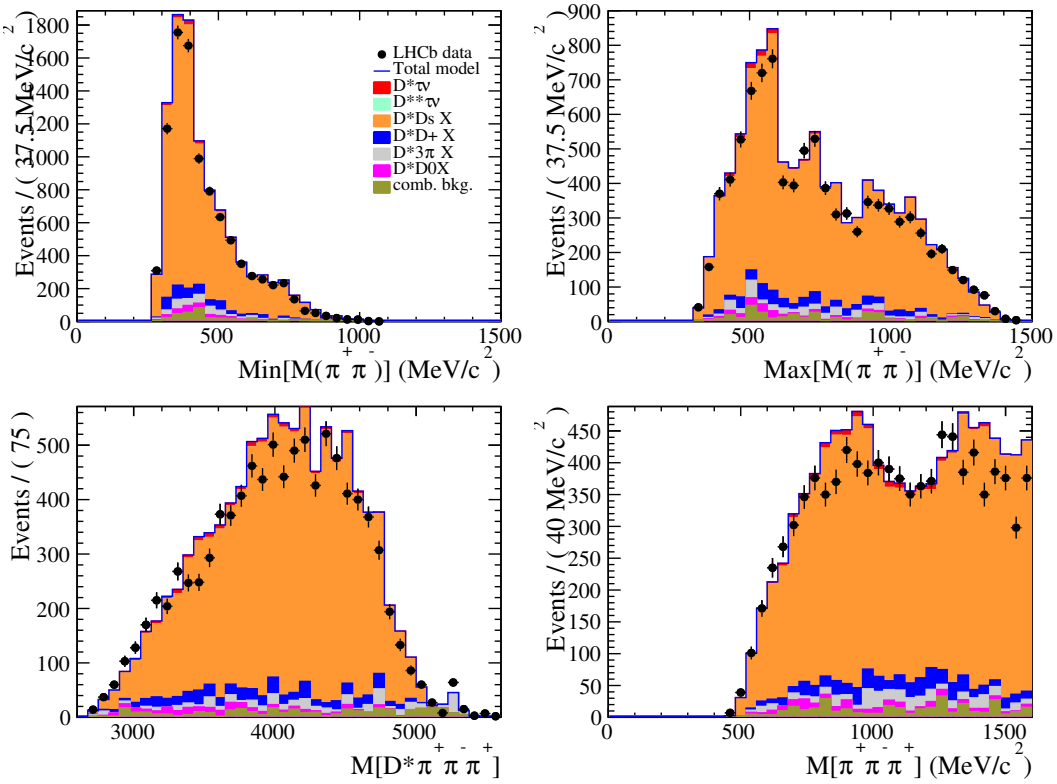

Fig. 6.4 Projection of the nominal fit results to the low bdt region in min$[m(2\pi)]$, max$[m(2\pi)]$, $m[D^*3\pi]$ and $m[3\pi]$.

6.3 Kernel Density Estimator

Due to the limited size of the simulation samples used to build the templates, the existence of empty bins in the templates introduces potential biases in the determination of the signal yield that must be taken into account. To study this effect, a method based on the use of kernel density estimator (KDE) [59] is used. For each simulated sample, a three-dimensional template density function is produced. Each KDE is then transformed in a three-dimensional template, where bins that were previously empty may now be filled. These new templates are used to build a smoothed fit model. The fit is repeated with different signal yield hypotheses. The results show that a bias is observed for low values of the generated signal yield that decreases when the generated signal yield increases, as shown in Fig. 6.5. For the value found by the nominal fit, a bias of +40 candidates is found, and is used to correct the fit result.

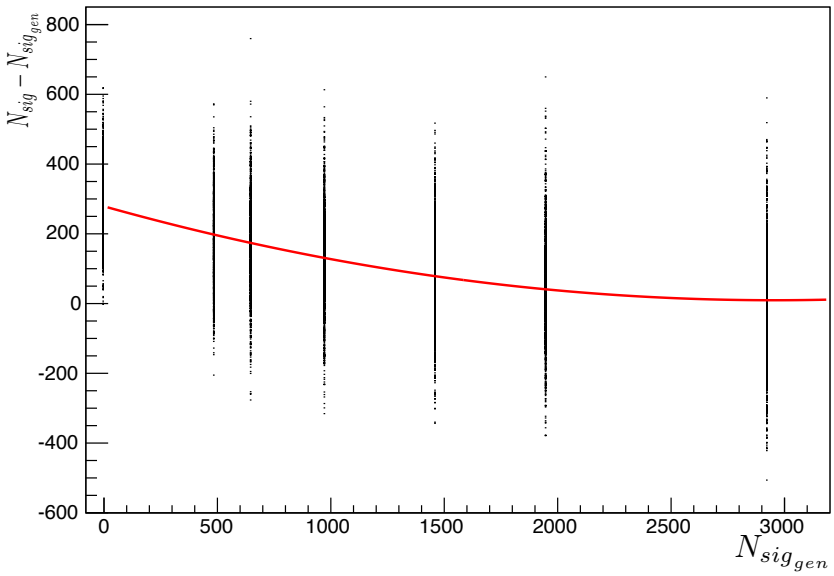

Fig. 6.5 Difference between the signal yield from the fits and the generated yield with respect to the generated value. At the nominal value, the fit bias is +40 events, which must be used to correct the signal yield obtained in the nominal fit.

6.4 Normalization through the $B^0 \to D^{*-}3\pi$ exclusive peak

Figure 4.5 shows the D^{*-} 3π mass after the selection of the normalization sample (see Sec. 4.2). A clean B^0 peak is seen. In order to determine the normalization yield, a fit is performed in the region between 5150 and 5400 MeV/c^2. The signal component is described by the sum of a Gaussian function and a Crystal Ball function [60]. An exponential function is used to describe the background. The result of the fit is shown in Fig. 6.6. The total obtained yield is 17808 ± 143. The fit is also performed with alternative configurations, namely with different fit range or requiring a common mean value of the signal functions in the 7 and 8 TeV data samples. The maximum differences between signal yields in alternative and nominal configurations are 14 and 62 for 2011 and 2012 data samples respectively, and are used to assign systematic uncertainties to the normalization yields.

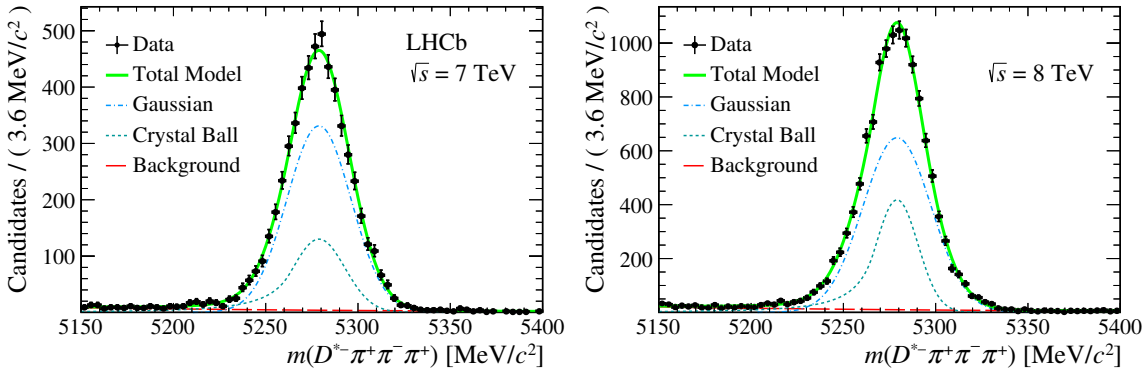

Fig. 6.6 Fit to the $m(D^{*-}3\pi)$ distribution after the full selection in the (left) $\sqrt{s} = 7$ TeV and (right) 8 TeV data samples.

Figure 6.7 shows the $m(3\pi)$ distribution for candidates with D^{*-} 3π mass between 5200 and 5350 MeV/c^2 for the full data sample. The spectrum is dominated by the $a_1(1260)^+$ resonance but also a smaller peak due to the $D_s^+ \to 3\pi$ decay is visible and is subtracted. A fit with the sum of a Gaussian function modeling the D_s^+ mass peak, and an exponential describing the combinatorial background, is performed to estimate this D_s^+ contribution, giving 151 ± 22 candidates. As a result, the number of normalization decays in the full data sample is $\mathrm{N}_{norm} = 17\,657 \pm 143\,(\mathrm{stat}) \pm 64\,(\mathrm{syst}) \pm 22\,(\mathrm{sub})$, where the third uncertainty is due to the subtraction of the $B^0 \to D^{*-}D_s^+$ component.

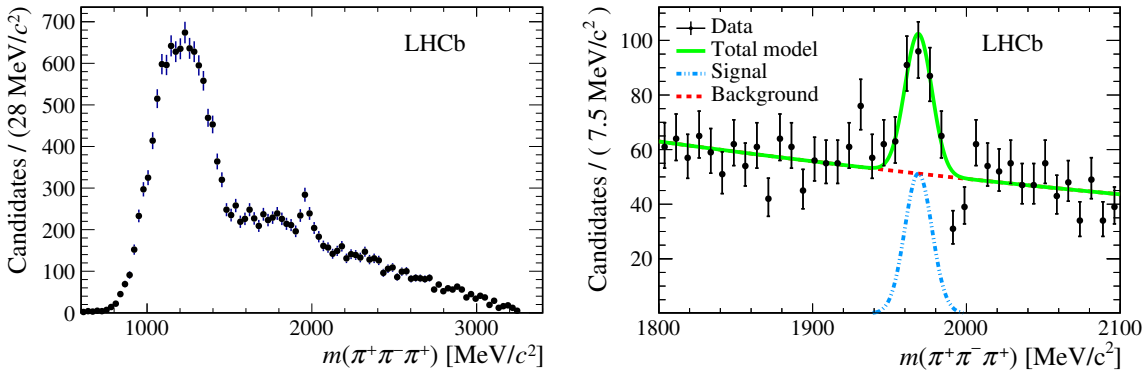

Fig. 6.7 (left) Distribution of $m(3\pi)$ after selection, requiring $m(D^{*-}3\pi)$ to be between 5200 and 5350 MeV/c^2; (right) fit in the mass region around the D_s^+.

6.5 Correction factors

Several corrections factors have to be applied in order to get a measurement of $\mathscr{K}(D^{*-})$. Three of them are due to the fact that, in the Monte-Carlo simulation used to compute the respective efficiencies for the signal and the normalization channels, some imperfections observed in the simulation with respect to the data, namely the efficiency of the L0S TOS hadron, and the efficiency of the HLT2 trigger, may not cancel exactly in the ratio between signal and normalization simulations. The fourth one is due to the SPD correction to the normalization MC efficiency, arising from the fact that data and MC disagree in the TOS-nonTOS proportions on the B^0 peak used for normalization, which is due to an underestimation of the SPD multiplicity in MC, multiplicty which is driving the efficiency of the TIS (ie non TOS) triggers. Finally, we have to take into account the small feed-down from $B_s^0 \to D^* \tau \nu K^0$ events due to the $B_s^0 \to D_s^{+**} \tau \nu$ channel wher the D_s^{+**} decays to $D^* K^0$. We did not include this feed-down in the D^{**} fraction used in the global fit below in order to keep the D^{**} contribution from B^0 and B^+ identical to what is observed in B-factories, where no B_s^0 contribution is present. The PID correction factor is equal to 1. since the PID efficiencies are taken directly from the data, with the PIDCAlib system. The first two other corrections factors, the L0hadron correction and the HLT2 correction, are described in Sec. 3.3 and 3.4 respectively. The initial size of the data/MC correction ranges from 10% to 25% but the residual size is in the ratio much smaller in all cases. The correction factors multiplying the number of expected events are:

- L0 hadron correction is 0.995±0.01
- the HLT2 correction factor is 1.00±0.005
- the SPD correction is 1/(0.97±0.01)
- feed-down from B_s^0 1.03±0.015

Overall, the global correction factor to the number of expected events is 1.056±0.025.

6.6 Determination of $\mathscr{K}\left(D^{*-}\right)$

The result

$$\mathscr{K}(D^{*-}) = 1.97 \pm 0.13\,(\text{stat}) \pm 0.18\,(\text{syst}),$$

is obtained using Eq. 2. The ratio of efficiencies between the signal and normalization modes, shown in Table 4.2, differs from unity due to the softer momentum spectrum of the

signal particles and the correspondingly lower trigger efficiency. The effective sum of the branching fractions for the $\tau^+ \to 3\pi\overline{\nu}_\tau$ and $\tau^+ \to 3\pi\pi^0\overline{\nu}_\tau$ decays is $13.81\% \pm 0.076\%$ [20]. This includes the 3π mode (without K^0), a very small feeddown from τ five-prong decays, the $3\pi\pi^0$ mode(without K^0), and only 50% of the $3\pi\pi^0\pi^0$ mode due to the smaller efficiency of this decay mode. This latter contribution results in a 1% correction (see Sec. 7.1). The event multiplicity, measured by the scintillating-pad detector, affects the efficiency for the fraction of the data sample which is triggered at the hardware trigger level by particles in the event other than those from the $D^{*-}\tau^+\nu_\tau$ candidate. An imperfect description of this multiplicity in the simulation does not cancel completely in $\mathscr{K}(D^{*-})$. The correction factor also includes a small feeddown contribution from $B_s^0 \to D_s^{**-}\tau^+\nu_\tau$ decays, where $D_s^{**-} \to D^{*-}K^0$, that is taken into account according to simulation.

As a further check of the analysis, measurements of $\mathscr{K}(D^{*-})$ are performed in mutually exclusive subsamples, obtained by requiring different trigger conditions and center-of-mass energies. All of these results are found to be compatible with the result obtained with the full sample.

Chapter 7

Systematic uncertainties

The systematic uncertainties on $\mathscr{K}(D^*)$ are divided in four categories, related to: the knowledge of the signal model, including τ decay models; the modeling of the various background sources; possible biases in the fit procedure due to the limited size of the simulated samples; trigger selection efficiencies, external inputs, and particle identification efficiency.

7.1 Signal model uncertainties

7.1.1 τ branching fractions

An uncertainty of 0.01 is assigned to the knowledge of the ratio $\mathscr{B}(\tau^+ \to 3\pi\pi^0\overline{\nu}_\tau)/\mathscr{B}(\tau^+ \to 3\pi(\pi^0)\overline{\nu}_\tau)$, taking into account the relative efficiencies. A fit is performed with this fraction gaussianly constrained to 0.78 ± 0.01. A second fit is done fixing the fraction to the value found by the first fit. The squared difference between the uncertainties of the two fits is taken as the systematic uncertainty due to the signal composition, resulting in a 0.7% systematic uncertainty.

7.1.2 Form factors

To estimate the systematic uncertainty due to the knowledge of the $B^0 \to D^{*-}$ form factors, a study based on simulated pseudoexperiments is performed. A total of 100 fits to generated samples is done varying the values of the parameters $R_1(1)$, $R_2(1)$, ρ^2 [6] which represent the fraction of each spin-configuration in the form factor templates. The parameters are gaussianly varied using their uncertainties and correlations. The parameter $R_0(1) = 1.14 \pm 0.11$ is varied assuming it is not correlated with the other parameters. A systematic uncertainty

of 0.7% on the signal yield is obtained by taking the standard deviation of the distribution of the fitted signal yields.

7.1.3 τ polarization

The effect of the τ polarization is studied separately for $\tau^+ \to 3\pi\overline{\nu}_\tau$ and $\tau^+ \to 3\pi\pi^0\overline{\nu}_\tau$.Due to the $a_1(1260)$ dominance observed in the channel $\tau^+ \to 3\pi\overline{\nu}_\tau$, the sensitivity to the polarization is negligible, therefore no systematic uncertainty is assigned to this effect in this channel. For the $\tau^+ \to 3\pi\pi^0\overline{\nu}_\tau$ decay mode, the signal is simulated in two configurations: using either the `Tauola` model or a pure phase space model. The effect of the τ polarization is evaluated by multiplying the efficiency by the ratio of the distributions generated with the two configurations. This produces a change in the efficiency of 1.5%. This value, scaled by the relative fraction of the $\tau^+ \to 3\pi\pi^0\overline{\nu}_\tau$ component with respect to the total, gives a systematic uncertainty of 0.4%.

7.1.4 Other τ decays

Other τ decays could contribute to the signal yield. They are either decays with three charged tracks in the final states ($K\pi\pi$, $KK\pi$, $\pi\pi\pi\pi^0\pi^0$) or 5 charged tracks, all of them having very small branching fractions compared to the $\tau^+ \to 3\pi(\pi^0)\overline{\nu}_\tau$ mode. The study of a dedicated simulation sample with inclusive τ decays indicates an effect of 1% due to other decays which do not correspond to the τ decay channels used in this analysis. This is assigned as a systematic uncertainty.

7.1.5 $B \to D^{**}\tau\nu_\tau$ and $B_s \to D_s^{**}\tau\nu_\tau$

The $B \to D^{**}\tau\nu_\tau$ fraction used for the nominal fit, 0.11, is assigned a 40% uncertainty, based on the results of an auxiliary study of $B^- \to D_1(2420)^0\tau^+\nu_\tau$ decays, where $D_1(2420)^0 \to D^{*-}\pi^+$. This results in a systematic uncertainty on the signal yield of 2.3%. An additional systematic uncertainty of 1.5% due to the $B_s^0 \to D_s^{**}\tau^+\nu_\tau$ decays contribution is assigned, under the assumption that the yield of these decays in the simulation has an uncertainty of 50%, determined to be the upper limit from a study performed on simulated data.

7.2 Background-related systematic uncertainties

This section lists the systematic uncertainties due to the modelling of different background sources, such as the D_s^+ decay model, double-charm and combinatorial contributions.

7.2.1 D_s^+ decay model

Candidates in the low BDT output region are used to correct the composition of D_s^+ decays in simulation. From the fit to this data sample corrections are obtained, which are used to generate 1000 alternative D_s^+ templates for each D_s^+ component in the nominal 3D fit. Each alternative template is produced by gaussianly varying the nominal template accounting for the uncertainty and correlations between the D_s^+ sub-components. These alternative templates are employed to re-fit the data and to estimate the systematic uncertainty. The difference between the signal yield of the alternative and the nominal fits, divided by the yield of the nominal fit, is fitted with a Gaussian function in order to obtain the systematic uncertainty which is found to be 2.5%.

7.2.2 Double-charm decay model

The kinematic variables expected to be significantly correlated with the fit variables are: $m(D^*3\pi)$, $m(3\pi)$, $\min[m(\pi^+\pi^-)]$, $\max[m(\pi^+\pi^-)]$ and $m(\pi^+\pi^+)$ invariant masses. The corresponding effect on the fit result of these variables is empirically studied by varying the distributions using a quadratic interpolation method: for each template, two alternative templates are produced, with a variation of $\pm 1\sigma$. with respect to the nominal template. Then, the fit enables the interpolation between the nominal and the alternative templates to be made with a linear weight. Each nuisance parameter is allowed to float in the range $[-1,+1]$ and a loose Gaussian constraint with $\sigma = 1$ is included. This method is used to compute systematic uncertainties due to the knowledge of the templates shape. The corresponding systematic uncertainty is of 2.9%. A systematic uncertainty of 2.6% is due to the composition of the $B \to D^{*-} D_s^+ X$ and $B \to D^{*-} D^0 X$ decays, as mentioned in Sec. 6.1.

7.2.3 Prompt background

The systematic uncertainty due to the knowledge of the shape of the residual prompt background component is estimated by applying the interpolation technique described previously to the corresponding template. When combined with the knowledge of the normalization of this background, this gives an overall uncertainty of 2.5%.

7.2.4 Combinatorial background

The interpolation technique used to compute the systematic uncertainties relative to the double-charm decay model and the prompt background is also employed to assess the systematic uncertainty due to the shape of the combinatorial background. The result in the

change of the signal yield provides a systematic uncertainty of 0.7%. Another systematic uncertainty is due to the normalization of this background. This uncertainty is computed by performing the fit with a 30% Gaussian constraint around the nominal value. The resulting difference with the nominal fit is 0.1% and it is assigned as systematic uncertainty.

7.3 Fit-related systematic uncertainties

This section lists the systematic uncertainties related to a possible bias in the fit procedure and the size of the simulation samples.

7.3.1 Fit bias

The study performed using kernel density estimation method has been repeated using different smoothing parameters. A difference in the signal yield of 1.3% is assigned as systematic uncertainty due to the fit bias.

7.3.2 Systematic due to the size of the simulation samples

In order to estimate the systematic uncertainty due the limited size of the simulation samples, a boostrap method is used. Each template from the nominal model is used to produce new templates sampled from the originals by using a bootstrap procedure [61] (random selection with replacement), varied bin-by-bin according to a Poisson distribution. This procedure is repeated 500 times. A Gaussian fit to the distributions of signal yields provides a 4.1% effect taken as the systematic uncertainty due to the template statistics.

7.4 Uncertainties related to the selection

In this section systematic uncertainties related to the selection criteria are listed. Such uncertainties derive from the choice of the trigger strategy, to the online and offline selection of the candidates, to the normalization and external inputs, and to the efficiency of the particle identification criteria.

7.4.1 Trigger efficiency

The trigger efficiency is studied as a function of the two most important variables in this analysis that are $\tau_{3\pi}$ and $m(D^*3\pi)$, the latter being highly correlated with q^2. Corrections on the $\tau_{3\pi}$ and $m(D^*3\pi)$ distributions due to different trigger efficiency between data and

simulation are applied. This gives a change on the number of signal candidates of 1.0% for the $\tau_{3\pi}$ and 0.7% for the $m(D^*3\pi)$ corrections. The sum in quadrature of these two contributions is taken as systematic uncertainty related to the trigger efficiency. An additional 1% systematic uncertainty arises from a mismatch between data and simulation in the distribution of the detector occupancy of the event.

7.4.2 Online and offline selection

The relative efficiency between the signal and the normalization channels is precisely measured on simulation. Discrepancies between data and simulation, due to offline selection criteria, introduce a 2% of systematic uncertainty. A 1% systematic uncertainty is assigned on the charged isolation criterium, due to differences observed between the $B^0 \to D^{*-}\tau\nu_\tau$ and the $B^0 \to D^{*-}3\pi$ simulations.

All selection cuts, except the detached vertex topology requirement, are common to the signal and normalization channels. Their efficiency are therefore directly determined on data using the $B^0 \to D^*3\pi$ mass peak and no systematics uncertainty is assigned. To compute the systematic uncertainty attributed to the knowledge of the relative efficiences corresponding to the different signal and normalisation vertex topologies, the vertex error distribution is splitted in three regions: between -4 and -2σ, between -2 and 2σ and between 2 and 4σ. Then a ratio between the number of candidates in the outer regions and the number of candidates in the inner region is computed for the candidates which have $m(D^*3\pi)$ in the exclusive $B^0 \to D^{*-}3\pi$ peak. The same is done for the candidates outside the $B^0 \to D^{*-}3\pi$ peak, which are assumed to have a signal-like behavior. The procedure is repeated for data, and the ratio between data and simulation provides a 2% systematic uncertainty.

7.4.3 Normalization and external inputs

The normalization channel consists of exactly the same final state and is treated exactly as the signal for trigger, selection, particle identification, charged and neutral isolation, and vertex requirements. This allows to limit differences between data and simulation. The systematic uncertainty on the normalization yield, determined using different fit configuration, is equal to 1%. The statistical error attached to the normalization yield is included in the statistical uncertainty.

7.4.4 Particle identification

Simulation is corrected in order to match the performance of particle identification criteria measured in data. Correction factors are applied in bins of momentum, pseudorapidity and global event multiplicity. To assess the systematic uncertainty due to the choice of binning scheme used to correct simulation, two new schemes are derived from the default one with half and twice the number of bins, the default configuration consisting of six bins in momentum, six in pseudorapidity and three in the global event multipliciy. The correction procedure is repeated with these two alternate schemes, leading to a systematic uncertainty due to particle identification of 1.3%.

7.5 Summary of systematic uncertainties

The precise knowledge of the branching fraction for the normalization channel $B^0 \to D^{*-}3\pi$ is crucial for the measurement of $\mathscr{R}(D^*)$. From the weighted average of the measurements by the LHCb [62], BABAR [63],and BELLE [64] collaborations, the $\mathscr{B}(B^0 \to D^{*-}\pi^+\pi^-\pi^+)$ is known with 7% accuracy [20]. A 2% uncertainty coming from the knowledge of the $B^0 \to D^{*-}\mu^+\nu_\mu$ branching fraction is added in quadrature to obtain a 7.3% total uncertainty on $\mathscr{R}(D^*)$ due to external inputs.

Table 7.1 summarizes the systematic uncertainties on the measurement of the ratio $\mathscr{B}(B^0 \to D^{*-}\tau^+\nu_\tau)/\mathscr{B}(B^0 \to D^{*-}3\pi)$. The total uncertainty is 9.1%. For $\mathscr{R}(D^{*-})$, a 7.3% systematic uncertainty due to the knowledge of the external branching fractions is added.

Contribution	Value in %
$\mathscr{B}(\tau^+ \to 3\pi\overline{\nu}_\tau)/\mathscr{B}(\tau^+ \to 3\pi(\pi^0)\overline{\nu}_\tau)$	0.7
Form factors (template shapes)	0.7
τ polarization effects	0.4
Other τ decays	1.0
$B \to D^{**}\tau^+\nu_\tau$	2.3
$B_s^0 \to D_s^{**}\tau^+\nu_\tau$ feeddown	1.5
$D_s^+ \to 3\pi X$ decay model	2.5
D_s^+, D^0 and D^+ template shape	2.9
$B \to D^{*-}D_s^+(X)$ and $B \to D^{*-}D^0(X)$ decay model	2.6
$D^{*-}3\pi X$ from B decays	2.8
Combinatorial background (shape + normalization)	0.7
Bias due to empty bins in templates	1.3
Size of simulation samples	4.1
Trigger acceptance	1.2
Trigger efficiency	1.0
Online selection	2.0
Offline selection	2.0
Charged-isolation algorithm	1.0
Normalization channel	1.0
Particle identification	1.3
Signal efficiencies (size of simulation samples)	1.7
Normalization channel efficiency (size of simulation samples)	1.6
Normalization channel efficiency (modeling of $B^0 \to D^{*-}3\pi$)	2.0
Form factors (efficiency)	1.0
Total uncertainty	9.1

Table 7.1 List of the individual systematic uncertainties for the measurement of the ratio $\mathscr{B}(B^0 \to D^{*-}\tau^+\nu_\tau)/\mathscr{B}(B^0 \to D^{*-}3\pi)$.

Conclusion

In conclusion, the ratio of branching fractions between the $B^0 \to D^{*-}\tau^+\nu_\tau$ and the $B^0 \to D^{*-}3\pi$ decays is measured to be

$$\mathscr{K}(D^{*-}) = 1.97 \pm 0.13\,(\text{stat}) \pm 0.18\,(\text{syst}),$$

where the first uncertainty is statistical and the second systematic. Using the branching fraction $\mathscr{B}(B^0 \to D^{*-}3\pi) = (7.214 \pm 0.28) \times 10^{-3}$ from the weighted average of the measurements by the LHCb [62], BABAR [63], and BELLE [64] collaborations, a value of the absolute branching fraction of the $B^0 \to D^{*-}\tau^+\nu_\tau$ decay is obtained

$$\mathscr{B}(B^0 \to D^{*-}\tau^+\nu_\tau) = (1.42 \pm 0.09\,(\text{stat}) \pm 0.13\,(\text{syst}) \pm 0.054\,(\text{ext})) \times 10^{-2},$$

where the third uncertainty originates from the limited knowledge of the branching fraction of the normalization mode. The precision of this measurement is comparable to that of the current world average of Ref. [20]. The first determination of $\mathscr{R}(D^{*-})$ performed by using three-prong τ decays is obtained by using the measured branching fraction of $\mathscr{B}(B^0 \to D^{*-}\mu^+\nu_\mu) = (4.88 \pm 0.10) \times 10^{-2}$ from Ref. [27]. The result

$$\mathscr{R}(D^{*-}) = 0.291 \pm 0.019\,(\text{stat}) \pm 0.026\,(\text{syst}) \pm 0.013\,(\text{ext})$$

is one of the most precise single measurements performed so far. It is 1.1 standard deviations higher than the SM prediction (0.252 ± 0.003) of Ref. [6], and consistent with previous determinations. An average of this measurement with the LHCb result using $\tau^+ \to \mu^+\nu_\mu\overline{\nu}_\tau$ decays [25], accounting for small correlations due to form factors, τ polarization and $D^{**}\tau^+\nu_\tau$ feed-down, gives a value of $\mathscr{R}(D^{*-}) = 0.310 \pm 0.0155\,(\text{stat}) \pm 0.0219\,(\text{syst})$, consistent with the world average and 2.2 standard deviations above the SM prediction. A summary of the status of the $\mathscr{R}(D^{*-})$ measurements perfomed by BaBar, Belle and LHCb is shown in Figure 7.1. Figure 7.2 displays the $\mathscr{R}(D)$ vs. $\mathscr{R}(D^*)$ measurements and the current theoretical predictions, indicating a 4.1σ discrepancy between theory and experiment.

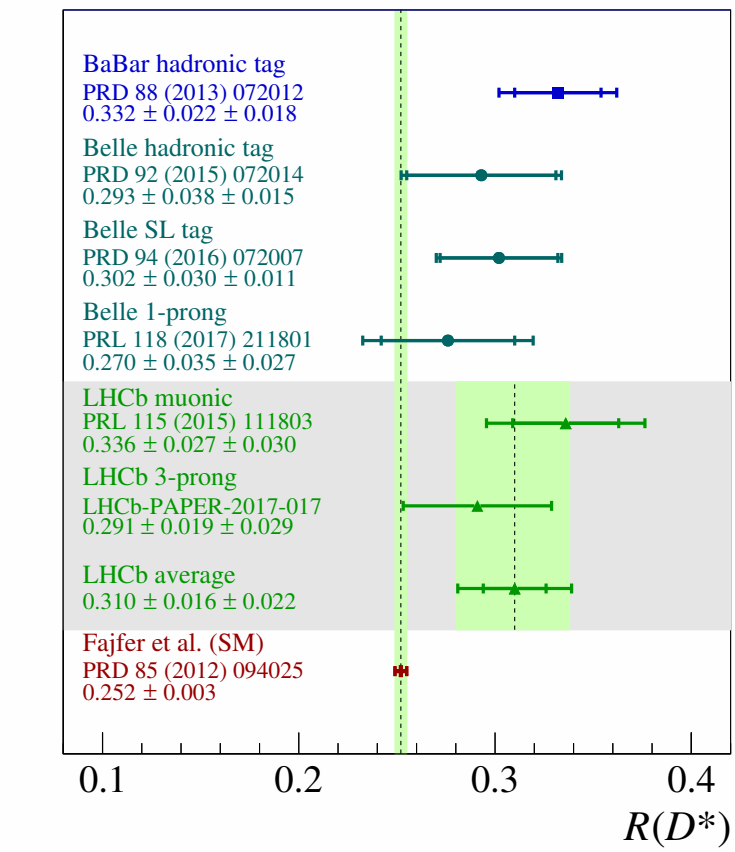

Fig. 7.1 Status of the measurements of $\mathscr{R}(D^*)$ performed by BaBar, Belle and LHCb, including the results of this analysis, and the SM prediction.

The novel technique presented in this thesis, allowing the reconstruction and selection of semitauonic decays with $\tau^+ \to 3\pi(\pi^0)\overline{\nu}_\tau$ transitions, can be applied to all the other semitauonic decays, such as those of B^+, B_s^0, B_c^+ and Λ_b^0. This technique also allows isolation of large signal samples with high purity, which can be used to measure angular distributions and other observables proposed in the literature and opens new opportunities in the search of new physics effects in semileptonic B decays.

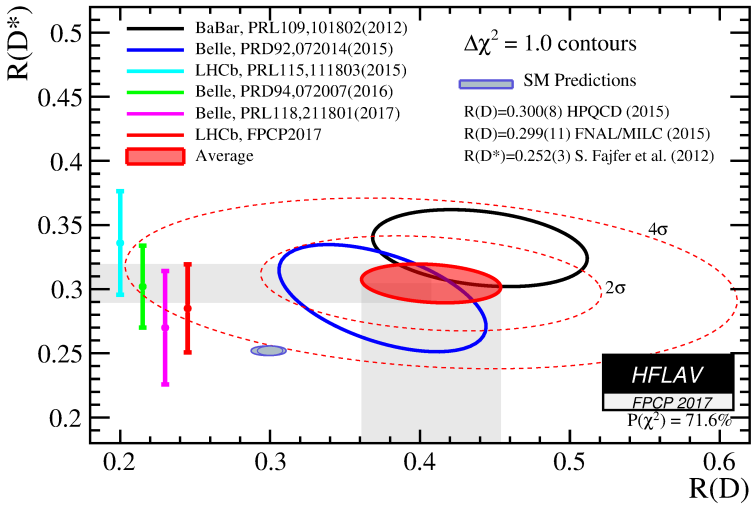

Fig. 7.2 Combination of the measurements of $\mathscr{R}(D)$ vs. $\mathscr{R}(D^*)$ performed by BaBar, Belle and LHCb, including the results of this analysis, and the SM prediction.

References

[1] M. Tanaka. Charged Higgs effects on exclusive semitauonic B decays. *Z. Phys.*, C67:321–326, 1995.

[2] Darius A. Faroughy, Admir Greljo, and Jernej F. Kamenik. Confronting lepton flavor universality violation in b decays with high-pt tau lepton searches at lhc. *Physics Letters B*, 764(Supplement C):126 – 134, 2017.

[3] I. Doršner, S. Fajfer, A. Greljo, J.F. Kamenik, and N. Košnik. Physics of leptoquarks in precision experiments and at particle colliders. *Physics Reports*, 641:1 – 68, 2016.

[4] Florian U. Bernlochner, Zoltan Ligeti, Michele Papucci, and Dean J. Robinson. Combined analysis of semileptonic B decays to D and D^*: $R(D^{(*)})$, $|V_{cb}|$, and new physics. *Phys. Rev.*, D95:115008, 2017.

[5] Sneha Jaiswal, Soumitra Nandi, and Sunando Kumar Patra. Extraction of $|V_{cb}|$ from $B \to D^{(*)}\ell\nu_\ell$ and the Standard Model predictions of $R(D^{(*)})$. 2017.

[6] Svjetlana Fajfer, Jernej F. Kamenik, and Ivan Nisandzic. On the $B \to D^*\tau\bar{\nu}_\tau$ Sensitivity to New Physics. *Phys. Rev.*, D85:094025, 2012.

[7] J. P. Lees et al. Measurement of an excess of $\bar{B} \to D^{(*)}\tau^-\overline{\nu}_\tau$ decays and implications for charged Higgs bosons. *Phys. Rev.*, D88:072012, 2013.

[8] J. P. Lees et al. Evidence for an excess of $\bar{B} \to D^*\tau^-\overline{\nu}_\tau$ decays. *Phys. Rev. Lett.*, 109:101802, 2012.

[9] M. Huschle et al. Measurement of the branching ratio of $\bar{B} \to D^{(*)}\tau^-\overline{\nu}_\tau$ relative to $\bar{B} \to D^{(*)}\ell^-\overline{\nu}_\ell$ decays with hadronic tagging at Belle. *Phys. Rev.*, D92:072014, 2015.

[10] Y. Sato et al. Measurement of the branching ratio of $\bar{B}^0 \to D^{*+}\tau^-\overline{\nu}_\tau$ relative to $\bar{B}^0 \to D^{*+}\ell^-\overline{\nu}_\ell$ decays with a semileptonic tagging method. *Phys. Rev.*, D94:072007, 2016.

[11] Roel Aaij et al. Measurement of the ratio of branching fractions $\mathscr{B}(\overline{B}^0 \to D^{*+}\tau^-\overline{\nu}_\tau)/\mathscr{B}(\overline{B}^0 \to D^{*+}\mu^-\overline{\nu}_\mu)$. *Phys. Rev. Lett.*, 115(11):111803, 2015.

[12] S. Hirose et al. Measurement of the τ lepton polarization and $R(D^*)$ in the decay $\bar{B} \to D^*\tau^-\overline{\nu}_\tau$. *Phys. Rev. Lett.*, 118:211801, 2017.

[13] Abdus Salam. Weak and Electromagnetic Interactions. *Conf. Proc.*, C680519:367–377, 1968.

[14] Steven Weinberg. A model of leptons. *Phys. Rev. Lett.*, 19:1264–1266, Nov 1967.

[15] S. L. Glashow. Partial Symmetries of Weak Interactions. *Nucl. Phys.*, 22:579–588, 1961.

[16] Makoto Kobayashi and Toshihide Maskawa. Cp-violation in the renormalizable theory of weak interaction. *Progress of Theoretical Physics*, 49(2):652–657, 1973.

[17] K. et al. Hagiwara. Review of particle properties. *Phys. Rev. D*, 66:010001, Jul 2002.

[18] Lincoln Wolfenstein. Parametrization of the kobayashi-maskawa matrix. *Phys. Rev. Lett.*, 51:1945–1947, Nov 1983.

[19] C.D. Froggatt and H.B. Nielsen. Hierarchy of quark masses, cabibbo angles and cp violation. *Nuclear Physics B*, 147(3):277 – 298, 1979.

[20] C. Patrignani et al. Review of particle physics. *Chin. Phys.*, C40:100001 and 2017 update, 2016.

[21] Irinel Caprini, Laurent Lellouch, and Matthias Neubert. Dispersive bounds on the shape of $\overline{\mathrm{B}} \to \mathrm{D}^{(*)}$ lepton anti-neutrino form-factors. *Nucl. Phys.*, B530:153–181, 1998.

[22] W. Dungel et al. Measurement of the form factors of the decay $\bar{B}^0 \to D^{*-}\ell^+\nu$ and determination of the CKM matrix element $|V_{cb}|$. *Phys. Rev.*, D82:112007, 2010.

[23] Dante Bigi and Paolo Gambino. Revisiting $B \to D\ell\nu$. *Phys. Rev.*, D94:094008, 2016.

[24] Dante Bigi, Paolo Gambino, and Stefan Schacht. $R(D^*)$, $|V_{cb}|$, and the Heavy Quark Symmetry relations between form factors. 2017.

[25] R. Aaij et al. Measurement of the ratio of branching fractions $\mathscr{B}(\bar{B}^0 \to D^{*+}\tau^-\overline{\nu}_\tau)/\mathscr{B}(\bar{B}^0 \to D^{*+}\mu^-\overline{\nu}_\mu)$. *Phys. Rev. Lett.*, 115:111803, 2015.

[26] S. Hirose et al. Measurement of the τ lepton polarization and $R(D^*)$ in the decay $\bar{B} \to D^*\tau^-\bar{\nu}_\tau$ with one-prong hadronic τ decays at Belle. 2017.

[27] Y. Amhis et al. Averages of b-hadron, c-hadron, and τ-lepton properties as of summer 2016. 2016. updated results and plots available at `http://www.slac.stanford.edu/xorg/hflav/`.

[28] Andreas Crivellin, Christoph Greub, and Ahmet Kokulu. Explaining $b \to d\tau\nu$, $b \to D^*\tau\nu$ and $b \to \tau\nu$ in a two higgs doublet model of type iii. *Phys. Rev. D*, 86:054014, Sep 2012.

[29] Andreas Crivellin, Dario Müller, and Toshihiko Ota. Simultaneous explanation of r(d (∗)) and b→sμ + μ −: the last scalar leptoquarks standing. *Journal of High Energy Physics*, 2017(9):40, Sep 2017.

[30] et Al. Barbosa-Marinho. *LHCb VELO (VErtex LOcator): Technical Design Report*. Technical Design Report LHCb. CERN, Geneva, 2001.

[31] Barbara Sciascia. LHCb Run 2 Trigger Performance. *PoS*, BEAUTY2016(LHCb-PROC-2016-020. CERN-LHCb-PROC-2016-020):029. 7, May 2016.

[32] G. Barrand, I. Belyaev, P. Binko, M. Cattaneo, R. Chytracek, G. Corti, M. Frank, G. Gracia, J. Harvey, E.van Herwijnen, P. Maley, P. Mato, S. Probst, and F. Ranjard. Gaudi — a software architecture and framework for building hep data processing applications. *Computer Physics Communications*, 140(1):45 – 55, 2001. CHEP2000.

[33] I. Belyaev, Ph. Charpentier, S. Easo, P. Mato, J. Palacios, W. Pokorski, F. Ranjard, and J. van Tilburg. Simulation application for the lhcb experiment, 2003.

[34] Torbjörn Sjöstrand, Stephen Mrenna, and Peter Skands. Pythia 6.4 physics and manual. *Journal of High Energy Physics*, 2006(05):026, 2006.

[35] D. J. Lange. The EvtGen particle decay simulation package. *Nucl. Instrum. Meth.*, A462:152–155, 2001.

[36] S. Agostinelli et al. GEANT4: A Simulation toolkit. *Nucl. Instrum. Meth.*, A506:250–303, 2003.

[37] The boole project - http://lhcb-comp.web.cern.ch/lhcb-comp/digitization/.

[38] The brunel project - http://lhcb-comp.web.cern.ch/lhcb-comp/reconstruction/.

[39] The davinci project - http://lhcb-release-area.web.cern.ch/lhcb-release-area/doc/davinci/.

[40] R. Frühwirth. Application of kalman filtering to track and vertex fitting. *Nuclear Instruments and Methods in Physics Research Section A: Accelerators, Spectrometers, Detectors and Associated Equipment*, 262(2):444 – 450, 1987.

[41] Lhcb detector performance. *International Journal of Modern Physics A*, 30(07):1530022, 2015.

[42] Zbigniew Was. TAUOLA for simulation of tau decay and production: perspectives for precision low energy and LHC applications. *Nucl. Phys. Proc. Suppl.*, 218:249–255, 2011.

[43] N. Davidson, G. Nanava, T. Przedzinski, E. Richter-Was, and Z. Was. Universal interface of TAUOLA technical and physics documentation. *Comput. Phys. Commun.*, 183:821–843, 2012.

[44] Roel Aaij and Johannes Albrecht. Muon triggers in the High Level Trigger of LHCb. Technical Report LHCb-PUB-2011-017. CERN-LHCb-PUB-2011-017, CERN, Geneva, Sep 2011.

[45] Albert Puig. The LHCb trigger in 2011 and 2012. Technical Report LHCb-PUB-2014-046. CERN-LHCb-PUB-2014-046, CERN, Geneva, Nov 2014.

[46] Daryl Scora and Nathan Isgur. Semileptonic meson decays in the quark model: An update. *Phys. Rev.*, D52:2783–2812, 1995.

[47] D. Cote, S. Brunet, P. Taras, and B. Viaud. Reweighting of the form-factors in exclusive $B \to X l \nu_l$ decays. *Eur. Phys. J.*, C38:105–113, 2004.

[48] Lucio Anderlini, Andrea Contu, Christopher Rob Jones, Sneha Sirirshkumar Malde, Dominik Muller, Stephen Ogilvy, Juan Martin Otalora Goicochea, Alex Pearce, Ivan Polyakov, Wenbin Qian, Barbara Sciascia, Ricardo Vazquez Gomez, and Yanxi Zhang. The PIDCalib package. Technical Report LHCb-PUB-2016-021. CERN-LHCb-PUB-2016-021, CERN, Geneva, Jul 2016.

[49] A A Alves Jr at Al. Performance of the lhcb muon system. *Journal of Instrumentation*, 8(02):P02022, 2013.

[50] V. V. Gligorov and M. Williams. Efficient, reliable and fast high-level triggering using a bonsai boosted decision tree. *JINST*, 8:P02013, 2013.

[51] R Aaij et Al. The lhcb trigger and its performance in 2011. *Journal of Instrumentation*, 8(04):P04022, 2013.

[52] M Williams, Vladimir V Gligorov, C Thomas, H Dijkstra, J Nardulli, and P Spradlin. The HLT2 Topological Lines. Technical Report LHCb-PUB-2011-002. CERN-LHCb-PUB-2011-002, CERN, Geneva, Jan 2011.

[53] I.M. Nugent. Invariant mass spectra of $\tau^- \to h^- h^+ h^- \nu_\tau$ decays. *Nuclear Physics B - Proceedings Supplements*, 253-255(Supplement C):38 – 41, 2014. The Twelfth International Workshop on Tau-Lepton Physics (TAU2012).

[54] The decaytreefitter was originally developed by wouter hulsbergen for the babar experiment and imported to lhcb analysis see https://twiki.cern.ch/twiki/bin/view/lhcb/decaytreefitter.

[55] L. Breiman, J. H. Friedman, R. A. Olshen, and C. J. Stone. *Classification and regression trees*. Wadsworth international group, Belmont, California, USA, 1984.

[56] Yoav Freund and Robert E. Schapire. A decision-theoretic generalization of on-line learning and an application to boosting. *J. Comput. Syst. Sci.*, 55:119, 1997.

[57] Martin Vojik and Peter Lichard. Three-pion decays of the tau lepton, the $a_1(1260)$ properties, and the $a_1\rho\pi$ Lagrangian. 2010.

[58] I. M. Nugent, T. Przedzinski, P. Roig, O. Shekhovtsova, and Z. Was. Resonance chiral Lagrangian currents and experimental data for $\tau^- \to \pi^-\pi^-\pi^+\nu_\tau$. *Phys. Rev.*, D88:093012, 2013.

[59] Kyle S. Cranmer. Kernel estimation in high-energy physics. *Comput. Phys. Commun.*, 136:198–207, 2001.

[60] Tomasz Skwarnicki. *A study of the radiative cascade transitions between the Upsilon-prime and Upsilon resonances*. PhD thesis, Institute of Nuclear Physics, Krakow, 1986. DESY-F31-86-02.

[61] B. Efron. Bootstrap methods: Another look at the jackknife. *Ann. Statist.*, 7(1):1–26, 01 1979.

[62] R. Aaij et al. Study of $B^0 \to D^{*-}\pi^+\pi^-\pi^+$ and $B^0 \to D^{*-}K^+\pi^-\pi^+$ decays. *Phys. Rev.*, D87:092001, 2013.

[63] J. P. Lees et al. Measurement of the $B^0 \to D^{*-}\pi^+\pi^-\pi^+$ branching fraction. *Phys. Rev.*, D94:091101, 2016.

[64] G. Majumder et al. Observation of B0 —> D*-(5 pi)+, B+ —> D*-(4 pi)++ and B+ —> anti-D*0(5 pi)+. *Phys. Rev.*, D70:111103, 2004.